VRIJE UNIVERSITEIT BRUSSEL

Faculteit Wetenschappen en Bio-ingenieurswetenschappen
Vakgroep Fysica - Interuniversity Institute for High Energies

Search for High-Energy Neutrinos Associated with Long Gamma Ray Bursts using the IceCube Detector

Lionel Brayeur

Proefschrift ingediend met het oog op het behalen van de academische graad van Doctor in de Wetenschappen.

Promotor: **Prof. Dr. Nick van Eijndhoven**

November 2015

Doctoral Examination Committee

Chair: Prof. Dr. Jan Danckaert (VUB)
Promotor: Prof. Dr. Nick van Eijndhoven (VUB)
Secretary: Prof. Dr. Freya Blekman (VUB)
Prof. Dr. Stijn Buitink (VUB)
Prof. Dr. Petra Van Mulders (VUB)
Prof. Dr. Michel Defrise (VUB)
Prof. Dr. Nick Van Remortel (University of Antwerp)
Prof. Dr. Ad van den Berg (University of Groningen, The Netherlands)

To Célia

Acknowledgements

The first person I want to thank is my advisor Nick van Eijndhoven. This thesis as well as the extraordinary experiences of the past four years would not have existed without him. More specifically, I thank him for his availability, his many advice and ideas, and all the very careful readings of the manuscript. Dank u voor alles Nick.

The work presented in this thesis would certainly be very different without the help of Geraldina Golup who guided me from the beginning to the very end of the thesis. She helped me to develop the various steps of the analysis and was always available for discussions. I also warmly thank her for the careful proof-reading of the manuscript. Muchas gracias Geri por todo tu apoyo, no lo podría haber hecho sin tu ayuda.

A very special thanks to Célia Paquay who realised most of the sketches shown in the thesis. I am also grateful for the moral support she gave me during all the thesis and especially during the final writing sprint. Merci choubi.

I also want to thank all my colleagues from the IIHE for their support. In particular, I thank Gwen for the proof-reading of the manuscript and my office mate, Martin, as well as Jan and Krijn for all the fruitful discussions we had about Physics and everything else. Merci Martin pour ta bonne humeur qui rendait le bureau de suite plus sympathique. Je suis content d'avoir partagé ces quatre ans avec toi. Bedankt Jan en Krijn voor de samenvatting en voor alle activiteiten buiten werk. I am also happy to have met and spent time with great people from all over the world like Debanjan, Thomas, David and Giulliano. Thank you for your constant good mood inside but also outside the lab.

A big thanks to my office neighbours I did not cite yet, Elisa, Simona and Jan for being indulgent when our office discussion was becoming a little loud. I enjoyed working in the IIHE during these 4 years mainly because of the great atmosphere created by the people who are part of it. For this I thanks Aongus, Christoph, Isabelle, Juanan, Kevin and Sabrina. A special thanks to Catherine and Kael for their support and their advice.

Still in the IIHE, a great thanks to Marleen and Audrey for their efficiency and kindness, it was a real pleasure to have you in the lab. Another great thanks goes to the IT team and especially to Samir for the amazing work he did to get the maximum from our cluster.

I would also like to thank my parents and my sister for having always encouraged me and supported me in my choices. Merci beaucoup à vous trois de m'avoir toujours soutenu dans mes choix et de m'avoir toujours encouragé à atteindre mes objectifs. Je remercie aussi Fabi-

enne et Raymond pour leur soutien.

Finally, I am grateful to the members of the jury, Jan Danckaert, Freya Blekman, Stijn Buitink, Petra Van Mulders, Michel Defrise, Nick Van Remortel and Ad van den Berg who accepted to be part of the Doctoral Examination Committee.

Contents

Introduction

In order to understand the relevance of detecting neutrinos from Gamma Ray Bursts, one must go back a century in the past. In 1907 radioactivity had already been discovered and it was known that there was a natural radioactivity such that ionising radiation was coming from the ground. The study of the amount of ionising radiation was carried out using electroscopes but unfortunately these devices were fragile and thus difficult to transport. The scientist T. Wulf had the idea of creating a new type of electroscope (now called the Wulf electroscope) that was more precise and more mobile [1].

Using his newly designed electroscope, Wulf measured the radiation in many places, from the Caves of Han in Belgium to the 1000 m altitude village of Zermatt in Switzerland. His most important measurements were done at the Eiffel tower, which was the tallest construction in the world at that time[1]. Since the radiation was believed to come only from the ground the expectation was that it should decrease with altitude. However, on the top of the Eiffel tower the decrease of the amount of radiation was much smaller than expected [2]. Wulf had two possible explanations. The first was an unknown source of γ-rays in the atmosphere and the second one was a wrong prediction for the radiation absorption in the air.

After this first hint of radiation coming from above, the Austrian scientist Victor Hess used an electroscope in a hydrogen-filled balloon [3]. Hess measured the radiation up to an altitude of 5 km and he found an increase in the amount of radiation as high as twice the ground level [4]. After Hess, other scientists performed more accurate measurements up to an altitude of 9 km. It became certain that there was radiation coming from space and that this radiation was composed of charged particles. The latter statement comes from measurements at different magnetic latitudes, which have an influence on the radiation intensity (for more details, see [5]). These charged particles were named **cosmic rays**.

In the late thirties, W. Kolhörster and later P. Auger performed measurements of cosmic radiation events in coincidence. This opened the door to the study of cosmic rays at ground level by the detection of the particle shower they induce in the atmosphere, a so-called **air shower** [5]. Initiated by the discovery of air showers, extraordinary large experiments were about to be built in the attempt to detect more energetic cosmic rays.

[1] In many books, cosmic ray introductions start in 1912 with Victor Hess. A detailed article about Wulf's searches and the role of the Eiffel tower in science is available in the Scientific American's website: `http://blogs.scientificamerican.com/guest-blog/paris-city-of-lights-and-cosmic-rays/`.

It was also in the thirties that W. Pauli postulated the existence of a neutral particle later called neutrino. This postulate was needed in order to explain the energy spectrum of the electrons from β-decay [6]. E. Fermi[2] calculated the neutrino cross-section which was so small that it was thought to be undetectable. This calculation was part of a consistent β-decay theory [6]. One had to wait until 1956 and nuclear reactors that would give an enormous flux of neutrinos to be able to detect them [7].

Four years later, in 1960, the Volcano Ranch experiment detected cosmic rays of energies above 10^{18} eV. This was the start of the Ultra High Energy Cosmic Rays (UHECRs) studies [4].

Still in the sixties, experiments at CERN and at Brookhaven National Laboratory discovered a second type of neutrino; after the electron neutrino came the muon neutrino [8]. The prediction of the third type of neutrino, the tau neutrino, happened in 1978 with the discovery of the tau at SLAC [9]. This third type of neutrino was then detected in 2000 by the DONUT collaboration [10].

Neutrinos

So far, there is no evidence for a fourth type (or equivalently flavour) of neutrino. In addition to the study of neutrinos from accelerators and nuclear reactors, several experiments have been designed to study neutrinos from the Sun as well as from the Earth atmosphere. The neutrino production in the Sun comes from the various nuclear reactions occurring in its center as well as from the interaction of particle ejecta falling back to the Sun during solar flares for example.

The atmospheric neutrinos are produced by the interaction of cosmic rays in the Earth atmosphere. In the case of muon neutrinos, the cosmic ray interactions produce pions and kaons which in turn decay producing muon neutrinos. Since the pions and kaons have lost energy before decaying, the energy spectrum of the atmospheric muon neutrinos is steeper than the cosmic ray spectrum [11]. While the neutrinos produced in the Sun have a too low energy to be detected in ICECUBE (as outlined in Chapter 2), atmospheric neutrinos can be detected. The case of atmospheric muon neutrinos is particular since it constitutes the irreducible background of the analysis presented in the current thesis.

The observation of neutrinos from the Sun and the disappearance of electron neutrinos with respect to expectations have led to the conclusion that neutrinos oscillate between their three flavours [11]. This oscillation phenomenon can also be observed in reactor experiments as well as in the detection of atmospheric neutrinos [12].

These oscillations are explained by the theory that the mass eigenstates of the neutrino are a combination of the flavour eigenstates. Of course this implies that neutrinos have a non-zero mass! However, the masses of the neutrinos have not been measured yet and only upper-limits have been set. It is also unknown which of the mass eigenstates is the most massive one. This is known as the hierarchy problem.

[2] It is E.Fermi that first used the word neutrino, which is Italian for small neutron.

What we do know is that neutrinos are neutral and that they interact only through the weak force such that they represent the perfect cosmic messenger, able to carry information from a distant source straight to us.

Cosmic Rays

Currently, the energy spectrum of cosmic rays has been measured up to about 10^{20} eV as shown in Fig. 1. It follows a non-thermal power spectrum of about $E^{-2.7}$ until a first structure is encountered around 3×10^{15} eV called the **knee**, where the spectral index decreases to -3. Then, there is a **second knee** at 8×10^{16} eV, where the spectral index decreases to about -3.2. At around 4×10^{18} eV, there is an increase of the spectral index to -2.6, which is called the **ankle** (for more details, see [5]).

The origins of these structures in the spectrum are still under debate. A possibility for the knee is that the limit of the proton acceleration by galactic supernovae is reached. Hence the knee energy could be the maximum energy up to which the protons are accelerated by the sources within our Galaxy [5]. Similarly, the second knee would be the limit of the galactic acceleration of iron. This hypothesis coupled with the fact that the Larmor radius associated to charged particles of EeV energies is larger than the thickness of the galactic disk imply that at the highest energies, especially above the ankle, the UHECRs are mainly coming from extra-galactic sources.

It is difficult to identify the sources of cosmic rays from their arrival directions since cosmic rays are charged particles and so they are deflected by (inter)galactic magnetic fields on their journey towards the Earth. This deflection cannot be computed precisely since the intervening magnetic field strength and cosmic ray composition are poorly known. Only if the cosmic ray composition is light, i.e. mainly protons, the magnetic deflection may be only a few degrees above a few tens of EeV and thus charged particle astronomy could be feasible.

Thus, in order to understand what are the cosmic rays and where they come from, a key element is the study of their composition. At low energies (below the knee) it was found that they are composed mainly of protons. In small amounts, also nuclei up to $Z \approx 40$ are observed. The abundance of these heavier elements was found to be very close to the composition of the solar system matter [5]. At the highest energies, the lower flux as well as inaccuracies in hadronic interaction models make composition studies very complicated and the composition of the UHECRs is still under debate [13].

Unfortunately the main question remains. Which objects could accelerate the UHECRs to such high energies? As we will see in the first chapter, Gamma Ray Bursts are a possible source but if this is the case, then they should also emit neutrinos (resulting from proton-γ interactions). This is the reason why the century-long search for the source of cosmic rays could be answered by using neutrino detectors like ICECUBE.

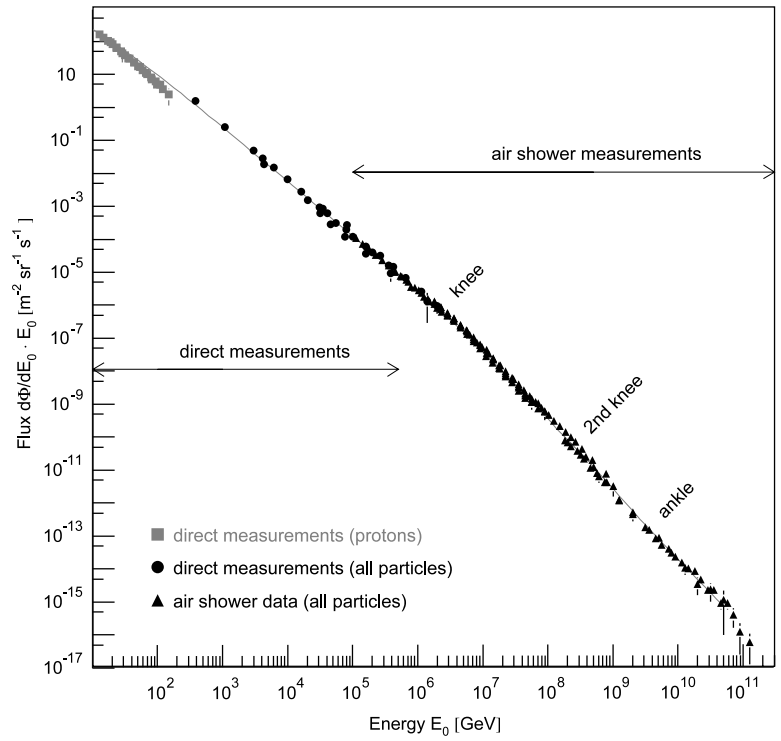

(a)

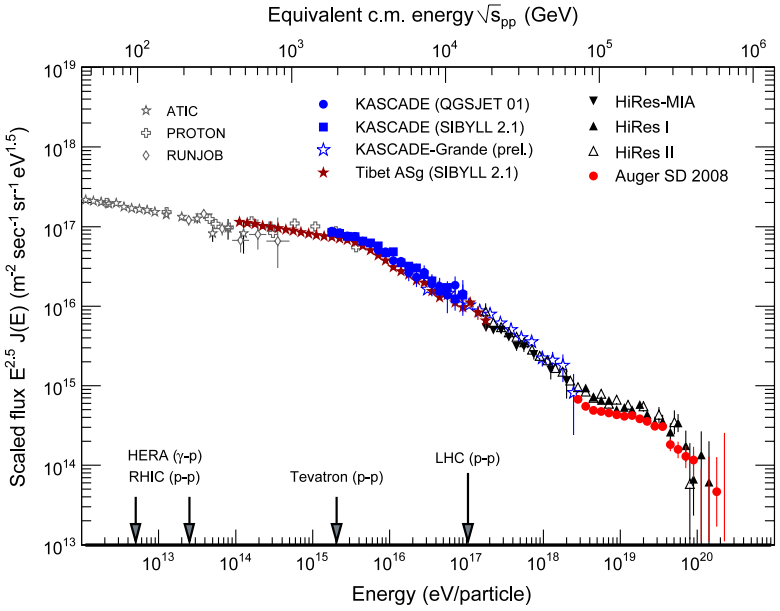

(b)

Figure 1: The cosmic ray energy spectrum. Panel (a) shows the cosmic ray energy spectrum measured by direct and indirect detections. The proton flux is shown at low energies. The structures of the spectrum are indicated but not well visible. In panel (b), one can see the cosmic ray energy spectrum as observed by different experiments. The flux was multiplied by a factor $E^{2.5}$ in order to enhance the visibility of the structures that are the knee, the second knee and the ankle [5]. In the panel (b), there was a mistake in the published figure, HERA was an electron-proton collider.

1

Gamma Ray Bursts

This chapter is dedicated to Gamma Ray Bursts (GRBs). After an historical introduction of their discovery, the observational knowledge will be summarised followed by a brief description of the different theoretical models that have been proposed to explain these particular objects. Finally the predicted neutrino production from GRBs will be described.

1.1 A brief history

This story starts in 1967 when the Vela satellites, a US military satellite system looking for clandestine nuclear tests, made the first observation of a Gamma Ray Burst (GRB) [13]. At first, this short burst was believed to be a possible sign of an extra-terrestrial civilisation. This idea was soon abandoned and in 1973, the discovery was made public.

For almost 20 years the science community thought that due to their incredible fluence emitted over very short time periods (time-integrated energy $\approx 10^{51}$ ergs = 10^{44} J)[14] , GRBs had a galactic origin. But in 1991, the CGRO (Compton Gamma Ray Observatory) satellite [15] was launched with the BATSE (Burst And Transient Satellite Experiment) detector [16] on board as well as three other experiments. The BATSE experiment had a 4π sr field of view, an energy range from 30 keV to 1.9 MeV and an angular resolution of 2 degrees [16, 17, 18].

The BATSE experiment released the first map of GRBs [17] and revealed the isotropic distribution of GRBs to the community. This discovery was a strong hint that GRBs were of extra-galactic origin. However, another possibility was that they were a local phenomenon with respect to the position of the Earth. The extra-galactic origin was confirmed in 1997 with

the first observation of X-ray afterglow (see Section 1.2.2) by the Beppo-SAX satellite [19] that led to the first redshift measurement (the precision of Beppo-SAX allowed optical and longer wavelength follow up observations of the afterglow).

After the success of CGRO, many satellites were used to localise more GRBs with a more accurate precision and a broader energy range. Some examples are the Konus-Wind experiment on board of the Wind satellite launched in 1994 [20], followed by HETE in 1996 [21], INTEGRAL in 2002 [22], Swift in 2004 [23] and Fermi in 2008 [24]. Despite all these new observations, the mystery of the GRB progenitors and of the mechanism of their inner engines remains unresolved up to today. In the next section, the observational knowledge about GRBs will be summarised as well as the explanation of the prompt and the afterglow emissions. Then, the theoretical framework describing GRBs will be outlined and finally the neutrino production inside the bursts will be discussed.

1.2 GRB observations

The first three characteristics that should be mentioned about GRBs is that they are the brightest events in the observable Universe with an energy output of about 10^{51} ergs (10^{44} J)[14] on timescales of seconds to minutes, that they are isotropically distributed and that there is no standard GRB. All GRBs have a different lightcurve, as can be seen from Fig. 1.1[1]. However, GRBs are not completely different from each other; they actually have many similarities in their spectra. The γ-ray emission can last from millisecond to several minutes and is followed by an afterglow emission in the X-ray, optical and radio frequencies, up to several years after the burst [13].

1.2.1 Prompt emission

The prompt emission is the heart of the GRB, the actual time of the γ-ray emission which can last up to 1000 seconds. The γ-ray emission usually comes with an accompanying X-ray emission [14]. In the case of weak γ-rays, the GRB is called an X-ray flash (XRF).

The γ-ray spectrum produced by GRBs is non-thermal. In most cases, it can be empirically fit by two power laws smoothly joined at a break energy (E_{break}). This function, called the Band function [25], can be written as

$$N_E(E) = \begin{cases} A\left(\frac{E}{100\,\mathrm{keV}}\right)^{\alpha} \exp\left(-\frac{E}{E_{break}}\right), & \text{for } E \leq (\alpha-\beta)E_{break}; \\ A\left[\frac{(\alpha-\beta)E_{break}}{100\,\mathrm{keV}}\right]^{(\alpha-\beta)} \left(\frac{E}{100\,\mathrm{keV}}\right)^{\beta} \exp(\beta-\alpha), & \text{for } E \geq (\alpha-\beta)E_{break}, \end{cases} \tag{1.1}$$

where A is a scaling parameter. For $\alpha \approx -1$ and $\beta \approx -2$, the Band function can describe most of the GRB spectra.

[1] Image obtained from `http://heasarc.gsfc.nasa.gov/docs/cgro/images/epo/gallery/grbs/`.

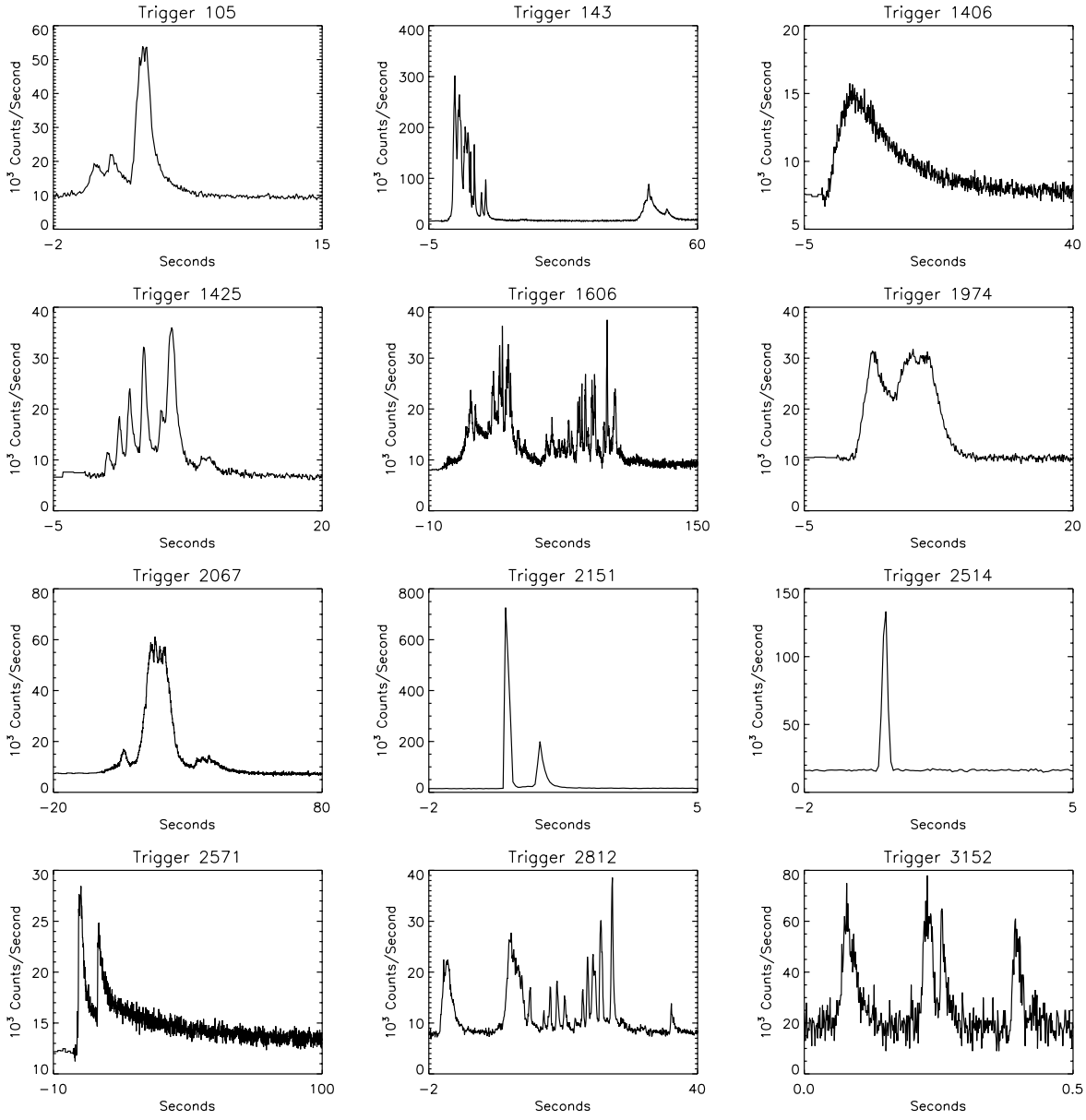

Figure 1.1: Lightcurves of GRBs observed with the satellite CGRO. The uniqueness of all GRB spectra can be observed as well as their variabilities.

A large amount of bursts show a variable time structure during the prompt emission as shown in Fig. 1.1. These structures appear on a significantly shorter time scale than the duration of the burst. Such structures, which can be interpreted as subsequent pulses, have interesting properties. These properties are present in most bursts and they are the similarities mentioned before. First of all, the width of pulses of a given amplitude is constant in time during the γ-ray emission. For example, if one classifies the pulses according to their intensity, the average width of the brighter pulses will not evolve during the GRB and the same is true for the average width of the dimmer ones. However, on average, the dimmer pulses will be wider than the brighter ones [26].

Another interesting feature of these pulses can easily be seen from the BATSE results. The BATSE instruments had different channels corresponding to different energies [16]. The emission observed in the low energy channels was delayed with respect to the high energy channels. This spectral lag between low and high energy pulses was found to be anti-correlated with the luminosity of the GRB (longer lag implies lower luminosity) [27]. This allowed to deduce a GRB luminosity even if the redshift could not be measured [27]. Another method based on the variability of the time structure (defined differently by different authors) gives a variability-luminosity relation that can also be used to infer luminosity without redshift [28].

As will be shown in Section 1.3.2, the pulse structure is an indication for an internal shock mechanism where several shells of dense plasma are colliding into each other. The width of the pulses would then be linked to the size of the colliding shells [26].

To measure the duration of the γ-ray emission the T_{90} value is often used. T_{90} is defined as the time between 5% and 95% of the total measured fluence (time integrated flux) during the GRB [29]. A distribution of T_{90} is shown in Fig. 1.2. One can observe from this figure that the T_{90} distribution is bimodal. There are two maxima corresponding to two superimposed distributions. The bursts that contribute to the first distribution are called short bursts (< 2 s) and the bursts contained in the other distribution are called long bursts (> 2 s) [29].

The duration is not the only difference between long and short GRBs. The short GRBs tend to be more energetic than the long ones [29], as can be seen in Fig. 1.3. The short bursts were first believed to have the same origin as the long ones. However, this idea was rejected because of several differences between the two types of GRBs. More than the overall time and spectral differences, their temporal structures are also distinct. The distributions of pulse width and number of pulses per burst are different between short and long GRBs strengthening the idea of two different populations. However, it was found that short bursts show similar spectral and temporal structures as the two first seconds of the long ones indicating a possible common inner engine [31].

The question of the possible common origin of the short and long GRBs is far from obvious when considering only the prompt emission. The difference between these two populations and their different progenitors becomes stronger once we compare their afterglow emissions.

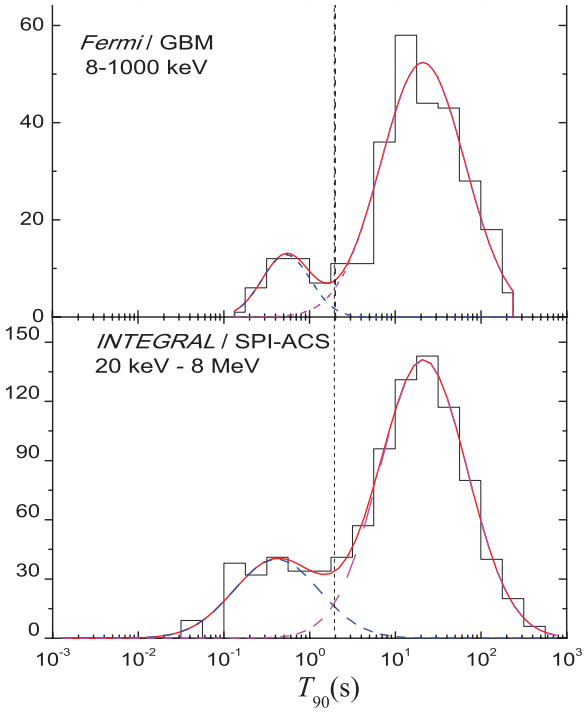

Figure 1.2: T_{90} distribution from Integral and Fermi GBM [30]. The distribution is bimodal indicating two different contributions arising from short and long GRBs.

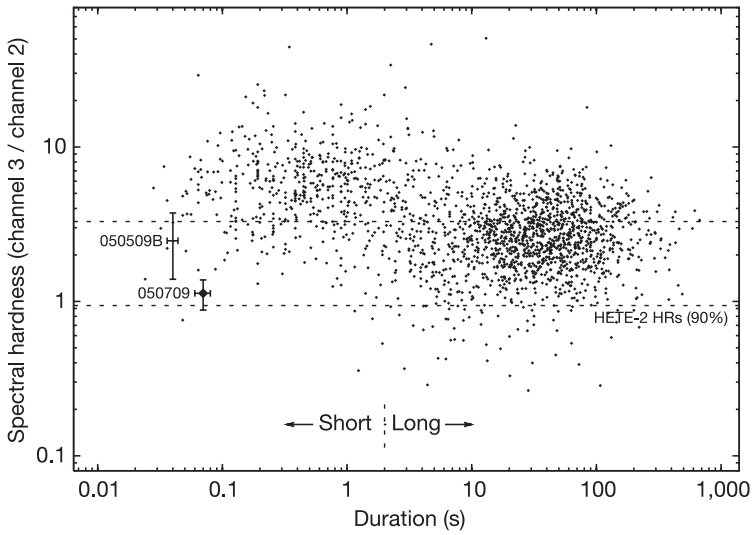

Figure 1.3: T_{90} vs the hardness ratio. The long and short GRB populations are well separated in time and in energy.[32].

1.2.2 Afterglow emission

The afterglow arises at the end of the γ-ray emission. It is first dominated by X-rays, up to several hours after the burst. Then the electromagnetic radiation moves to optical, infra-red (IR) and finally radio wavelength. In some cases, optical flashes were also observed during the prompt phase. In such a case, the optical light is not to be regarded as the low energy tail of the γ-ray emission [14].

The majority of the well localised GRBs has an IR or optical afterglow. If no optical afterglow is detected, the burst is called a dark GRB. These phenomena could be a different class of GRBs but it now seems that they originate from dustier galaxies where the light is absorbed [33].

An interesting property of the afterglow is the absence of correlation with the prompt γ-ray emission. When one tries to extrapolate backwards the X-ray component of the afterglow, the produced spectrum does not fit the γ-ray emission of the prompt phase [14]. This indicates that the prompt emission and the afterglow would come from different mechanisms as we will discuss in Section 1.3.2.

The detection of the GRB afterglow is essential because it allows to measure the redshift of the GRB as well as to identify its host galaxy. Until 2005, it was believed that short GRBs had no afterglow. The discovery of the optical afterglow of GRB050709[2] allowed to define the characteristics of a short GRB afterglow as well as to identify the emission site of the burst [32].

A first difference between long and short GRB afterglows was observed in the X-ray afterglow that was found to be much weaker for short bursts than a typical one from long bursts. Furthermore, unlike many long GRBs, there have been no supernovae type Ic found in vicinity of short GRBs (see [34] for a review of supernova types). When combining these differences between long and short GRBs with those already noticed during the prompt phase, it appears that the two types of bursts are likely to originate from different progenitors.

The detection of radio afterglows has also led to interesting conclusions. The radio lightcurve can be used to infer the size of the GRB up to four weeks after the burst [14]. The size is of the order of 0.01 pc. This measurement provides a proof of the relativistic nature of the ejecta [35] and due to the relativistic nature of the outflow, it is very likely that the ejecta of GRBs are beamed. In this case, only a fraction of all the GRBs would be observable namely those where the jets point toward us. During the afterglow, the outflow loses energy and the ejecta become less and less relativistic. As a consequence, the late afterglow should not be beamed anymore and thus should be observable from anywhere. In this case, one should be able to observe an orphan afterglow i.e. an afterglow without prompt emission.

[2] The name of GRBs depends on the date of their discovery. For instance, GRB050709 was observed the 9^{th} of July 2005. In the case where several GRBs are discovered the same day, a letter (A, B, ...) distinguishes them.

1.3 Acceleration mechanisms

1.3.1 Fermi acceleration

Before describing what happens to the accelerated particles during the prompt emission and the afterglow, it is interesting to describe the mechanism capable of accelerating particles to such high energies. The Fermi mechanism was introduced in the 1940's [36] and is said to be of second order because it depends on $\beta^2 = \left(\frac{V}{c}\right)^2$, where V is the velocity of a gas cloud as shown in Fig. 1.4. This dependence reduces the efficiency of the mechanism, especially for $V << c$. A first order acceleration mechanism ($\propto \beta$) was worked out later (see [37] for a historical review). The first order mechanism is used to describe the acceleration in GRBs.

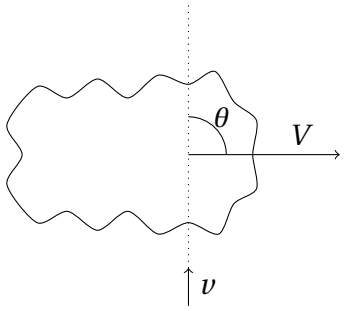

Figure 1.4: Interaction of a charged particle with a cloud of plasma. This situation leads to the second order Fermi acceleration (the original theory). The probability of interaction in this case where $\theta = \frac{\pi}{2}$ is proportional to the velocity of the particle v.

In order to introduce the idea behind the first order Fermi acceleration, we will consider a simplified approach that calculates the energy gain of one particle that crosses a shock several times. A more rigorous treatment can be found in [37]. Such a shock is formed when a dense plasma moves toward a plasma of lower density. The denser plasma located behind the shock belongs to the downstream region and the plasma of lower density that did not encounter the shock yet belongs to the upstream region. More details about the formation of shocks will be given in Section 1.3.2.

Following the calculation performed in [38], we consider in the upstream rest frame, as shown in Fig. 1.5(a), a particle with energy E_1 and momentum $P_1 = \frac{E_1}{c}$. Given the high energy of the particles, their mass can be neglected. After the shock interaction the particle has an energy E_2 and a momentum $P_2 = \frac{E_2}{c}$.

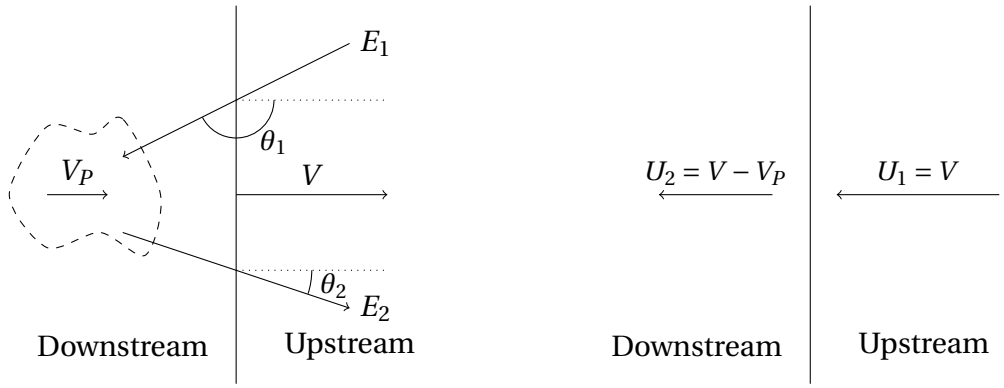

(a) Upstream rest frame (b) Shock rest frame

Figure 1.5: Interaction of a particle with the shock, seen from the upstream rest frame (a) and velocities of the upstream and downstream region in the shock rest frame (b). The particle gains energy by interacting with the plasma on the other side of the shock.

In the downstream rest frame (labelled with a prime):

$$E_1' = \gamma E_1(1-\beta\cos\theta_1) \quad \text{where} \quad \beta = \frac{U_1-U_2}{c} = \frac{V_p}{c} \text{ and } \gamma = \frac{1}{\sqrt{1-\beta^2}}, \tag{1.2}$$

where U_1 (resp. U_2) is the velocity of the upstream (resp. downstream) plasma in the shock rest frame and V_P and V are respectively the velocities of the downstream plasma and the shock in the frame where the upstream plasma is at rest. In this upstream rest frame:

$$E_2 = \gamma E_2'(1+\beta\cos\theta_2'). \tag{1.3}$$

In the downstream rest frame, the particle has the same energy when entering and leaving (due to collisionless scattering), which means that $E_1' = E_2'$. Hence, the gain of energy is

$$\begin{aligned}
\frac{\Delta E}{E} &= \frac{E_2 - E_1}{E_1} && (1.4)\\
&= \frac{\gamma E_2'(1+\beta\cos\theta_2') - \frac{E_1'}{\gamma(1-\beta\cos\theta_1)}}{\frac{E_1'}{\gamma(1-\beta\cos\theta_1)}} && (1.5)\\
&= \gamma^2(1+\beta\cos\theta_2')(1-\beta\cos\theta_1) - 1 && (1.6)\\
&= \frac{(1+\beta\cos\theta_2' - \beta\cos\theta_1 - \beta^2\cos\theta_1\cos\theta_2')}{1-\beta^2} - 1 && (1.7)\\
&= \frac{\beta^2 + \beta\cos\theta_2' - \beta\cos\theta_1 - \beta^2\cos\theta_1\cos\theta_2'}{1-\beta^2}. && (1.8)\\
& && (1.9)
\end{aligned}$$

We must now average over the values of θ_1 and θ_2'. The probability for a particle to interact is proportional to the rate of particles crossing the shock at an angle θ_1. In the case of the second order acceleration, one considers the interaction with a cloud of plasma moving at velocity V. The interaction rate for a particle moving at velocity v is then proportional to $v - V\cos\theta$, where θ is the angle between $\vec{v}$ and $\vec{V}$. This gives a probability per unit solid angle or equivalently per infinitesimal change of $\cos\theta$:

$$\frac{dP}{d\cos\theta} \propto 1 - \beta\cos\theta \text{ for } \theta \in [0,\pi]\,. \tag{1.10}$$

In the case of a shock (first order acceleration), this probability transforms to

$$\frac{dP}{d\cos\theta} \propto \cos\theta + \beta \quad \text{for } \theta \in [0,\frac{\pi}{2}]\,. \tag{1.11}$$

This is due to the fact that for a particle interacting with a plasma on one side of the shock, the plasma on the other side of the shock moves toward it whatever the angle θ is. For example, if $\theta = \frac{\pi}{2}$, the probability of interaction is proportional to the speed of the downstream plasma. This is different in the case of the cloud where $\theta = \frac{\pi}{2}$ corresponds to a particle moving toward a cloud with a velocity perpendicular to the velocity of the cloud (see Fig. 1.4). The probability of interaction in that case is proportional to the velocity of the particle and not to the one of the cloud.

The average of $\cos\theta_1$ can then be written:

$$\begin{aligned}
<\cos\theta_1> &= \frac{\int \cos\theta_1 \frac{dP}{d\cos\theta} d\cos\theta_1}{\int \frac{dP}{d\cos\theta} d\cos\theta_1} && (1.12)\\
&= \frac{\int \cos^2\theta_1 \sin\theta d\theta + \beta\int \cos\theta_1 \sin\theta_1 d\theta_1}{\int \cos\theta_1 \sin\theta_1 d\theta_1 + \beta\int \sin\theta_1 d\theta_1} && (1.13)\\
&= \frac{-\frac{1}{3}(\cos^3(\frac{\pi}{2}) - \cos^3(0)) - \beta\frac{1}{2}(\cos^2(\frac{\pi}{2}) - \cos^2(0))}{-\frac{1}{2}(\cos^2(\frac{\pi}{2}) - \cos^2(0)) - \beta(\cos(\frac{\pi}{2}) - \cos^2(0))} && (1.14)\\
&= \frac{\frac{1}{3} - \frac{\beta}{2}}{\frac{1}{2} - \beta}\,. && (1.15)
\end{aligned}$$

In the case of a non relativistic shock (i.e. $\beta << 1$), $<\cos\theta_1> \approx \frac{2}{3}$. A similar argumentation yields $<\cos\theta_2'> = -\frac{2}{3}$ so that we finally obtain

$$\frac{<\Delta E>}{E} \sim \frac{4}{3}\beta = \frac{4}{3}\frac{U_1 - U_2}{c}\,. \tag{1.16}$$

In the case of second order acceleration, $<\cos\theta_1> = -\frac{\beta}{3}$ and $<\cos\theta_2'> = 0$ because the direction of the particle leaving the cloud is random from the cloud rest frame. Thus we have $\frac{<\Delta E>}{E} \approx \frac{4}{3}\beta^2$ yielding to a much less efficient acceleration.

Another way to calculate the gain of energy for a particle after crossing the shock is to consider the gain in momentum by the fact that the magnitude of momentum is unchanged when crossing the shock in the shock rest frame and then by changing to the downstream rest frame [39]. A third way explained in [37] starts with the plasma diffusion equation and calculates the gain in momentum by crossing the shock without involving any change of reference frame. Following these two alternative procedures, one arrives at the result that the change in momentum when crossing the shock for a particle with momentum p and velocity v, in the case of an upstream plasma moving with a velocity U_1 and a downstream plasma moving with a velocity U_2 (in the shock rest frame, see Fig. 1.5(b)) is

$$\frac{2}{3}\frac{p}{v}(U_1 - U_2)\,. \tag{1.17}$$

The above result is valid for a particle moving from upstream to downstream and from downstream to upstream. This is due to the fact that the plasma on one side of the shock always sees the plasma on the other side of the shock coming toward it. This is why the shock acceleration is so efficient.

Following this framework, assuming that the particle moves relativistically and crosses the shock twice, the gain in momentum or equivalently in energy (using $p \approx E/c$) becomes identical to the previous result in Eq. (1.16). The calculation presented above is a simplification whose purpose is to understand the physics behind the shock acceleration mechanism. In a realistic calculation, one has to take into account that the magnetic field is not always parallel to the plasma velocity nor to the normal of the shock. This difference of direction between the flow velocity and the magnetic field introduces an extra acceleration due to the induced electric field. Such an acceleration is called shock drift acceleration [37].

In the shock rest frame, the plasma on both side of the shock moves toward the downstream region as shown in Fig. 1.5(b). This causes particles to escape the shock region. However, due to the surrounding magnetic field, particles might rotate around the shock such that they cross it several times gaining energy at each crossing. Every time the particle returns to the downstream region it can either escape or return to the shock. At a given energy depending on the magnetic field strength, the gyro-radius associated to the particle becomes to large for the particle to remain in the acceleration site and it escapes [37, 39, 38].

Following closely [38], we will calculate the energy spectrum of the particle accelerated through the shock mechanism. The energy of a particle having an initial energy E_0 before the shock interaction, becomes after crossing m times the shock

$$E = E_0\left(1 + \frac{<\Delta E>}{E}\right)^m\,. \tag{1.18}$$

From this, one can determine m, being the number of times a particle has to cross the shock in order to have an energy E starting from an energy E_0 is

$$m = \frac{\ln\left(\frac{E}{E_0}\right)}{\ln\left(1 + \frac{<\Delta E>}{E}\right)}\,. \tag{1.19}$$

The number of particles with an energy greater than E is proportional to the probability of returning to the shock (which is one minus the probability of escaping the shock), so we obtain

$$N(>E) \propto \left[1 - P(\text{escape})\right]^m . \tag{1.20}$$

This leads to

$$\ln N(>E) = B - (\Gamma - 1)\ln E \tag{1.21}$$

where

$$\Gamma = \left(1 - \frac{\ln\left[1 - P(\text{escape})\right]}{\ln\left(1 + \frac{<\Delta E>}{E}\right)}\right) \tag{1.22}$$

and B is a constant.

Γ can be expressed in terms of the compression ratio for a strong non-relativistic shock $R = \frac{U_1}{U_2}$ [38]. This yields

$$\Gamma \approx \frac{R+2}{R-1}. \tag{1.23}$$

Hence

$$N(>E) \propto E^{-(\Gamma-1)} \quad \text{and} \quad \frac{dN}{dE} \propto E^{-\Gamma}. \tag{1.24}$$

In the case of a strong shock, $R = 4$ [38, 40], which leads to

$$\frac{dN}{dE} \propto E^{-2}. \tag{1.25}$$

This is the main result of the first order Fermi acceleration. In the case of GRBs, the shocks are likely relativistic and though the main idea remains the same, the final result is slightly different. In many cases, numerical simulations are performed in order to take into account as many effect as possible. An example is given in [38] where the final spectral index is not -2 but -2.25. Despite this variation of the spectral index, we will see in Section 1.4 that models predicting neutrino production in GRBs assume that the Fermi acceleration gives an E^{-2} spectrum.

In the case of cosmic rays, as explained in the Introduction, the observed spectrum is $E^{-2.7}$ which is different from E^{-2} or $E^{-2.25}$. This difference is due to the propagation of cosmic rays in the Universe which is energy dependent [38].

1.3.2 Prompt emission and Afterglow

The dominant picture that describes what happens in a GRB is the phenomenological model of the fireball [14]. Because of the short time structures appearing in the lightcurve, it is believed that GRBs originate from a small compact object. The smallness of the progenitor has an influence on the optical depth. Indeed, the optical depth τ_{opt} can be expressed as a number of interactions in terms of the luminosity of the GRB L_γ, the size of the progenitor R_0 and

the energy of the γ-ray E_γ [13]:

$$\tau_{\rm opt} \sim 10^{15} \left(\frac{L_\gamma}{10^{52}\ {\rm erg/s}} \right) \left(\frac{100\ {\rm km}}{R_0} \right) \left(\frac{1\ {\rm MeV}}{E_\gamma} \right). \tag{1.26}$$

With such an expression for τ_{opt}, the medium is optically thick because of pair production processes. Powered by the radiation pressure, the fireball will expand to relativistic velocities until it becomes transparent to radiation. Indeed, if the expansion was not relativistic, given the energy of the photons we observe, the medium will remain optically thick and we would observe a blackbody spectrum in contradiction with observations. However, if the photon outflow comes towards us at relativistic energies, the photons will be blueshifted. That implies that the photons at the source have lower energies. The requirement of an optically thin medium sets a lower limit on the Lorentz boost factor $\Gamma \sim 100$ [14]. The relativistic expansion of the fireball is confirmed by the radio observation of the afterglow as explained in Section 1.2.2.

Following this picture, the non-thermal spectrum is created by the dissipation of the kinematic energy of the relativistic expanding fireball through shocks after the medium becomes optically thin [41]. A way to visualise what happens is to imagine that the progenitor ejects dense shells of plasma followed by the emission of a thinner plasma [13]. The moving shells become multiple shock fronts. Two types of shocks are expected. The internal shocks occur when a shell catches up with another one moving at a lower velocity. This is believed to produce the prompt emission. On the other hand, external shocks that occur when the shells are slowed down by the interstellar medium (ISM) could be responsible for the afterglow.

The high variability of GRBs can be explained in several ways. One of the scenarios assumes that only external shocks occur. In such a case the temporal structure of GRBs arises from the interaction between the ejecta with inhomogeneities of the ISM. However, this requires certain assumptions for these inhomogeneities that are difficult to meet [42]. Another possibility that seems more likely involves internal shocks. During internal shocks, the radiation produced by all the accelerated shells of plasma is disturbed by the collisions of the shells happening when a faster one catches up with a slower one.

In this picture, the width of the pulses that arise in the temporal structure is related to the thickness of the colliding shells [26]. Internal shocks are the direct consequence of the variability of the inner engine. Hence the temporal structure of GRBs reflects the variability of the source [42, 14]. The assumption that the short structures arising in GRB spectra is caused by internal shocks has been confirmed by numerical simulations [26]. In these simulations one needs to restrict the Lorentz boost factor in order to reproduce the observed power law spectrum. This limit gives a maximum $\Gamma \sim 1000$[26]. Hence $\Gamma \in [\sim 100, \sim 1000]$.

Once the shells interact with the ISM and produce the external shocks, a reverse shock appears, going back towards the progenitor[43, 14]. Consequently, one can divide the different regions around the burst into 4 parts, as shown in Fig. 1.6. Region 4 corresponds to the ISM before the forward shock occurs. Region 3 is the shocked matter after the forward shock. Re-

gion 2 corresponds to the shocked matter that has been re-shocked by the reverse shock and region 1 is the region where only the internal shocks occur.

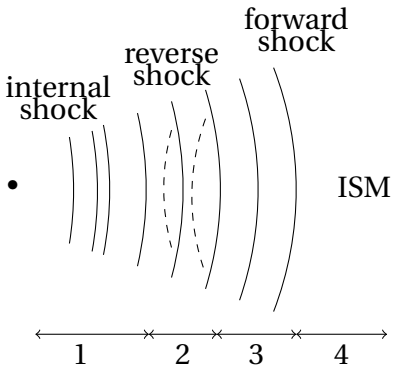

Figure 1.6: View of the 4 regions described in the text.

The γ-rays are expected to come from internal shocks and early forward shocks. They could be produced by synchrotron radiation of accelerated electrons and reach TeV energies by inverse Compton scattering with the high-energy electrons [14]. According to some models, the internal shocks might also contribute to larger wavelength emission like optical flashes [44]. When the reverse shocks happen, the Lorentz boost factor has already been reduced because of the interaction between the accelerated plasma and the ISM. Depending on the model, the reverse shock could contribute to all wavelengths from X-ray to radio [14, 45, 44]. According to the observation in several wavelengths from GRB130427A [43], the reverse shock emission dominates first in UV, optical and IR and later in radio and the forward shock emission dominates first in X-ray and later in UV, optical and IR.

The fireball model allows to reproduce most of the observational data from GRBs [14]. However, many aspects remain unclear. The biggest uncertainties in the model come from the value of the Lorentz boost factor Γ and from the baryonic loading being the amount of energy given to protons over the amount of energy given to electrons and γ-rays.

1.3.3 Possible progenitors

As explained in Section 1.2.2, long and short GRBs are expected to come from different progenitors. Long GRBs are often observed in galaxies with a high star formation rate (SFR) [14]. They are often found in the vicinity of a supernova type Ib or Ic indicating that long GRBs could come from the collapse of very massive stars into black holes [41]. In this so called collapsar model [14], the core of a star of $\sim 30 M_\odot$ collapses resulting in a hypernova in which a black hole arises from the collapse and an accretion disc appears. The fireball would be produced by the transformation of gravitational energy into kinetic energy [13, 14].

The short bursts are localised in galaxies with many types of SFR. Unlike long bursts there is no evidence of supernovae related to them. The general belief is that short GRBs occur from the merger of two compact objects such as two neutron stars or of a neutron star and a black hole.

1.4 Neutrino production

Neutrinos with various energies are expected to be produced in GRBs. In supernovae, nearly all of the energy is carried away by thermal neutrinos of energies around 10 MeV. In the case of GRBs, these thermal neutrinos can be expected around energies of ~ 100 MeV [13]. In the case of a significant proton density, neutrinos of GeV to tens of GeV energy could be produced by proton-proton or proton-neutron interactions [46, 40]. When the proton energy increases over 10^6 GeV, the dominant process for neutrino production becomes the proton-photon interactions [47]. Higher energy neutrinos are expected from such interactions between accelerated protons and high-energy photons.

Of course this possibility requires that protons are present in the fireball (hadronic model). This is likely to happen if GRBs are coming from the collapse of a massive star or from the merger of neutron stars. As such, in this thesis, we intend to search for related high-energy neutrino production and use this neutrino signal as a unique proof for associated hadronic processes.

1.4.1 high-energy neutrinos

The general idea for the production of high-energy neutrinos (>1 TeV) is the interaction between shock accelerated protons (> 10^{16} eV) and γ-rays. As explained in Section 1.3.2, γ-rays would reach their energy by inverse Compton scattering on the shock accelerated electrons. The neutrino production would be efficient because of the formation of the Δ resonance. A Δ^+ baryon is formed of two up and one down quarks and its mass is about 1232 MeV/c^2. The total process is

$$p\gamma \rightarrow \Delta^+ \rightarrow \begin{cases} n\pi^+ \\ p\pi^0 \end{cases} \tag{1.27}$$

$$\pi^+ \rightarrow \mu^+ + \nu_\mu \rightarrow e^+ + \nu_e + \bar{\nu_\mu} + \nu_\mu \tag{1.28}$$

$$\pi^0 \rightarrow \gamma\gamma \tag{1.29}$$

where p is a proton and n a neutron. This mechanism is sketched in the left part of Fig. 1.7. The neutrinos produced by this mechanism would have an energy up to ~ 100 TeV [13, 48]. The photons arising from the decay of the neutral pions would reach energies up to PeV and they would contribute to the observed γ-rays of the prompt emission (≈ MeV-GeV).

So far, no PeV photon has been detected because at these energies photons efficiently interact with other photons creating e^+ e^- pairs. Interactions with electrons from the jet will

also contribute to degrade their energy. Moreover, the PeV photons that will manage to escape the bursts will interact with the photons of the extra-galactic background light (EBL) before they can reach the Earth (the photon mean free path distance at 1 PeV is $\approx$ 10 kpc) [49]. This is a strong argument in favor of the neutrinos as a unique tool to investigate these processes. They are not deviated by magnetic fields unlike protons and they do not suffer from a cut off in their spectrum in PeV energies unlike photons. Neutrinos are also the only messengers that can directly convey information about the inner engine of GRBs because they can be created very close to the engine and travel to us without being affected in any way during their journey.

Though there is a general agreement on the global mechanism described above, many different methods to calculate the neutrino flux from GRBs have been proposed. The models can be divided in two categories depending on their assumptions about the Ultra High Energy Cosmic Rays (UHECRs): (i) the UHECRs are mainly produced in GRBs and (ii) only a part of the UHECRs is produced in GRBs.

The idea that GRBs would produce the UHECRs comes from two observations. First, the GRBs (as well as the Active Galactic Nuclei) are amongst the most energetic events in the Universe, so it is in these objects that one could expect the highest energy cosmic rays [38]. Second, the protons accelerated through the Fermi mechanism follow a power law spectrum which is also the shape (though it is a different index due to propagation effects) of the UHECR spectrum.

In the first category, the neutrino spectrum can be normalised with the UHECR spectrum. Before the stringent neutrino limit set by ICECUBE [50], models generally assumed that the amount of energy given to protons in the fireball was of the same order as the amount of energy given to electrons [48] (i.e. the baryonic loading $f_e^{-1} \in [1, 10]$). A large set of parameters is critical for the neutrino production. The three main ones are the baryonic loading, the Lorentz boost factor and the amount of baryonic energy given to pions (assumed $\approx$ 20%) [51].

Another type of model where protons are magnetically confined in the fireball has also been proposed [52, 53]. In this model, neutrons coming from the primary proton interactions and which are produced together with the pions, escape the fireball and decay into the protons producing the UHECRs. This model is represented in the right part of Fig. 1.7. The main interest of this model is that it links directly the neutrino flux with the UHECR flux because neutrinos and cosmic rays come from the same proton-photon interaction. This allows to calculate the neutrino flux without using any assumption about the fraction of protons that initiate neutrino production.

In the second category, one uses the γ-ray spectrum to normalise the neutrino one. This has the advantage of allowing a calculation of the neutrino flux per GRB and not for the entire GRB population [54]. However, this model requires an extra assumption. As in the first category, the baryonic loading is assumed between 1 and 10 but one has also to assume that the amount of energy given to protons is of the same order as the amount of energy given to photons. For models from the first category, this assumption can be justified because the total

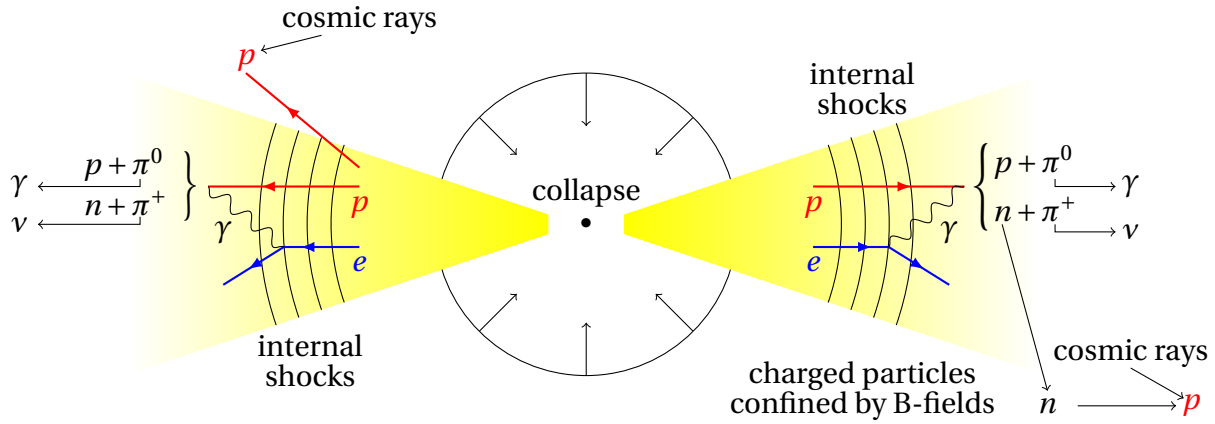

Figure 1.7: Schematic representation of the fireball model. The general idea of the fireball model where proton-photon interactions give high-energy photons and neutrinos is shown on the left. The protons that did not interact escape and become the UHECR. A variant of the fireball model where charged particles are trapped in the magnetic field (neutron escape model) is sketched on the right. In this alternative model, only the neutrons can escape forming the UHECR by decaying to protons.

energy carried by the extra-galactic cosmic rays is comparable to the total GRB γ-ray fluence.

1.4.2 Model constraints

Due to the recent results from ICECUBE [50], the fireball models have been updated with more precise calculations (often numerical) taking into account other processes than the Δ resonance [55]. The value of several parameters like the Lorentz boost factor, the baryonic loading or the amount of baryonic energy given to the pion have been modified to accommodate the observed data. The information of cosmic-ray data, γ-ray observations and neutrino limits has been combined in order to restrict the value of several parameters of the fireball model [51]. This study ruled out the neutron escape model (mainly due to the ICECUBE limit) and states the necessity of a baryonic loading above the standard value of 10 if one wants to keep the GRBs as main sources of UHECRs.

It is important to remark that the ICECUBE limits concern only neutrinos that would be emitted during the prompt phase. However neutrinos can be expected at three different time scales[47]. They are mainly expected to come at the time of the prompt emission but one can also expect neutrinos from the afterglow and even before the burst. During the afterglow, interactions between protons and UV photons from the reverse shock could produce high-energy neutrinos ($\approx$ EeV) [41]. If neutrinos are produced when the fireball is still opaque to photons, they would be detected before the γ-rays. Such neutrinos are named precursor

neutrinos. Since no limit was set by ICECUBE on precursor or afterglow neutrinos, there are only few constraints on the neutrino emission from these phases.

For completeness, it is useful to mention that hadronic models are not the only possibility. Leptonic models also exist where the fireball is mainly composed of electrons. In this case, no neutrinos are expected (an example is [56]).

The observation of high-energy neutrinos from GRBs would confirm that hadronic interactions take place in these extraordinary explosions. The spectrum and the flux of these neutrinos would confirm or reject the hypothesis that the GRBs are (one of the) sources of UHECRs. Finally, such a neutrino observation would help us understanding what is the inner engine of GRBs and how the observed γ-rays are produced.

The detection of high-energy neutrinos is only possible in a detector sufficiently large in volume such that the interaction rate becomes sufficiently large to allow for a discovery. Such a detector has been built in Antarctica by the ICECUBE collaboration. The following chapter will explain in detail the ICECUBE Observatory from its construction to its operation.

2

The ICECUBE Neutrino Observatory

In this chapter, we will focus on the ICECUBE detector. After a short overview of the detector, the principle of neutrino detection will be explained as well as the possible signatures generated by the different neutrino interactions. This part will be followed by the description of the hardware used in ICECUBE from the design of the optical module to the data sent to the Northern Hemisphere from the ICECUBE Laboratory at the surface. Then, the first background rejection methods from the triggers and the filters will be presented and finally, the properties of the South Pole ice, which are essential for the event reconstruction, will be discussed.

2.1 Overview

The first attempt to build a large scale Cherenkov detector was performed in water with the Deep Underwater Muon and Neutrino Detector (DUMAND) located close to Hawaii [57]. This attempt was not successful but other (smaller) experiments did achieve interesting results. One of these experiments was the Antarctic Muon and Neutrino Detector Array (AMANDA) which started in 1993. Once completed, AMANDA consisted of 667 optical modules (light detectors) deployed in the South Pole ice [58]. The construction ended in 2000 and the detector was in operation until 2009.

ICECUBE is the successor of AMANDA. It is a kilometer cube detector buried in the Antarc-

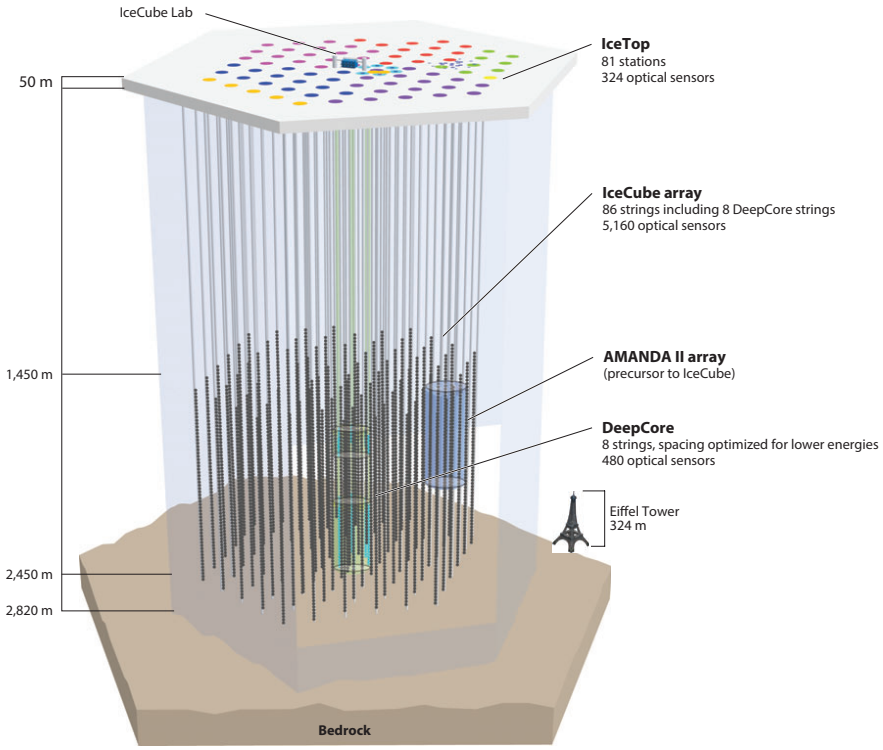

Figure 2.1: The ICECUBE detector at the Amundsen-Scott South Pole Station. The DeepCore sub-array used to lower the energy threshold of ICECUBE is in green [60]. The precursor of ICECUBE, AMANDA is in blue.

tic ice [59, 60, 61, 62]. It is located near the geographic South Pole and it is composed of 5160 optical sensors. These sensors called **DOMs** for Digital Optical Modules cover a horizontal hexagonal surface of a square kilometer between 1450 m and 2450 m under the ice. This implies that the lower DOM is located only 370 m above the rocks that form the Antarctic continent (see Fig. 2.1). The modules are distributed over 78 ICECUBE strings plus 8 DeepCore strings (see below). The 78 ICECUBE strings are horizontally spaced by 125 m and the DOMs are spaced by 17 m on each vertical string.

This 78-string configuration allows the detection of neutrinos with a lower energy threshold of about 200 GeV. In the center of the detector, a region is more densely instrumented. This sub-array is called DeepCore and is composed of 8 strings horizontally separated by 72 m. The DOMs along a string in DeepCore are spaced between 10 m (the 10 first DOMs) and 7 m (the 50 others). Thanks to DeepCore, the energy threshold can be lowered to about 10 GeV.

On the top of ICECUBE, at the surface level, an air shower array detector has been built [59]. It is composed of 162 tanks filled with frozen water and DOMs submerged in this ice. The tanks are deployed on 81 stations of two tanks each located close to the ICECUBE strings. This detector is called **IceTop** and is mainly used for cosmic ray studies. However, it can also be used as a veto for ICECUBE events in order to reject atmospheric neutrinos and atmospheric

muons.

The construction of ICECUBE took seven years, from 2004 to 2011. Due to the extreme climate at the South Pole, only the Antarctic summer can be used for deployment. The detector has been taking data and analyses have been performed during the construction phase. One refers to such uncomplete detector with the number of strings that were deployed. For example, an analysis with IC59 refers to an analysis performed with data taken by ICECUBE when it was composed of 59 strings in total. The completed observatory is referred to as IC86, which is the configuration used for the analysis described in this thesis.

2.2 Detection principle

In order to observe a neutrino with ICECUBE, it must weakly interact with a nucleus of the ice or of the rocks under ICECUBE and produce at least one relativistic charged particle. This interaction can be charged current (CC) via exchange of a W boson or neutral current (NC) via exchange of a Z boson. The produced relativistic charged particle travels through the detector emitting Cherenkov light that can be detected by the optical sensors. The two main interaction possibilities are

$$\nu_l + N \rightarrow l + X \qquad \text{Charged Current} \tag{2.1}$$

$$\nu_l + N \rightarrow \nu_l + X \qquad \text{Neutral Current} \tag{2.2}$$

where l is a lepton (electron, muon or tau), N is a nucleus and X is the hadronic state after the interaction.

In charged current interactions, for a neutrino energy around 10 GeV, 50% of this energy is transferred to the lepton [57]. For a neutrino of higher energy this percentage can go up to 80%. What remains of the energy is transferred to the nucleus producing a hadronic shower (showers will be explained in Section 2.2.4). In the case of neutral current interactions, the neutrino exchanges energy with the nucleus producing only a hadronic shower.

2.2.1 Interaction probability

Following [57], one can derive an approximate neutrino interaction probability in the detector. If $L(\theta)$ is the length traveled by a neutrino arriving at a zenith angle θ in the detector, this probability can be written

$$P(E_\nu) = 1 - \exp\left[-\frac{L(\theta)}{\lambda_\nu(E_\nu)}\right] \approx \frac{L(\theta)}{\lambda_\nu(E_\nu)}, \tag{2.3}$$

where the mean free path for a neutrino traveling in ice $\lambda_\nu(E_\nu)$ can be expressed

$$\lambda_\nu(E_\nu) = \left[\rho_{\text{ice}} N_A \sigma_{\nu N}(E_\nu)\right]^{-1}. \tag{2.4}$$

In the above equation, the density of the ice $\rho_{\text{ice}} = 0.9$ g cm^{-3} , N_A is the Avogadro's number and $\sigma_{\nu N}(E_\nu)$ is the neutrino-nucleon cross section. Details of the neutrino-nucleon cross section can be found in [63].

This calculation is a first approximation because it does not take into account that the Earth becomes opaque to neutrinos at high energies. The value of L, the distance the neutrino travels in the detector, is also an approximation because the neutrino can interact outside the detector and the reaction products could still generate detectable light [57].

The interaction between a neutrino and an electron in the ice has such a low probability that it is negligible. However, there is an exception for interaction at 6.3 PeV where a resonant cross section cannot be neglected anymore [63].

It is important to notice that for a neutrino energy $E_\nu > 10$ GeV, the median angle between the neutrino and the lepton produced by a charged current interaction is given by the formula [64]

$$\Delta\theta[\text{rad}] \approx \left(\frac{1}{\pi \frac{E_\nu}{1\text{ GeV}}} \right)^{\frac{1}{2}} \tag{2.5}$$

In the case of the energies considered in ICECUBE, the neutrino and the lepton can be considered as collinear. This is important because it allows us to trace back the direction of the neutrino by reconstructing the direction of the lepton as we will see in the next chapter.

2.2.2 Energy loss of charged leptons

The lepton produced by a CC interaction will travel through the ice losing energy to the surrounding medium. The average energy loss per distance traveled by a lepton can be written as [65]

$$-\langle \frac{dE}{dX} \rangle = \alpha + \beta E \tag{2.6}$$

where X is in units of g cm^{-2} , E is the energy of the lepton, α is the ionisation energy loss given by the Bethe-Bloch formula and $\beta = \beta_{\text{brem}} + \beta_{\text{pair}} + \beta_{\text{nucl}}$ is the sum of the radiative processes which are the Bremsstrahlung, the e^+ e^- pair production and the photonuclear scattering [65]. The ionisation energy loss is nearly constant while the radiative energy loss is weakly dependent on energy.

In the case of a muon, the losses by radiative processes become dominant over the ionisation losses above ≈ 1 TeV [65]. Thanks to this energy loss mechanism, the muon energy can be estimated from the total number of photons detected along the muon track.

The Bremsstrahlung process is the photon emission from a charged particle when it interacts with the electric fields of the nuclei in a medium (the ice in our case). The pair production comes from the emission of a photon that converts into an e^+ e^- pair. The electrons and positrons produced will also lose their energy by ionisation and radiative processes creating more photons and more pairs. This gives an electromagnetic shower. Pair production

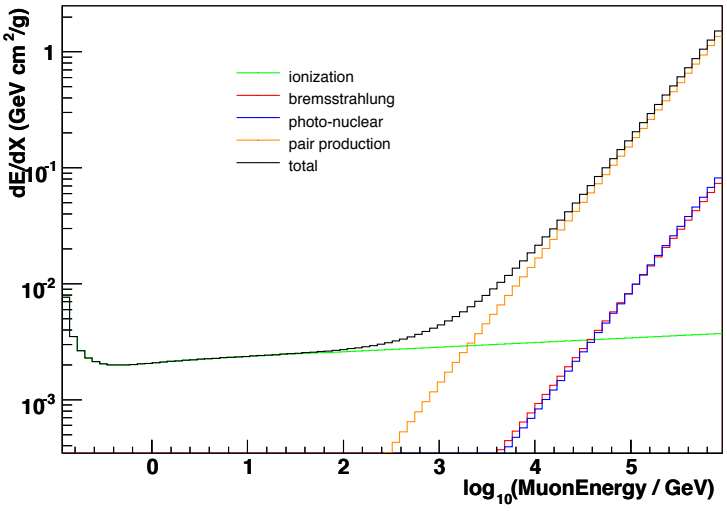

Figure 2.2: Energy loss for a muon traveling in a medium similar to the Antarctic ice [66]. Pair production is the dominant mechanism above ≈ 1 TeV.

is actually the main mechanism for a muon to lose its energy above ≈ 1 TeV as can be seen in Fig. 2.2 [65].

The photonuclear scattering is an inelastic scattering between a lepton and a nucleon (or a nucleus). It consists of the exchange of a virtual photon. If the four-momentum transferred from the lepton to the hadron is large enough, the process is called deep inelastic scattering [67]. The virtual photon is then absorbed by the nucleon generating a final hadronic state.

2.2.3 Cherenkov radiation

The Cherenkov radiation arises from the ionisation energy loss term of Eq. (2.6). Indeed, in the Bethe-Bloch formula, there is a term called the density effect. Neglecting this term corresponds to the situation where a charged particle crossing a medium interacts with electrons in the medium (ionisation) one at a time and independently.

For a relativistically moving particle, this simple vision does not work. One has to consider that the relativistic charged particle will disturb the fields generated by atoms in the medium and this will influence the fields at the location of the ionisation process [68]. This will result in a slight change in the ionisation (a lower energy deposition), hence the presence of the density effect in the Bethe-Bloch formula. This density effect can be seen as a modification of the fields because of the polarisation of the medium.

If one calculates the energy deposited in the medium by a charged particle moving at relativistic velocity, it is seen that all the energy is distributed close to the particle path except in the case when the particle velocity is larger than the phase velocity of the electromagnetic field in the medium. In this case, radiation is emitted called Cherenkov radiation because it was first observed by Cherenkov in 1934. Like for the density effect, this is due to the polari-

sation of the medium. The density effect and the Cherenkov radiation are actually originating from the same phenomenon considered differently (they correspond to two different limiting cases) [68].

In a qualitative observation, the Cherenkov radiation could be seen as a light equivalent of the sonic shock. This is only qualitative because the sonic shock is formed from sound waves emitted even when the velocity is lower than the sound speed that sum up in a wave front when the velocity reaches the sound speed. The Cherenkov radiation appears only when the particle moves faster than the (phase) speed of light in a medium and consists of radiation from the polarised medium and not from the ultra-relativistic particle.

A very interesting feature of the Cherenkov radiation is its emission at a fixed angle, θ_c, depending only of the velocity v of the particle and the refraction index of the medium n [68, 40]

$$\cos\theta_c = \frac{1}{n\beta} \qquad \text{where} \qquad \beta = \frac{v}{c}. \tag{2.7}$$

In the case of ICECUBE, we can consider that $\beta \approx 1$ and by using in the refraction index for ice we get $\theta_c \approx 41°$. A charged particle crossing the ice (or any medium) will radiate as long as $\beta > \frac{c}{n}$ [40]. The Cherenkov emission covers all wavelengths λ but its intensity increases with shorter wavelengths as can be seen from the Frank-Tamm formula [40]

$$\frac{d^2N}{dxd\lambda} = \frac{2\pi\alpha z^2}{\lambda^2}\left(1 - \frac{1}{\beta^2 n^2}\right), \tag{2.8}$$

where z is the particle charge and α is the fine-structure constant. This implies that the maximum emission occurs at blue and low energy UV light.

2.2.4 Different signatures

Since bremsstrahlung and pair production are mass dependent, these processes are much more efficient for electrons than for muons or taus. As a result, an electron will quickly lose its energy producing an electromagnetic shower. A muon of the same energy will travel a longer distance releasing less energy per unit distance. The tau has a very short lifetime and therefore, there is a high probability that it decays in the detector.

These differences lead to different signatures for the three neutrino flavors. For all flavors, in the case of a neutral current interaction, a hadron shower is initiated by the fragmentation of the struck nucleon producing various types of particles. The hadronic shower has also an electromagnetic component due to e.g. neutral pions that decay into photons which subsequently convert into e^+ e^- pairs. Such a shower generates a ball of light coming from the Cherenkov radiation of all the particles involved in the shower that extends in all directions. Such a signature in the detector is called a **cascade**.

In the case of a charge current interaction, the signature will depend on the flavor. The electron created by the interaction will release its energy in a distance smaller than the distance between two optical modules such that the detector signature will be an electromagnetic cascade which will look very similar to a cascade initiated by hadrons.

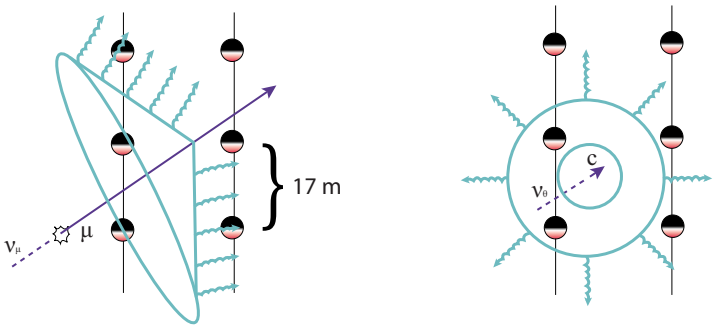

Figure 2.3: Difference of the light emitted by a cascade (on the right) and a track (on the left) in the ice [57].

The muon case is the most interesting one for point source studies as we will see in Section 3.2. A muon of TeV energy can travel up to several kilometers across the detector (i.e. in ice) emitting Cherenkov light along its trajectory [57]. Such a signature is called a **track**. The difference between tracks and cascades can be visualised in Fig. 2.3

The tau signature is different whether it decays into hadrons or a muon. In the case of a hadronic decay, one should observe a first cascade when the neutrino interacts followed by a track generated by the tau and finally another cascade produced by the hadronic decay products of the tau (this is called a double bang). In the case of the muonic decay of the tau, the signature is a cascade followed by a thin track generated by the tau followed by a thicker track after the muon is produced [69].

2.3 The ICECUBE Data Acquisition System

The data acquisition system of ICECUBE is explained in detail in [61]. It is composed of several elements:

- The DOMs, which detect photons and digitise the signal;
- the DOMHub, which is located at the surface and receives the data from the DOMs;
- the Cable Network, which connects the DOMs together and to the DOMHub;
- the Master Clock, which calibrates the DOMHub using a GPS signal;
- the Stringhub, which amongst other tasks, time-orders the signals coming from DOMs along a string.

The purpose of these components is to transport the information about a set of properties that characterises the detected signal to the ICECUBE laboratory (ICL) where the data can be triggered and filtered before the remaining events are sent to the Northern Hemisphere

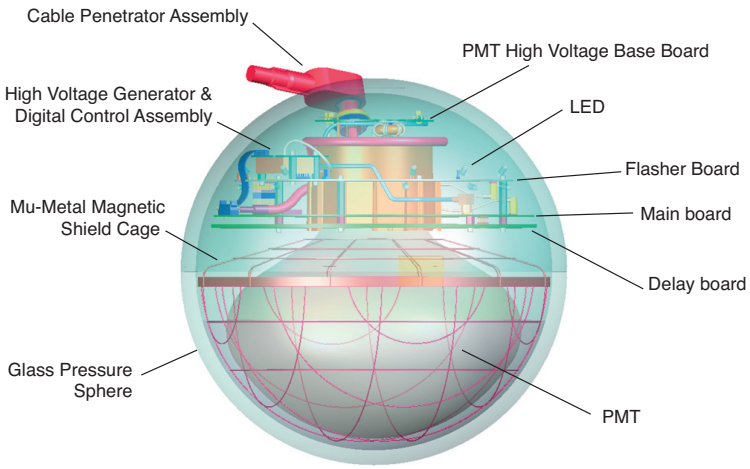

Figure 2.4: Drawing of a Digital Optical Module. The lower part detects photons and the upper part digitises the signal [61].

(details about triggers and filters can be found in Section 2.4). This set of properties is called a **Hit**. The amount of information that composes the Hit depends on the coincidence of the detection between several DOMs. This will be explained in more detail in the first part of this section dedicated to these optical modules which are frozen in the ice. The second part will focus on the different tasks performed in the ICL.

2.3.1 Digital Optical Modules

The cable network to which the DOMs are attached is a copper wire-pair that allows communications between the DOMs and the ICL but also between pairs of DOMs. It has a thickness of 3 cm and it supports data rates up to 900 kb/s for the DOMs located in the deepest part of the detector. This network also supplies power to the modules. A string which consists of the cable network with 60 DOMs attached to it is deployed in a water filled hole. Indeed, the ice is first melted along more than 2000 m before the string can be immersed. Once this operation is over, the ice re-freezes and the DOMs are trapped in the ice such that they are not accessible anymore for repair. The design of the modules had to take this constraint into account in order to conceive a stable electronic system with a long lifetime.

Technical design

The DOMs are composed of two main elements (see Fig. 2.4). First, a photomultiplier tube (PMT) that transforms the incident photons into an electrical signal and second, a computer that digitises the signal. The digitisation is necessary because of the very long cables linking the DOMs to the ICL due to which an analog signal would be disturbed leading to a loss of information.

The PMT has a diameter of 25 cm (Hamamatsu brand) and is supplied by a modular 2 kV power. The computer is composed of three elements. First, a mother board (MB) that receives the data from the PMT and digitises it. This board can be remotely accessed from the surface if one needs to change some parameters like the duration of data taking that will form the Hit or to reboot the DOM.

The digitisation is performed using two digitisers. The first one is the Analog Transient Waveform Digitizer (ATWD) which digitises at a higher rate but for a total time of 0.43 μs. In order to save power, the ATWD stores the signal and takes its time to digitise. While the digitising process is ongoing, the ATWD cannot record any other signal creating a dead-time. To overcome this problem, a second ATWD has been placed in the DOM such that when a signal arrives, it goes to the free ATWD. Furthermore, in order to account for the possible difference in signal strength, the ATWDs have three channels with each channel having a different gain ($\times 16$, $\times 2$, $\times 0.25$). The second digitiser is the Fast Analog to Digital Converter (fADC), which digitises at a lower rate but can manage longer waveforms up to 6.4 μs.

The second element of the electronic part is a flasher board composed of LEDs that can mimic the light induced by Cherenkov emission in order to simulate an event, calibrate adjacent DOMs or to study the properties of the ice. A LED is also available on the mother board in order to calibrate the DOM by the detection of the scattered light emitted by the LED. The third element is the PMT high voltage subsystem that is located on top of the flasher board and that is supplied in power by the mother board.

The DOM components are surrounded by a thick glass sphere (13 mm) that must resist to the high pressure that is exerted on it when the water freezes in the hole. The complete DOM is a sphere with a diameter of 33.2 cm filled with dry nitrogen at a pressure of 0.5 atmosphere to maintain a strong force against the glass.

Local Coincidence

By coupling the DOMs via dedicated transceivers, a capability for Local Coincidence (LC) search has been implemented. A LC happens when a DOM detects a signal and receives a "tag" from another DOM that also detected a signal within 1 μs. The tag sent by a DOM to another one when a signal is detected can be modified and retransmitted such that one can build a coincident chain along a string of a certain length depending of the number of DOMs that detected a signal.

In case a DOM detects a signal but receives no LC tags from the direct neighbour DOMs (one above or one below) nor from the second neighbours (two above or two below), it will run in a compressed mode. This means that it will not transmit the entire detected waveform but only basic information (three samples of the fADC around the recorded peak amplitude) yielding to a "light" Hit called Soft Local Coincidence[1] (SLC).

When a signal is detected and a tag from a direct neighbour or a next to direct neighbour DOM is received, the DOM will run in Hard Local Coincidence (HLC) mode. The entire

[1]This term is misleading because a SLC Hit is a Hit where no local coincidence was detected.

digitised waveform (ATWD and FADC) is compressed to reduce the data rate without any information loss and is then transmitted to the ICL.

Such a LC system allows to reduce the data rate on the string and forms an efficient noise rejection without losing much information about physical process. Indeed, an isolated Hit is probably caused by noise from the PMT or by a particle that has too low energy to be detected by ICECUBE.

2.3.2 The ICECUBE Laboratory

The ICL is located at the surface close to the middle of the detector. All the cables from the different strings are collected in this laboratory. It is also from this location that the data are transferred to the North after filtering (see Section 2.4 for details).

It is at the ICL that one can find the computers that receive the data from the strings. More specifically, the DOMHub is a computer consisting of several components that allows the communication with the strings. A substructure handles the power and the communications for all DOMs on a string. This substructure receives the Hits and can control the DOMs in order to perform several tasks like calibration. An other substructure receives the GPS signal and distributes it to the DOMHub subsystems.

The DOMHub also hosts the Stringhub, a software that converts Hit information from the DOMs to a format suitable for a physics purpose like triggering and event building. More detail about triggering will be given in the next section.

2.4 Triggers and Filters

The rate at which the DOMs produce Hits, mainly from dark noise, is about 500 Hz per DOM. In the case of HLC Hits, the rate drops down to 5-15 Hz per DOM [70]. With more than 5000 DOMs, this represents a tremendous amount of data. To reduce this amount of data, specific triggers have been implemented.

Once the Hits are received at the ICL, the system searches for several criteria in order to save the recorded data [70]. In case none of the predefined criteria are met (no triggers were flagged), the data are discarded. When the criteria corresponding to a trigger are satisfied, the waveforms coming from HLC Hits and the basic information from SLC Hits are "packed" in an event. The duration of an event depends on the trigger that was tagged as explained hereafter. Once the event is built, it goes through the filter procedure. The filters are designed to search for a particular signature in the events. Details about the filters will be given in the second part of this section.

2.4.1 Triggers

ICECUBE uses several triggers. The most common one is the Simple Multiplicity Trigger (SMT) that selects data if a certain number of HLC Hits are detected in a given time window. For

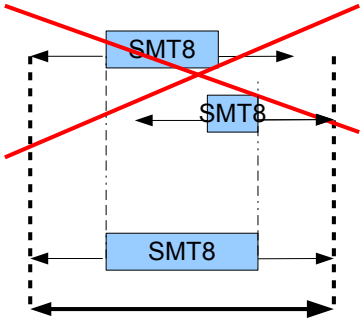

Figure 2.5: In the case where two triggers overlap, the global trigger will create a longer event in order to avoid having two events with the same content [71].

Table 2.1: The triggers in IceCube.

Name	Description
InIce SMT8	8 HLC Hits in 5 μs
String trigger	5 HLC Hits in 1.5 μs within 7 adjacent DOMs on one string
Volume trigger	4 HLC Hits in 1 μs within a cylinder of r=175 m and h=75 m
SLOP	Search for low velocity track-like signature
Fixed Rate trigger	Triggers at a fixed rate: 0.003 Hz
DeepCore SMT3	An SMT3 trigger on DeepCore DOMs

example the SMT8 trigger will be flagged if eight or more HLC Hits are detected within a 5 μs time window. In case of a SMT8 triggered event, data will be recorded from -4 μs to 6 μs around the trigger time to record the early and late Hits [70].

Other triggers can save data for a longer time. For example the Slow Particle trigger (SLOP) records data for ≈500 μs or more. The triggers are combined into a global trigger to avoid that 2 different events are created with the same content in a case where for example the SMT8 and the SLOP trigger would be flagged. The global trigger allows also to merge several trigger windows into one single event. For example, if two SMT8 triggers are flagged such that they overlap each other, only one longer event is created (see Fig. 2.5).

The different triggers are summarised in Table 2.1. For more detail, we refer the reader to [70].

2.4.2 Filters

After the triggering, one speaks about the events as level 0. The data rate (number of events per second) is of the order of 2.5 kHz. This high rate represents 1 TB per day of data. The transfer of the data to the Northern Hemisphere is achieved by satellites with a total maximum bandwidth of about 100 GB per day [70]. Consequently, it is necessary to reduce the amount

of data after triggering by at least a factor 10. This is the purpose of the filtering. After this process, the filtered events (named level 1) have a rate of about 100 Hz.

Several filters have been designed. They all try to identify an event that could be relevant for some specific analyses. The various analyses in ICECUBE have resulted in a whole suite of filters. Only the filters used in the analysis presented in this thesis will be described.

The most important filter when searching for muon neutrinos is the **MuonFilter**. Like most filters it is based on simple and fast reconstructions and simple quality parameters. The reconstructions will be explained in detail in Section 3.2. The two main reconstructions performed at the South Pole and that are used by the filters are LineFit and PoleMuonLlh. LineFit tries to fit a line through all the DOMs that detected light. PoleMuonLlh is a likelihood fit with only one iteration that uses LineFit as a seed.

The first cut of the MuonFilter is based on LineFit and behaves differently in function of the zenith angle θ and the number of DOMs that detected light (this is called NChannels or NChan)

$$\text{NChan} \quad \geq 8 \qquad \text{if } \theta_{\text{LF}} > 70^\circ \tag{2.9}$$

$$\text{NChan} \quad \geq 10 \qquad \text{if } \theta_{\text{LF}} \leq 70^\circ . \tag{2.10}$$

After this first cut, the events are divided in up-going and down-going based on the PoleMuonLlh reconstruction. An event is down-going if the zenith angle as reconstructed by PoleMuonLlh θ_{Llh} lies inside $0^\circ \leq \theta_{\text{Llh}} < 78.5^\circ$ and up-going if $78.5^\circ \leq \theta_{\text{Llh}} \leq 180^\circ$. These definitions of up and down-going are specific to the MuonFilter. In the analysis described in the current thesis, down-going events are defined as $0^\circ \leq \theta \leq 90^\circ$ and up-going events are defined as $90^\circ < \theta \leq 180^\circ$. If Q_{tot} is the total recorded charge of the event and LogL the value of the minimised loglikelihood, the cuts are

$$\text{If up-going: } \frac{\text{Logl}}{(\text{NChan}-3)} \leq 8.7 \tag{2.11}$$

$$\text{If down-going: } \begin{cases} \log_{10}(\text{Qtot}) \geq (3.9 \times \cos(\theta) - 0.5) + 2.6 & \text{If } \theta_{Llh} > 60^\circ \\ \log_{10}(\text{Qtot}) \geq (0.6 \times \cos(\theta) - 0.5) + 2.6 & \text{If } \theta_{Llh} \leq 60^\circ \end{cases} \tag{2.12}$$

The other filter that will be used is the Extremely High Energy filter (**EHEFilter**). As one can guess from its name, it is used to select events with very high energy. The cut is simple, it is based on the number of photo-electron (NPE) detected

$$\log_{10}(\text{NPE}) \geq 3 . \tag{2.13}$$

There are many other filters that are designed for the search of cascade or low energy up-going events for example. Even though the current analysis searches for muon neutrinos, several filters were considered in this analysis but only the events that had passed the MuonFilter or the EHEFilter survived the different cuts performed on the data (the event selection will be the subject of the Chapter 4). Consequently, the final event selection has been optimised on events that passed one of the Muon or EHE Filters.

2.5 The South Pole ice

The properties of the ice at the South Pole are of critical importance for the ICECUBE detector. One of the reasons that ice was chosen as medium for a Cherenkov detector is because it has a longer absorption length than water. This allows to build a larger detector with the same number of optical modules [57]. Unfortunately, the ice has also a drawback, the light has a shorter scattering length than in water. The measurement of scattering and absorption in the ice are extremely relevant for the reconstruction algorithms that will try to find the primary direction of the neutrino from the detected signals. The different simulations used in ICECUBE are also dependent on the modeling of the ice because they need to reproduce the propagation of light in the detector as close as possible to reality.

2.5.1 Study of the ice

In order to study the properties of the ice, the optical modules are equipped with LEDs as described in Section 2.3.1. This was already the case with AMANDA where the first measurements were performed [72]. AMANDA was also equipped with several other light emitters either pulsed or continuous. The covered wavelengths went from 313 nm using a UV module (steady source) to 532 nm using a YAG laser (pulsed source). Thanks to this equipment AMANDA could measure several important ice properties as well as establish a relation between the depth and the age of the ice [73].

In ICECUBE, the flasher board is equipped with LEDs emitting light at 399 nm. This wavelength was chosen because it reproduces the light of the Cherenkov radiation that ICECUBE tries to detect. Amongst the 5160 DOMs, 16 are equipped with LEDs emitting at 350 nm, 370 nm, 450 nm and 500 nm in order to study wavelength dependent effects [74]. The light emitted from the flasher board is pulsed and can be detected by DOMs up to 0.5 km away. More data about the South Pole ice were taken during the deployment of ICECUBE. Between the drilling and the string deployment, dust loggers have been lowered in the water filled holes in order to study the dust concentration as a function of the depth [75].

2.5.2 Properties of the ice

It was discovered that the ice at the upper part of AMANDA was not pure enough. Indeed, the presence of air bubbles in the ice had as result to increase the scattering of light and this severely limited the precision of the reconstructions.

ICECUBE has been buried deep enough to avoid air bubbles (they disappear below 1400 m) but the ice is still not perfectly clear. Some impurities like dust have been trapped in the ice. The amount of dust at a specific depth depends on the dust concentration in the atmosphere at a certain time in the past. For example, the ice close to the bedrock at the very bottom of the glacier has been estimated to be 165 000 years old. The ice above the detector (1300 m) is

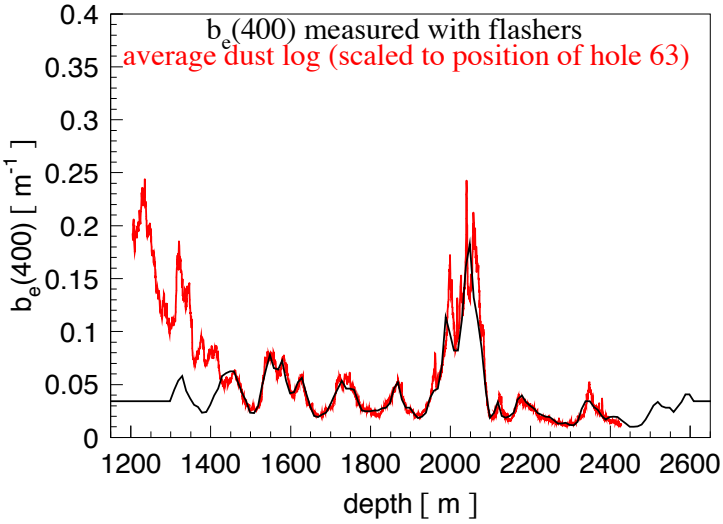

Figure 2.6: Comparison of the measurement from the dust logger (in red) with the effective scattering coefficient $b_e \equiv \frac{1}{\lambda_e}$ at 400 nm (in black)[74]. The effect of the air bubbles can be seen on the left part on the figure as well as the clear dust peak around 2000 m.

about 23 000 years old and is about 65 000 years old around the middle of the detector (2100 m) [73].

Since the dust concentration is depth dependent, the ice can be regarded as several layers of different purity which translates into different values for the absorption length and scattering length. The main result from the study of the dust in the ice is the discovery of a dust peak around 2000 m under the surface [72, 74].

The first detailed study of the scattering on small masses of material like dust was performed by Gustav Mie [68]. The scattering in ICECUBE is not isotropic but preferentially forward with respect to the incoming photon direction [72]. This leads to the definition of an effective scattering length λ_e defined as

$$\lambda_e \equiv \frac{\lambda_s}{1 - < \cos\theta >}, \tag{2.14}$$

where λ_s is the geometric scattering length (average distance between scatters) and θ is the deflection angle at each scatter [72, 57]. In the case of an isotropic scattering, $< \cos\theta >= 0$ and $\lambda_e = \lambda_s$. A study performed with AMANDA measured the scattering length at different wavelengths and at different depths. The results of this study are presented in Fig. 2.7. The effect of the air bubbles can easily be seen on this figure as well as the dust peak. The correlation between the concentration of dust and the scattering length can be observed in Fig. 2.6 when comparing the variation of the scattering length with the measurement from the dust logger [74]. From Fig. 2.6, one can deduce that for ICECUBE, at 400 nm, $\lambda_e \approx 25$ m on average.

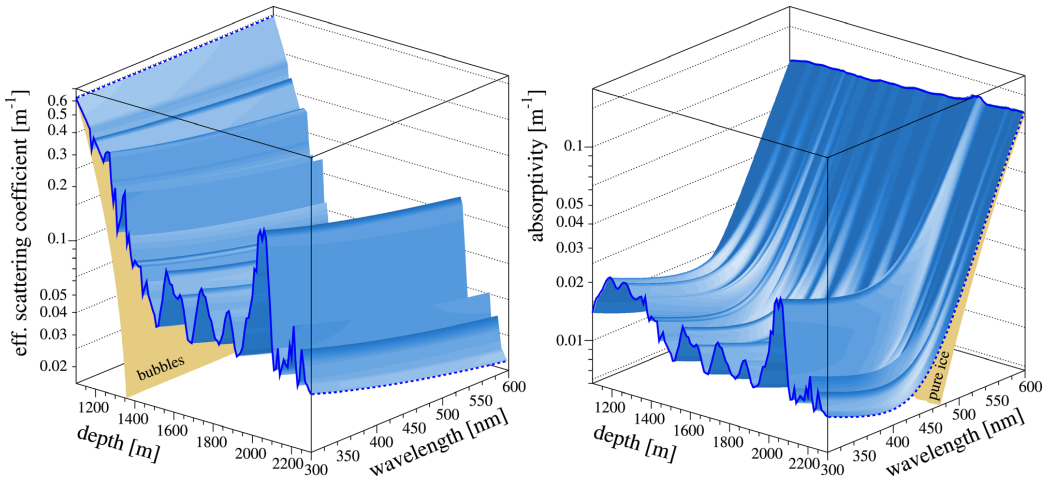

Figure 2.7: Maps of the effective scattering coefficient $b_e \equiv \frac{1}{\lambda_e}$ (on the left) and the absorptivity $a = \frac{1}{\lambda_a}$ (on the right) versus the depth and the wavelength [72].

The absorption length λ_a is defined as the length at which the probability of survival of the photons has dropped to $\frac{1}{e}$ [72]. In ICECUBE, the absorption length is strongly dependent on the depth. The effect of the dust layer appears very clearly in Fig. 2.7 and Fig. 2.8. From these figures, one can see that in ICECUBE, at 400 nm, $\lambda_a \approx 100$ m. One should remember that the strings in ICECUBE are 125 m apart and 72 m apart in DeepCore. At the bottom of the detector, below the dust layer, the ice is even clearer and the absorption length increases to ≈200 m.

2.5.3 Ice Models

In order to extract the different properties presented above, a model of the ice based on several parameters has been developed [72]. The way to extract these parameters consists of simulating the propagation of the light in the ice using a Monte-Carlo based on the ice model and fitting the result of the simulation to the recorded data by varying the parameters. With more precise simulation techniques and increasing amount of data the ice model evolved to describe more precisely the ice around the detector (see [74] for more detail). The result from two different ice models can be seen in Fig. 2.8.

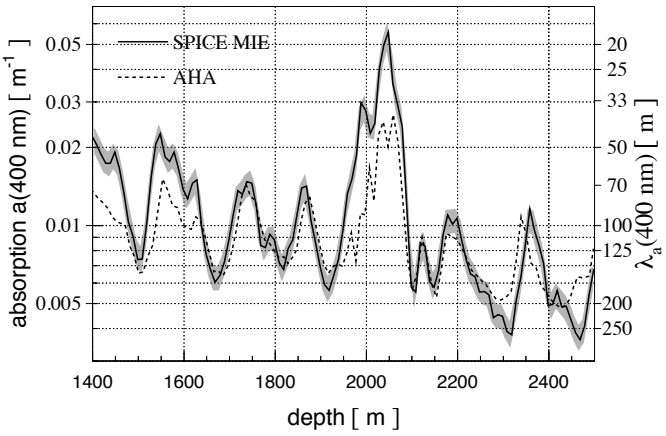

Figure 2.8: Absorption length at 400 nm versus depth for different ice models [74]. The AHA model is plotted in dashed line and the Spice-Mie model is drawn with a solid line. The grey area shows the uncertainties on the Spice-Mie model.

3

Event reconstruction and simulation

This chapter will be dedicated to the event reconstructions and simulations used in IceCube. After explaining the types of noise that can be expected in the detector and which methods are used to remove them from data, the event reconstructions used in this analysis will be described. Since the current analysis focuses on track events from muon neutrinos, only track reconstructions will be explained. The reconstructions are divided in two sections. The first one describes the initial fast reconstructions used at the South Pole and the second one will explain the more detailed and more time consuming reconstructions used "offline", after the data have been transferred to the Northern Hemisphere. The Direct-Walk algorithm to which I directly contributed will be explained in a dedicated section. Finally, an outline of the various event simulations used in IceCube will be given.

3.1 Background in the IceCube detector

Concerning our search for neutrinos from GRBs in the Northern Hemisphere, there are several types of background in the data collected by IceCube. One of them is the noise that mainly comes from the electronic equipment. Another one consists of mis-reconstructed down-going muons and finally there is an irreducible background of atmospheric neutrinos. Indeed, for an analysis like the one presented in this thesis that focuses on events from the Northern Hemisphere, the atmospheric muons are blocked by the Earth but it is impossible

to say for a neutrino if it is atmospheric or from astrophysics origin.

3.1.1 Elimination of noise Hits

The effect of electronic noise is the appearance of Hits uncorrelated with any physical events. The presence of these fake Hits can dramatically affect the precision of the reconstructions. Such noise is mainly caused by rare nuclear decay in the glass spheres of the DOMs as well as thermal emission of electrons in the PMTs (dark noise). The fact that the dark noise dominates the total amount of noise in the detector is due to the special low radioactive glass that was selected for the DOM as well as the location of ICECUBE. Indeed, the South Pole is a region where human activity as well as environmental effects have very little influence. Furthermore, the kilometer of ice above the detector acts as a natural shield against most cosmic radiation.

Several cleaning algorithms have been developed in order to remove noise Hits from the data. The general idea of such a cleaning algorithm is to search for isolated Hits in time and in space.

In the context of the analysis presented here, a more advanced cleaning procedure named **HiveSplitter** will be described in detail. HiveSplitter is originally designed to split the Hits of an event that would contain more than one particle in order to create separate events, each containing only the Hits belonging to one specific particle. However, this algorithm can also be used as a noise cleaner and this is what has been done in the current analysis (for a detailed description of splitters, see [76]).

The principle of HiveSplitter (like all splitters) is to construct clusters of Hits belonging to one particle. In the end of the procedure, the Hits that do not belong to any cluster are considered as noise, hence the cleaning ability of a splitter. The algorithm starts by sorting Hits in time and constructs clusters of Hits in the following way. Every Hit is surrounded by its **Individual Active Volume** (IAV) which is an element of volume around the Hit as well as a window in time. When several IAV overlap, a cluster is formed. The details of the values of the time and space windows can be found in [76].

Once a cluster is formed, a **Cluster Active Volume** (CAV) is defined in space and in time such that only Hits within the CAV will be added to the cluster. Once new Hits are added to the CAV, due to their timing information, the CAV moves in time and this may result in decreasing the cluster size because the IAV of early Hits may drop off the cluster. One can say that the cluster comes to life, grows up and dies when it reaches its lifetime[1]. In the end of the procedure, the clusters that fulfill certain size criteria are considered as physics events and the others are considered as noise.

The efficiency of HiveSplitter is due to several improvements in the definition of space and time window sizes with respect to previous algorithms. The parameters that define the horizontal and vertical components of the space window are chosen to be discrete because only a

[1] A more detailed description of HiveSplitter can be found at `http://software.icecube.wisc.edu/icerec_trunk/projects/IceHive/icehive.html`.

specific increase of a parameter will add a DOM to the cluster. A limit in the vertical direction constitutes also an improvement from previous algorithms. Furthermore, the choice of the size of the horizontal window takes into account the hexagonal shape of the detector in order to treat properly any border effect that could reduce the efficiency of the splitter (see [76] for details).

3.1.2 Mis-reconstruction and splitting of events

The main source of background is formed by the mis-reconstructed atmospheric muons from the Southern Hemisphere. There are several reasons why an event can be mis-reconstructed. The main types of mis-reconstructed events are the muons entering the detector with a nearly horizontal direction, the muons passing close to a corner of the detector and the coincident events.

If a muon direction is nearly horizontal, a small error in the reconstruction makes a down-going event to become a reconstructed up-going event. A particle passing close to the border of the detector or even worse, in a corner of the detector can generate light that will reach the detector mimicking an up-going particle.

A coincident event happens when two or more particles leave some light in the detector within the same trigger time window. The system creates then an event containing the Hits generated by several particles. The reconstructions will usually fail because they try to fit one particle to the Hit pattern (with the exception of IceDwalk, see Section 3.4).

The solution to this problem is to split the event in order to obtain separate events each of them containing the Hits related to one particle. As explained in the previous section, this is usually done by constructing clusters. However, due to remaining noise hits and the fact that there exists a horizontal dust layer near the middle of the detector, sometimes events may be split by mistake (see Section 2.5.2 for more details about the dust layer).

Usually a splitting algorithm is followed by a recombination algorithm. Such an algorithm tries to combine split events in case an event containing only one particle would have been split erroneously.

3.2 Reconstructions at the South Pole

Since power and computing resources are very limited at the South Pole, the reconstructions that are run before the filtering procedure must be fast and efficient. The most important reconstructions run at the South Pole are **LineFit** and a likelihood based reconstruction named **PoleMuonLlhFit**. More evolved algorithms are applied on a small subset of events but they will not be discussed here because they are not used in the current analysis. This section will focus on track reconstruction and will not enter the difficult topic of cascade reconstruction. Since track events can be reconstructed with a higher accuracy than cascade events they are more suitable for a point source analysis. For this reason the current analysis focuses only on

track events.

It should be noted that simple cleaning and splitting algorithms are run on the data before performing the reconstructions.

3.2.1 The LineFit algorithm

A description of the analytical LineFit algorithm can be found in [77] and [78]. The idea of LineFit is very simple; it tries to construct a track based on Hit times and DOM positions. It neglects the fact that the light emission follows a particular profile (Cherenkov cone) as well as the scattering of light in the ice. The purpose of such a simple algorithm is to be used as a seed for more complex reconstructions often based on likelihood maximisation techniques.

In more detail, if t_i is the time of the Hit i and $\mathbf{r}_i$, the position of the DOM that recorded the Hit i, one tries to minimise the χ^2 function defined as [77]

$$\chi^2 = \sum_{i=1}^{N_{Hit}} \rho_i^2 = \sum_{i=1}^{N_{Hit}} (\mathbf{r}_i - \mathbf{r} - \mathbf{v} \cdot t_i)^2 \tag{3.1}$$

with respect to the free parameters that are the interaction vertex position $\mathbf{r}$ and the speed $\mathbf{v}$ of the particle[2] along the track. The advantage of this method is that it can be solved analytically [77].

The results of this fit (vertex point and direction) are then used as seed for Likelihood based reconstructions. However, it has been shown that the results of the likelihood fit are very dependent on the seed used. Hence, one might be penalised by using a too simple algorithm to create the seed [78]. This led to the development of the **improved LineFit** which is the algorithm that was applied to the data used in this work.

This improved algorithm solves two important drawbacks of LineFit [78]. First, it removes Hits which are likely due to scattering in the ice by searching for a Hit happening a certain time t after another Hit in a defined neighbourhood. Since the LineFit algorithm does not take into account the scattering of light in the ice, the fit is misled by scattered Hits happening after the particle has passed the area. Second, it uses a Huber fit instead of minimising a χ^2. This makes the algorithm more robust to noise. Indeed, noise Hits that were not removed in the cleaning process can have an important impact on the fit due to the quadratic nature of the fit.

The Huber function to minimise, H, can be written [78]

$$H = \sum_{i=1}^{N_{Hit}} \phi\left(\rho_i(t_0, \mathbf{r}, \mathbf{v})\right), \tag{3.2}$$

where t_0 is the time corresponding to the interaction vertex and $\phi(\rho)$ is the Huber penalty

$$\phi(\rho) = \begin{cases} \rho^2 & \text{if } \rho < \mu \\ \mu(2\rho - \mu) & \text{if } \rho \geq \mu \end{cases}, \tag{3.3}$$

[2]The speed $v = |\mathbf{v}|$ is not exactly the speed of the particle. It is the projection to 1 dimension of the light propagating in the detector.

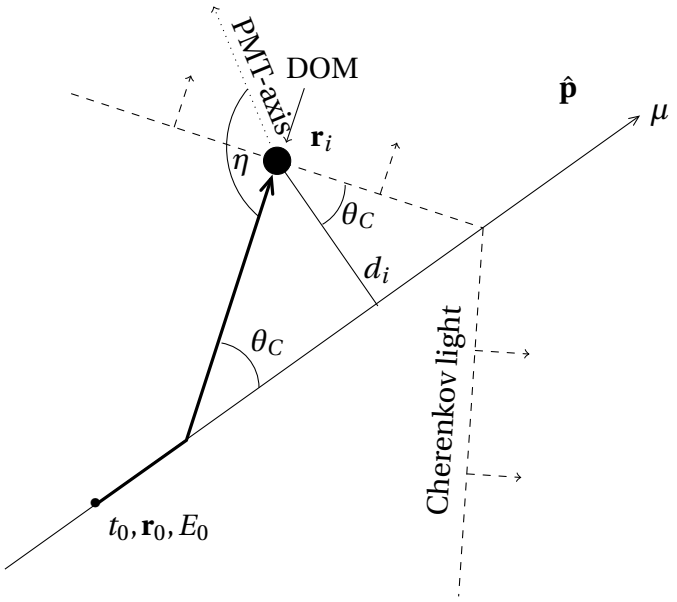

Figure 3.1: Explanation of the different parameters used in the Likelihood reconstruction [77].

where the value μ has been optimised using simulations and is equal to 153 m. Once the fit is performed, the Hits with $\rho \geq \mu$ are tagged as noise Hits and a χ^2 minimisation as in Eq. (3.1) is performed on the cleaned Hits. This improves the LineFit accuracy but has the cost of a longer processing time [78].

3.2.2 Likelihood reconstruction

Once a first guess algorithm like LineFit has been performed, a more evolved method is applied using the first guess as a seed. Like in the previous section, the goal is to extract the value of several track parameters by fitting the data. The differences with respect to the previous section are the fit method used, a maximum likelihood in this case, and the fact that the cone shape of the light emission is taken into account.

Following [77], the parameters that the likelihood tries to extract are $\mathbf{r}_0$, a point on the track, the time t_0 at which the particle position is $\mathbf{r}_0$, the energy E_0 at this same position and finally, the direction of the track $\hat{\mathbf{p}}$. The photons are assumed to be emitted at the constant Cherenkov angle θ_c along the track. These parameters are represented in Fig. 3.1.

According to the geometrical configuration described in Fig. 3.1, the time t_{geo} at which the photons are expected to be detected by a DOM is

$$t_{\text{geo}} = t_0 + \frac{\hat{\mathbf{p}} \cdot (\mathbf{r}_i - \mathbf{r}_0) + d_i \tan\theta_c}{c}, \tag{3.4}$$

where d_i is the distance between the track and the DOM i (located at a position $\mathbf{r}_i$) and c is the speed of light in vacuum.

From t_{geo}, one can construct the residual time $t_{res} \equiv t_{Hit} - t_{geo}$. The next step in the likelihood reconstruction is to define the Probability Density Function (PDF) for t_{res}. This PDF will depend on the different parameters described above such that it can be written as $p_1(t_{res}|\mathbf{a})$, where $\mathbf{a} = (\mathbf{r}_0, t_0, E_0, \hat{\mathbf{p}})$. This PDF can be constructed in different ways. It is based on simulation of propagation of light in the ice (of course this depends on the ice model).

The simplest PDF that can be chosen considers for each DOM the detection of several single photons. The reconstruction based on this simple PDF is named **Single Photo Electron fit** (SPEFit). This is the algorithm used by the different filters at the South Pole (where it is called PoleMuonLlhFit). Another possible algorithm named **Multiple Photo Electron fit** (MPEFit) uses the PDF for detecting a number N of photons (instead of the PDF of detecting 1 photon as for SPE) [77].

3.3 Offline Reconstructions

Once the data are filtered and transferred to the Northern Hemisphere, more computing power is available and the events are re-processed with more time consuming reconstructions. Most of these reconstructions are likelihood reconstructions as explained in the previous section. The PDF used can change in order to use more information from the event. For example, one could consider the product of a PDF for time arrival of the photons with a PDF for the expected charge in the DOMs (see [78] for more details).

Another improvement consists of the use of an iterative procedure. At the first iteration, the reconstructed track resulting from the maximised likelihood is used as seed. The point $\mathbf{r_0}$ is taken to be the center of gravity of the Hits of the seed track. The time t_0 is calculated to correspond to the Cherenkov expectation and the zenith and azimuth angles are chosen randomly. If the value of the likelihood maximisation is higher than the value obtained at the first maximisation, the new reconstructed track becomes the seed for the next iteration. If the new maximisation is not better than the previous one, the seed remains unchanged for the next iteration. Usually, only few iterations are performed because of the required computing time.

The most evolved reconstruction used in this analysis is **MuEx4MPE** [79]. It allows a reconstruction of direction and energy. It is a MPE likelihood reconstruction that uses a more complicated likelihood which is a function of direction and energy. Prior to this reconstruction the HiveSplitter algorithm is used to further improve the cleaning.

3.4 The Direct-Walk reconstruction algorithm

The Direct-Walk algorithm was initially developed as a first-guess reconstruction for AMANDA [77]. It has been updated for the ICECUBE configuration and was given the ability to reconstruct several tracks per event. The name was also updated to become IceDwalk.

Below a brief description of the procedure is provided[3].

The algorithm starts by constructing **track elements** (or TEs) which are straight lines connecting hit pairs. These pairs must satisfy specific distance and time separation criteria. The next step associates Hits to these TEs. The criterion to associate a Hit to a TE is based on the value of t_{res} as defined above as well as the distance d represented on Fig. 3.1. Once the Hit association procedure is over, the algorithm keeps the TEs that satisfy various quality parameters.

The selected TEs are called **track candidates**. Because several track candidates could originate from a single particle track, the algorithm will cluster the track candidates based on the angle and the distance between them. The cluster of track candidates forms a **jet**. Following a similar procedure, the jets are then merged through an iterative procedure. If a merger of two jets gives a jet that satisfies the merging criterion with a third one, the new jet is merged with this third one and it continues until no jet can be merged anymore. If the resulting jets satisfy a quality condition, they are considered as tracks. The IceDwalk algorithm can thus provide several reconstructed tracks for a single event.

The algorithm contains many parameters that can be optimised. From the minimum distance to form pairs to the maximum angle to merge track candidates or jets. There are three sets of parameters because there are three types of IceDwalk reconstructions. The first type, called **IC** uses all the available Hits and has the most stringent set of parameters, optimised for the geometry of the standard IceCube strings. The second type, called **I** uses the same Hits but has a looser set of parameters, optimised for the hybrid IceCube and DeepCore geometry, such that if the IC reconstruction fails, the algorithm tries to run IceDwalkI. If both IC and I fail, a third type of reconstruction is attempted using even more loose selection criteria (optimised for the DeepCore geometry) to look for low-energy tracks. This last type is called **DC**.

An optimisation of the parameters used in IceDwalk IC has been performed prior to the use of the IceDwalk reconstruction in this analysis. For this optimisation, several variations of 11 parameters around their default values were considered. This investigation was performed on neutrino simulations.

The difficulty resides in the fact that the more restrictive the parameters are, the better the reconstructed tracks are but the number of events where IceDwalk fails is also larger. To take this effect into account an objective function F was defined such that different parameter configurations were compared based on this function. If the median angular resolution obtained from the IceDwalk reconstruction is $\widetilde{\psi}$, the percentage of events reconstructed as upgoing while they are down-going is $\not{\mu}$ (and the opposite is $\not{d}$) and if the percentage of events on which IceDwalk succeeds is N, the objective function is

$$F = \frac{\widetilde{\psi} \times (\not{\mu} + \not{d})}{N}. \tag{3.5}$$

[3]The details of the IceDwalk algorithm are available at `http://www.iihe.ac.be/~ice3/ncfsdoc/IceDwalk.html`.

Table 3.1: Summary of the difference between the optimised IceDwalk IC and the default one.

	$\widetilde{\psi}$	$\mathscr{U}$	$\mathscr{d}$	N
Optimised	5.6°	3.6%	6.6%	83%
Default	5.9°	5%	7.4%	88%

Table 3.2: Values of the most relevant parameters for the IceDwalk IC reconstruction.

Dmin	Dtmarg	MaxDhit	Dthitmin	Dthitmax
120 m	250 ns	3 λ	-50 ns	250 ns

The best set of parameters is the one that minimises F.

It was found that the most relevant parameters are

- Dmin: Minimum distance between 2 Hits to form a TE.
- Dtmarg: Maximum time difference between 2 Hits to form a TE.
- MaxDhit: Maximum distance for a Hit to get associated to a TE.
- Dthitmin: Minimum time residual between a Hit and a TE for association.
- Dthitmax: Maximum time residual between a Hit and a TE for association.

A summary of the difference between the default IceDwalk IC and the optimised IceDwalk IC can be found in Table 3.1. After this optimisation, we realised that the parameter Dmin does not affect the quality of the reconstruction but only the number of events on which the reconstruction will succeed. Hence, the value of Dmin was slightly lowered from the optimised value. The values of the five most relevant parameters for the IceDwalk IC used in this analysis are presented in Table 3.2. The parameter MaxDhit is given as a function of the scattering length λ. This scattering length can take three values in function of the location in the detector (above the dust layer, in the dust layer and below the dust layer).

Because of the various steps of the IceDwalk algorithm, it turns out to be robust with respect to noise. Due to this robustness, IceDwalk can also be used as a Hit cleaner. Once the algorithm has finished processing the data of an event, it returns a direction as well as the set of Hits associated to the final reconstructed tracks. One can then run another reconstruction like LineFit on the Hits that were selected by IceDwalk. This hybrid reconstruction is named **LineFit4Dwalk** and it is the Direct-walk based reconstruction that will be used in this analysis. The LineFit reconstruction has the advantage of being an analytical procedure from which one can extract the speed v as explained in the Section 3.2.1.

3.5 Event simulations in ICECUBE

Two simulations were used in this analysis. The first one generates neutrinos and the second one generates cascades induced by cosmic rays. In both cases, the simulations start by generating primary particles following a specific energy spectrum. Then these primary particles are propagated through the different media (air, ice, rock) taking into account the production of secondary particles and the different energy loss mechanisms [69].

When the simulation propagates particles in the ice, it takes care of the Cherenkov emission as well as the scattering of the produced photons. This specific part of the simulation uses ice models (see Section 2.5.3) and assumes that the ice properties vary only in function of the depth. Once the photon propagation phase is over, the DOM response to these photons is simulated and the entire data treatment is reproduced in the same way as it is done for real data.

The simulation code which generates the background induced by the cosmic rays is CORSIKA (COsmic Ray SImulation for KAscade) [80]. The one used for neutrino generation is named NuGen and is based on the program ANIS [81]. For efficiency reasons, the NuGen algorithm forces all generated neutrinos to interact in the specified volume. In order to take this effect into account when dealing with NuGen events, one must weight the events by the probability of interaction. The weight w_i of an event i is provided as a parameter called **OneWeight** in all simulated data and does not need to be calculated by the user.

These weights are also used in the re-normalisation procedure to reflect a certain neutrino energy spectrum. If one wants to use a NuGen simulation following a flux $\frac{d\Phi}{dE}$, every event of the NuGen sample will have to be weighted by $w_i \times \frac{d\Phi}{dE}$ to represent the actual event rates in the ICECUBE detector.

4

Event Selection

After the introduction to the cleaning and reconstruction algorithms in ICECUBE in the previous chapter, this chapter will be dedicated to the use and the combination of these algorithms to extract the relevant information from the data for the final analysis. The main purpose of the event selection presented in this Chapter is to extract possible signal events that would produce a muon induced track in the detector.

The event selection is composed of two parts. The first one is a pre-selection named **QualDist** that uses a novel method developed for this thesis research. The second part uses a Boosted Decision Trees (**BDT**) algorithm to efficiently discriminate background events from possible signal events. A detailed description of these two parts will be followed by the explanation of the various variables that allow to quantify the performance of the event selection.

The starting point of the event selection is the so-called **Level2** of the standard IceCube data processing chain. This consists of all ICECUBE events that have passed at least one of the physics filters and it contains offline processing and reconstructions (see Section 3.3 for details). A selection is made from the Level2 data since we use only the MuonFilter and the EHEFilter. In this chapter, all relative amounts of signal and background will be given with respect to the Level2 rate r_{L2} for events having passed one of these two filters.

During the first phases of the development of the event selection, more filters were used. However, it turned out that the other filters were not increasing the amount of relevant signal events but were increasing the amount of background. This is an interesting result on its own since it confirms the high efficiency of the MuonFilter.

The dataset used as signal consists of 1000 NuGen files generated with the Spice-Mie ice model (see Section 3.5 for details) from which only up-going events have been selected. These NuGen events need to be weighted to take into account simulation effects. During

this weighting process one has to assume a specific energy spectrum. As explained in Section 1.3.1, the generic spectrum generated by Fermi acceleration is E^{-2}. In order to be as model independent as possible, this generic spectrum will be used to weight the NuGen events through the analysis (i.e. $\frac{d\Phi}{dE} \propto E^{-2}$). Furthermore, using this spectrum allows a direct comparison with other analyses since it is used as a generic benchmark spectrum.

The background sample is formed from 38 samples of 2 hours of real data when no GRBs were detected. This background sample is called a **burn sample**.

4.1 Pre-selection

From the comparison of the IceDwalk reconstruction with other types of reconstructions, we realised that depending on the type of reconstruction, the types of mis-reconstructed events were different. For instance, IceDwalk seems to be robust with respect to the noise but has the tendency to fail the reconstruction of events that have a nearly vertical or horizontal direction. On the other hand, likelihood based reconstructions like MPEFit do not have this tendency of mis-reconstructing events coming from a specific direction but they are more sensitive to noise.

Given these observations, the idea arose to combine several reconstructions to gain from their respective efficiencies. The first attempt to combine reconstructions was to build a selection that would keep an event if a certain fraction of the used reconstructions were of good quality. In order to define a good quality reconstruction, a quality parameter was defined for every reconstruction and ranges of values for these quality parameters were defined.

The problem with this first attempt is the enormous number of parameters. One should have optimised on the number of reconstructions to be used, the fraction of good quality reconstructions of an event to be kept and on all the ranges of the quality parameters that define good quality reconstructions. Due to this drawback, another approach was followed. Instead of having as many conditions as reconstructions to fulfill the acceptance of an event, it is simpler to build a distribution containing all the quality parameters of all the considered reconstructions and to perform a cut on this continuous distribution.

4.1.1 QualDist

Such a distribution was named QualDist for Quality Distribution. It removes the necessity of defining a range for the quality variables of every reconstruction and allows to select the ideal set of reconstructions to be used in a single optimisation process.

QualDist combines the quality parameters of the reconstructions by summing them. This requires that all quality parameters have comparable values for well-reconstructed events. Since the various parameters had very different ranges of possible values, they were all renormalised to lie between 0 and 1. The value 0 corresponds to a mis-reconstructed event and the

value 1 corresponds to a perfectly-reconstructed event. A first QualDist possibility is then

$$\mathrm{QD} = \sum_{i}^{N_{\mathrm{reco}}} q_i \,, \tag{4.1}$$

with QD the QualDist value of the event and q_i the quality parameter of the reconstruction i. This definition of QualDist can be improved by associating a weight to every reconstruction. Indeed, all reconstructions are not equivalent; some have a better performance than others and hence should have a higher weight in the distribution. Another improvement is to subtract the quality parameter if the reconstruction output is a down-going track.

If W_i is the weight associated to the reconstruction i and if $a = 0$ for up-going reconstructed tracks and $a = 1$ for down-going reconstructed tracks, we have

$$\mathrm{QD} = \sum_{i}^{N_{\mathrm{reco}}} (-1)^a W_i \times q_i \,. \tag{4.2}$$

This is the definition of QualDist as used for the pre-selection of events. The weights W_i are calculated using a two step numerical procedure explained in the next section.

The used quality parameter depends on the reconstruction procedure. In the case of LineFit reconstructions (including LineFit4Dwalk), the quality parameter is $\beta = \frac{v}{c}$ where v can be interpreted as the particle velocity in case of tracks as explained in Section 3.2.1 and c is the speed of light. In the case of likelihood reconstructions the quality parameter is the Reduced Log-Likelihood (**RLogL**) value of the likelihood fit. This RLogL value is defined as the ratio of the negative Log-Likelihood fit (LogL) to the number of degrees of freedom n_{dof} [82]. Since there are 5 parameters in the likelihood fit, we have

$$\mathrm{RLogL} = \frac{\mathrm{LogL}}{n_{\mathrm{dof}}} = \frac{\mathrm{LogL}}{n_{\mathrm{ch}} - 5} \,, \tag{4.3}$$

with n_{ch}, the number of channels (i.e. the number of DOMs used in the fit). The distributions of RLogL for MPEFit and β for LineFit4Dwalk are shown in Fig. 4.1.

Since all quality parameters $q_i \in [0,1]$, we define the transformations

$$q_{\mathrm{Llh}} = \begin{cases} \frac{6}{\mathrm{RLogL}} & \text{if} \quad \mathrm{RLogL} \geq 6 \\ 1 & \text{if} \quad \mathrm{RLogL} < 6 \end{cases} \tag{4.4}$$

$$q_{\mathrm{Lf}} = \begin{cases} \beta & \text{if} \quad \beta \leq 1 \\ 2 - \beta & \text{if} \quad \beta > 1 \end{cases} \tag{4.5}$$

with q_{Llh} the quality parameter of the likelihood based reconstructions and q_{Lf} the quality parameter of LineFit reconstructions.

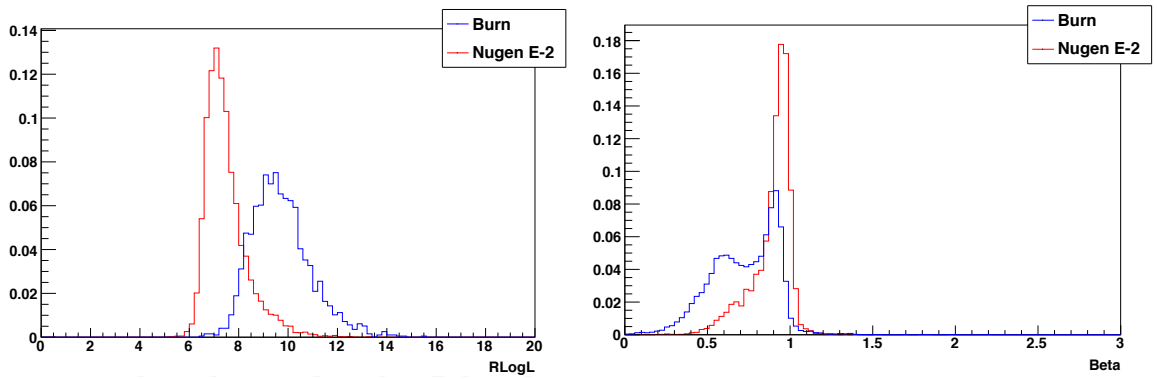

(a) MPEFit RLogL (b) LineFit4Dwalk β

Figure 4.1: Example of QualDist variables. Panel (a) shows the distribution of the RLogL variable associated to the MPEFit reconstruction. Panel (b) shows the distribution of the β variable associated to the LineFit4Dwalk reconstruction. In both panels, the simulated signal is in red and the background is in blue.

4.1.2 Optimisation procedure

In order to combine the various reconstructions in the most efficient way, an optimisation of the reconstruction weights has been performed. This optimisation is based on simulations and uses as signal only well-reconstructed up-going NuGen events. A well-reconstructed event is defined as an event which is reconstructed within 5° of the simulated neutrino by at least one of the considered reconstructions. Unless it is specified differently, all references to signal in this section will mean well-reconstructed up-going NuGen events.

The optimisation is performed in two steps. The first step consists of associating five possible weights to each reconstruction and to test all possible combinations of weights and reconstructions. The five possible weights are 0; 0.5; 1; 1.5 and 2. If there are N reconstructions, there are then 5^N possible sets of weights. The optimal set is found by selecting the one that maximises the amount of signal while reducing the background to a specific level.

At the end of the first step, each reconstruction has a weight associated to it. The reconstructions that have a weight of 0 do not contribute to QualDist and are thus removed from the optimisation. In this way, the weight optimisation also allows to define the most appropriate set of reconstructions to use.

The second step generates random weights from a Gaussian distribution centered at the value of the weights obtained at the first step and with a standard deviation of 0.5. Similarly as for step 1, the selected weights are the ones that maximise the signal efficiency for a specific background level.

Since the choice of this specific background level has an influence on the optimal set of weights, three background levels have been used in the QualDist optimisation. These possible

Table 4.1: Comparison of signal efficiencies for three possible BDT cuts applied after three different QualDist optimisations (see the text for details). The QualDist optimisation that reduces the background level to $0.01 \times r_{L2}$ is the most efficient one.

QualDist optimisation	BDT cut at $r = 1$ mHz	BDT cut at $r = 2$ mHz	BDT cut at $r = 4$ mHz
$0.05 \times r_{L2}$	42%	67%	86.5%
$0.01 \times r_{L2}$	64%	76%	87.5%
$0.005 \times r_{L2}$	62%	75%	86%

Table 4.2: Weights associated to the five selected reconstructions. These weights are the results of a two step numerical optimisation as explained in the text.

LineFit4DWIC	LineFit	SPEFit	MPEFit	LineFit_HiveSplit
0.29	0.63	1.58	3.5	0.33

background levels are $0.05 \times r_{L2}$; $0.01 \times r_{L2}$; $0.005 \times r_{L2}$. The difficulty with these three possible background reductions is that it is impossible to know which one is the best before having applied the Boosted Decision Trees (BDT) as we will see in the next section. This comes from the fact that the event selection has to be the most efficient at the final level, where the statistical method will be applied. Thus, which QualDist selection will be the most optimal one after the application of the BDT on the remaining data, is a difficult question to answer a priori.

The method that was applied to resolve this is the following. After having optimised through the two step procedure the three possible background levels, a BDT algorithm (see next section) was trained and applied to the three optimised QualDist outputs. The signal efficiencies were then compared after the BDT selection. Once again, the signal efficiencies have to be compared at a specific background level. Since the previous IC86 GRB analysis had a final background rate of 3.8 mHz, it was decided to compare the signal efficiencies at 1 mHz, 2 mHz and 4 mHz. The signal efficiencies of the three possible QualDist optimisations after three possible BDT cuts are shown in Table 4.1.

Given the results shown in Table 4.1, the QualDist optimisation that yields the highest signal efficiency while reducing the background to $0.01 \times r_{L2}$ seems to be the best optimisation. Using this optimisation, the finally selected reconstructions and their associated weights are shown in Table 4.2.

Because of the numerical optimisation, one has to make sure that there is no over-training in the weight optimisation. Indeed, a too precise optimisation could be extremely well adapted to the set of data used in the optimisation but the results could be far from optimal when applied to a different set of data. This verification is performed by super-imposing the QualDist output for the sample used in the optimisation (training sample) and another

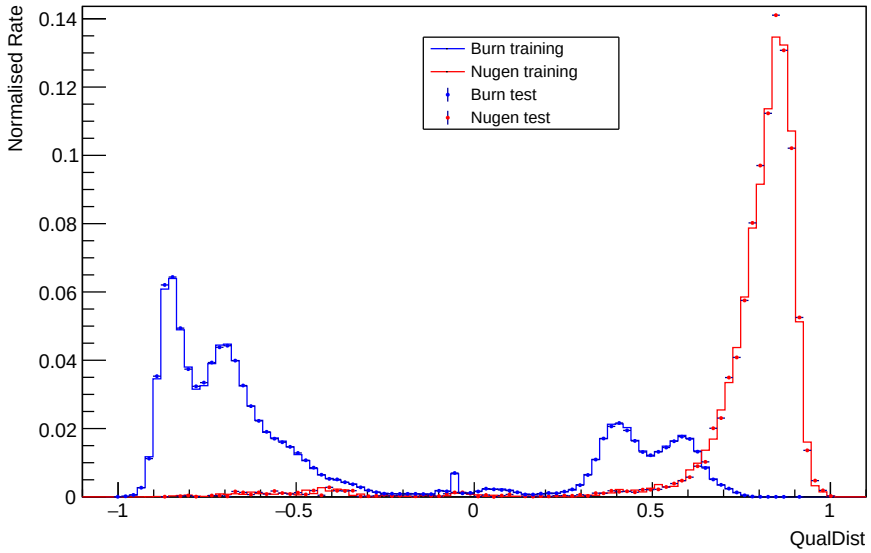

Figure 4.2: QualDist distribution for signal in red and background in blue. The solid lines indicate the training samples used for the optimisation of the weights and the markers indicate the test samples.

Table 4.3: Signal efficiencies for well-reconstructed signal events and all signal events as well as the background rate after the QualDist selection (QualDist level) as explained in the text.

Well-reconstructed signal	All signal	Background
90.5%	80%	0.35 Hz

sample (test sample). This over-training verification is shown in Fig. 4.2 from which it is seen that no over-training has occurred.

The QualDist distribution for signal and background can also be seen in Fig. 4.2. A more informative representation of QualDist is shown in Fig. 4.3. In this figure, one can read the signal efficiency on a linear scale and the background efficiency on a logarithmic scale. This allows to precisely quantify what a given QualDist cut can achieve. Both signal and background efficiencies are calculated with respect to Level2 data (and only for Muon and EHE Filtered events as mentioned before).

Since the selected optimisation reduces the background by a factor one hundred, the corresponding QualDist cut value is 0.671. The signal efficiency and the background rate after this cut (at QualDist level) are summarised in Table 4.3.

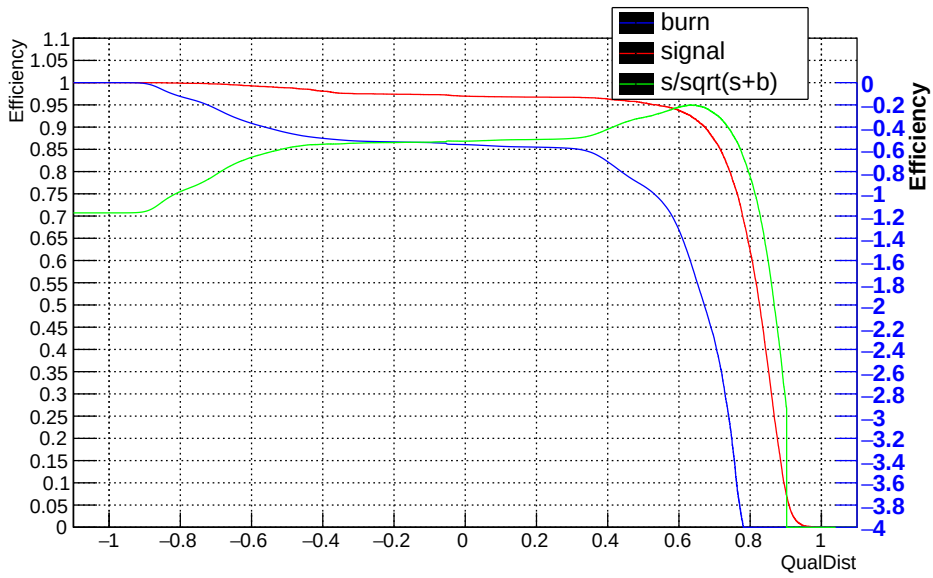

Figure 4.3: QualDist distribution for signal in red and background in blue. The signal efficiency in linear scale can be read from the left axis while the background efficiency in logarithmic scale can be read from the right axis. The green line corresponds to a possible measure of the efficiency of the cut.

4.2 Boosted Decision Trees

A decision tree is a simple method that allows to classify an event either as signal or background. A decision tree is composed of **nodes** as can be seen in Fig. 4.4. The first node is called the **root node** and the final ones are called **leaf nodes**. The decision tree is built by using a signal sample and a background sample. This phase is called the **training** (more information about BDTs and their implementation can be found in [83]).

The training for a tree works as follows. At each node the algorithm performs a cut on a given variable such that it maximises the signal-background separation. Once arrived at a leaf node, the events of the node are classified as signal (resp. background) if the majority of events are signal (resp. background) events. Since the algorithm searches for the variable and the cut that maximises signal-background discrimination, it is possible that some efficient variables are used at several nodes while less useful variables are not used at all. In this way the algorithm will only use the efficient variables which makes it robust against variables that have a poor separation power.

There are several possible criteria to search for the optimal cut at each node. The criterion used in this analysis is the **Gini Index** [83]. If the purity p is defined as the ratio of the number of signal events to all the events at a given node (i.e. $p = \frac{S}{S+B}$), then the Gini Index is $p(1-p)$.

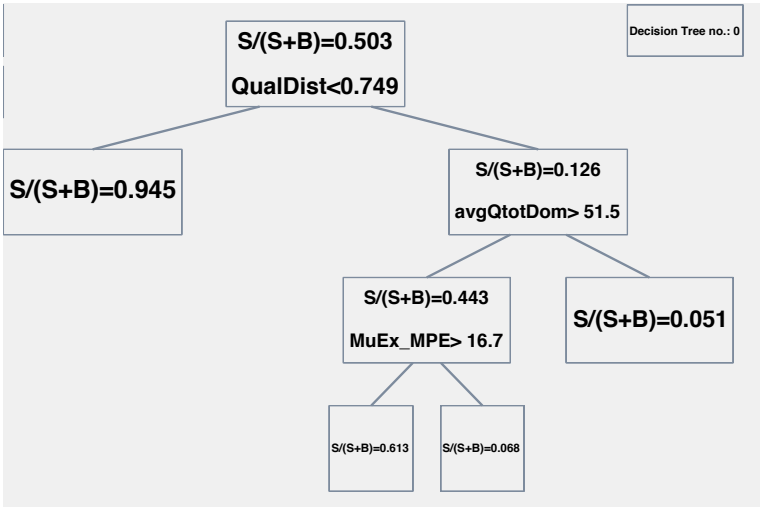

Figure 4.4: Example of a decision tree. At each node, starting from the root node, the most efficient cut on a variable is performed in order to increase the $\Delta G(p)$ between the parent node and the daughter nodes as explained in the text. At the leaf nodes, the events are classified as signal if $p > 0.5$ and background if $p < 0.5$.

At each node the algorithm selects the variable and the cut on that variable that will maximise

$$\Delta G(p) = G(p) - G(p_1) - G(p_2)\,, \tag{4.6}$$

where p_1 is the purity of the first daughter node and p_2 is the purity of the second one.

One might be tempted to build (or grow) a very long tree in order to get the most efficient signal-background separation. The risk of a large tree is that it would be extremely efficient on the trained sample but could perform very differently on any other sample. As for the QualDist method, this phenomenon is called over-training. There are several methods that can increase the performance of the decision tree without risking over-training.

The first method is called **boosting**. Instead of considering a single decision tree one might consider a large number of trees (a forest) such that each event receives a score based on the classifications of the various trees. The boosting procedure generates different weights for the events and grows trees one at a time adapting the weights at each tree. The purpose of the boosting is to increase the efficiency of the algorithm by boosting the weight given to misclassified events in the hope that they will be classified properly in the next tree.

Another possibility which is compatible with boosting is **bagging**. This procedure trains several forests on a re-sampled training sample and takes the average of the BDT output for each event. The re-sampling procedure is done by generating random weights for the events of the training sample.

In this analysis, the Toolkit for Multivariate Data Analysis (TMVA) has been used [83]. This suite has been developed at CERN and offers the possibility to use various machine learning algorithms. A brief comparison of several algorithms has been performed and the BDT with

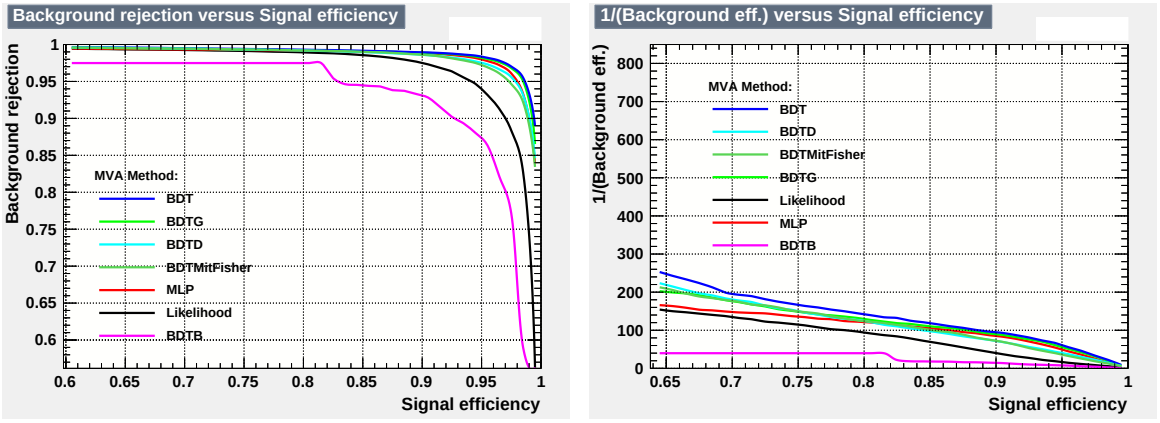

(a) (b)

Figure 4.5: Comparison of several multi-variate methods. The BDT with the AdaBoost boosting method gives the best performance.

the AdaBoost boosting method gave the best performance as shown in Fig. 4.5.

4.2.1 BDT variables

The question of which variables to use in the BDT is not trivial. Indeed, a variable could have a low discrimination power on its own but could become efficient when combined with several others in a BDT. Fortunately, the BDT procedure is very robust with respect to the introduction of variables with a low separation power. The method that was followed is to use as many variables as possible and to remove one by one those which do not contribute to the BDT.

The variable selection started with the choice of the cleaning algorithm. As explained in Section 3.1.1, the HiveSplitter cleaner was finally used in this analysis. After the QualDist selection (QualDist level), two cleaning algorithms were compared as well as the absence of any cleaning[1]. These two cleaning algorithms are HiveSplitter and another one called TWSRT. Several possible variables, including the Center of Gravity (**COG**) of all Hits, angles between several reconstructions and MuEx4MPE specific variables, were computed and compared based on the three possible cleaning solutions.

[1]It is useful to explain why LineFit run on HiveSplit selected Hits is used in QualDist while the HiveSplit cleaner has been chosen after the QualDist selection. The reason is that a first QualDist selection did not involve reconstructions on the HiveSplit selected Hits and later, after that the HiveSplit cleaner was chosen for the BDT variables, a new version of QualDist was optimised using LineFit run on HiveSplit selected Hits.

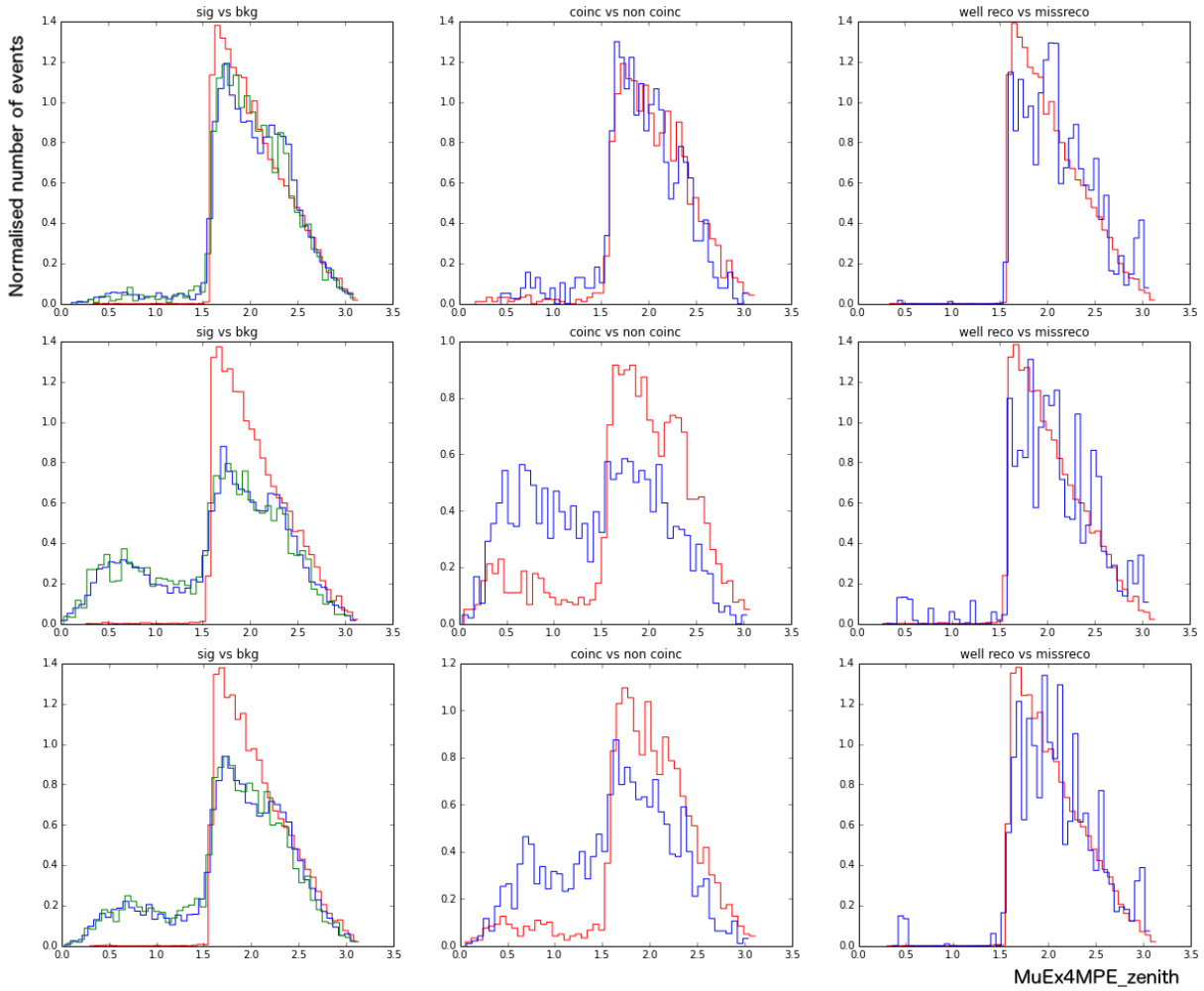

Figure 4.6: Comparison of the variable `MuEx4MPE_zenith` without cleaning (top), with HiveSplit cleaning (middle) and with TWSRT cleaning (bottom). This comparison has been performed on three subsamples, signal vs. background (left), coincident vs. non-coincident (center) and mis-reconstructed vs. well-reconstructed (right). In the case of the signal vs. background, signal is in red, background in blue and CORSIKA in green. The coincident events are in red and the non-coincident in blue and the mis-reconstructed are in blue and the well-reconstructed in red.

The comparison of the variables was based on different subsamples of events:

- Signal vs. Background,
- Well-reconstructed vs. Mis-reconstructed,
- Coincident vs. Non-coincident.

Based on these subsamples, it was possible to obtain an overview of the variable separation power. An example of the comparison of the various cleaning procedures for the `MuEx4MPE_zenith` variable using the different subsamples is shown in Fig. 4.6 where one can notice that the HiveSplit cleaning allows a better background/signal separation.

Most of the used variables can be classified in four categories. The first one contains the angles between different reconstructions or between the same reconstruction run on different Hits. The second category contains the variables which are reconstruction specific, this can be both the output of the reconstruction as well as a quality estimator. A set of efficient variables has been developed within the ICECUBE collaboration and is known under the name of **common variables**. Some of the variables belonging to this set have been used and they form the third category. Finally, some newly designed variables enter the last category.

The various variables that entered in the BDT are described in Table 4.4. The common variables set uses the HiveSplit selected Hits and for the variables that require a reconstructed track, MuEx4MPE was used. In the case of `avgQtotDom`, `trEmpLength` and `trHitSepLength`, only DOMs or Hits that belong to a specified cylinder are used. This cylinder is positioned along the track with a radius of 150 m. An overview of the variable distributions is presented in Appendix B.

Table 4.4: Variables used in the BDT with a brief description and their importance in the BDT.

Variable	Brief description	Importance in BDT
Angle between reconstructions		
LineFit_GeoSplit	Angle between the two LineFit reconstructions applied on GeoSplit Hits	4.87×10^{-2}
MPEFit_GeoSplit	Angle between the two MPEFit reconstructions applied on GeoSplit Hits	5×10^{-2}
MuEx_MPE	Angle between MuEx4MPE performed on the HiveSplit cleaned Hits and MPEFit	3.9×10^{-2}
MuEx_LF	Angle between MuEx4MPE and LineFit both performed on the HiveSplit cleaned Hits	3.85×10^{-2}
DW_Lf4DW	Angle between Dwalk and LineFit4Dwalk	2.03×10^{-2}
Reconstruction specific variables		
MPEFit_Qual	MPEFit quality parameter (cf. Section 4.1.1)	5.88×10^{-2}
LineFit_HiveSplit_Qual	LineFit quality parameter (cf. Section 4.1.1)	4.64×10^{-2}
MuEx4MPE_HiveSplit_zen	Zenith angle obtained from MuEx4MPE	4.89×10^{-2}
MuEx_Sigma	Difference between two iterations of MuEx4MPE	4.08×10^{-2}
Common variables		
cogZ	Center of gravity of Hits along the vertical axis	5.74×10^{-2}
cogZSigma	Standard deviation of the cogZ distribution	5.3×10^{-2}
ZTravel	Average of the Z values of all DOMs minus the average of the Z values of the first DOM quartile	4.89×10^{-2}
avgQtotDom	Average DOM distance from the track weighted by the total charge of each DOM for DOMs that belong to the specified cylinder	6.07×10^{-2}
trEmpLength	Maximum length along the track without Hits for Hits that belong to the specified cylinder	6.66×10^{-2}
trHitSepLength	Distance along the track between the COG of the first quartile and the COG of the last quartile for Hits that belong to the specified cylinder	5.24×10^{-2}
New variables		
DWZtravel	ZTravel applied on Dwalk selected Hits	4.62×10^{-2}
QualDist	QualDist as described in Section 4.1.1	6.59×10^{-2}
avgDistCenterR	Average distance of the Hits from the center of the detector in the horizontal plane	5.54×10^{-2}
avgDistCenterZ	Average distance of the Hits from the center of the detector in the vertical axis	5.55×10^{-2}
avgDistTrack	Average distance of the HiveSplit Hits to the MuEx4MPE track	4.63×10^{-2}

4.2.2 BDT output

The result of the BDT is a score for each event between -1 and 1. The -1 score corresponds to pure background events and a score of 1 corresponds to pure signal events. The BDT output for signal, background, atmospheric neutrinos and background simulation (CORSIKA) is presented in Fig. 4.7. As for QualDist, one should verify that there is no over-training. This can be done by super-imposing a testing sample and a training sample as shown in Fig. 4.8 from which it is seen that no over-training occurred.

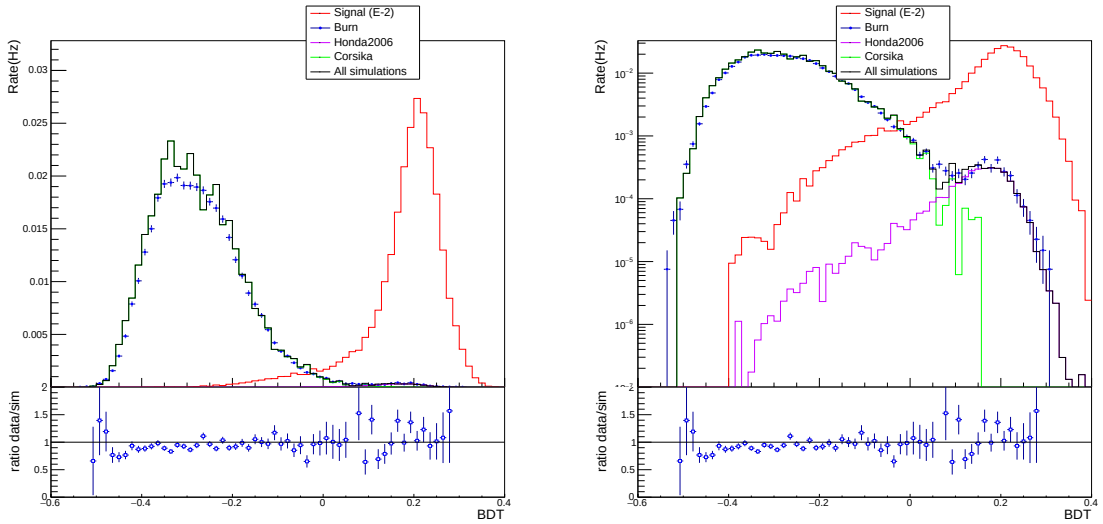

(a) (b)

Figure 4.7: BDT output in linear scale (a) and logarithmic scale (b). Signal is in red, background in blue, CORSIKA in green, atmospheric neutrinos (Honda model) in purple and the sum of CORSIKA and atmospheric neutrinos in black.

It is often useful to have an idea of the linear correlation between the variables used in the BDT, this is shown in Fig. 4.9. Many multivariate methods like neural networks for example are very sensitive to high correlations between variables. The BDT is a very stable algorithm that is not very sensitive to strong correlations. However, it is possible that the introduction of a variable that would be strongly correlated to another one would decrease the BDT performance. In this analysis, all correlated variables have been removed one by one and only those that had a positive effect on the BDT were kept.

Another interesting visualisation of the BDT output is the purity. The purity is defined as the rate of atmospheric neutrinos over the rate of background (burn sample). It is thus 0 if the background, due to mis-reconstructed down-going muons or noise, is several orders of magnitude larger than the amount of atmospheric neutrinos and it is equal to 1 if only atmospheric neutrinos remain in the background sample. The purity is shown in Fig. 4.10.

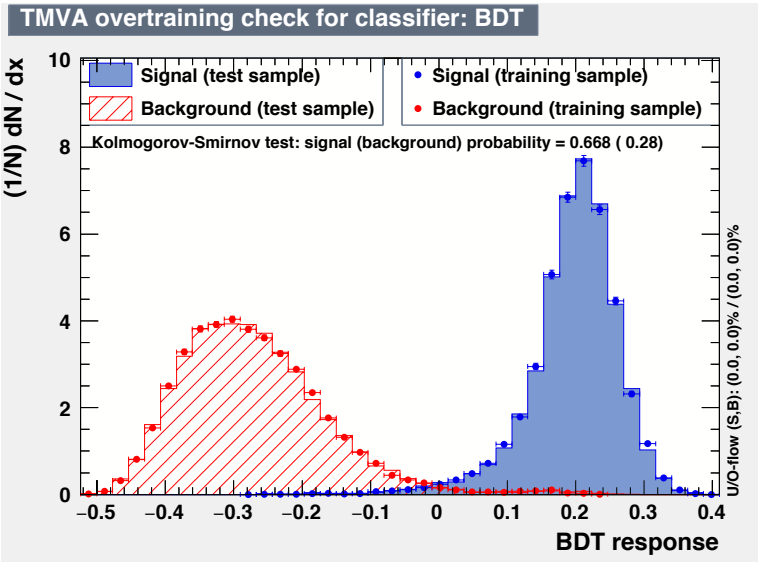

Figure 4.8: Over-training check automatically performed by the TMVA algorithm.

Table 4.5: Signal efficiency and background rate at a BDT cut of 0.07.

Well-reconstructed signal	All signal	Background
86.3%	72.6%	3.57 mHz

4.3 Results

The next step of the event selection is to define a cut value on the BDT score. However, this cut needs an optimisation that will depend on the chosen statistical method in order to maximise the sensitivity for discovery. The discussion and the selection of the statistical method is the subject of the next chapter where it will be explained that the optimal cut is at 0.07.

The signal efficiency after QualDist and after a BDT selection at this cut is shown in Fig. 4.11. The overall signal efficiency for well-reconstructed signal as well as for all signal events and the background rate for the BDT cut at 0.07 are presented in Table 4.5. As can be seen from Fig. 4.10, the purity at this BDT cut is above 80%. We have thus reduced the background to the irreducible atmospheric neutrino level while retaining more than 86% of the well-reconstructed signal events.

Several quantities can be calculated to measure the overall performance of the event selection. One of these quantities is the effective area which is defined as

$$A_{\text{eff}} = \frac{\text{observed event rate}}{\text{incoming flux}}. \tag{4.7}$$

It is calculated using signal simulation and relates the efficiency of the performed cuts with the sensitivity to a specific signal flux. The higher the effective area, the higher is the amount

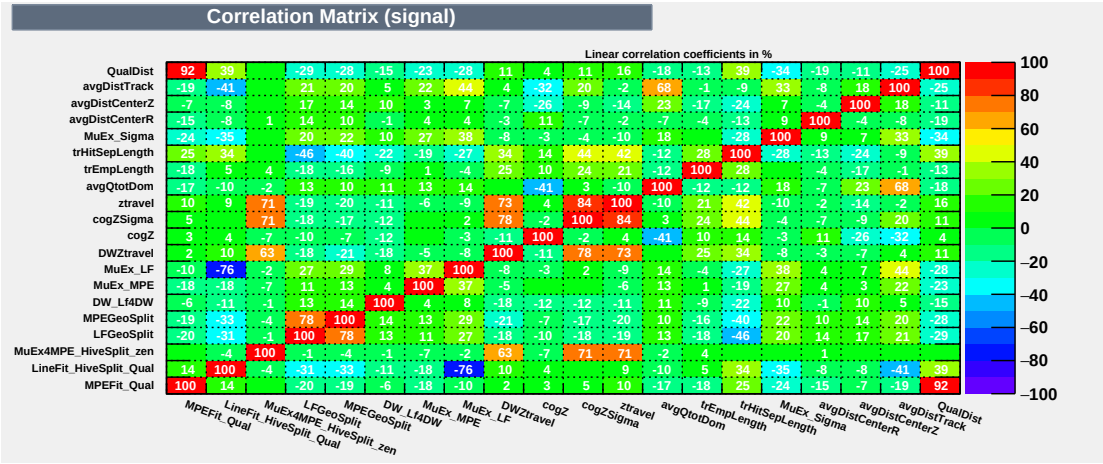

(a) Signal

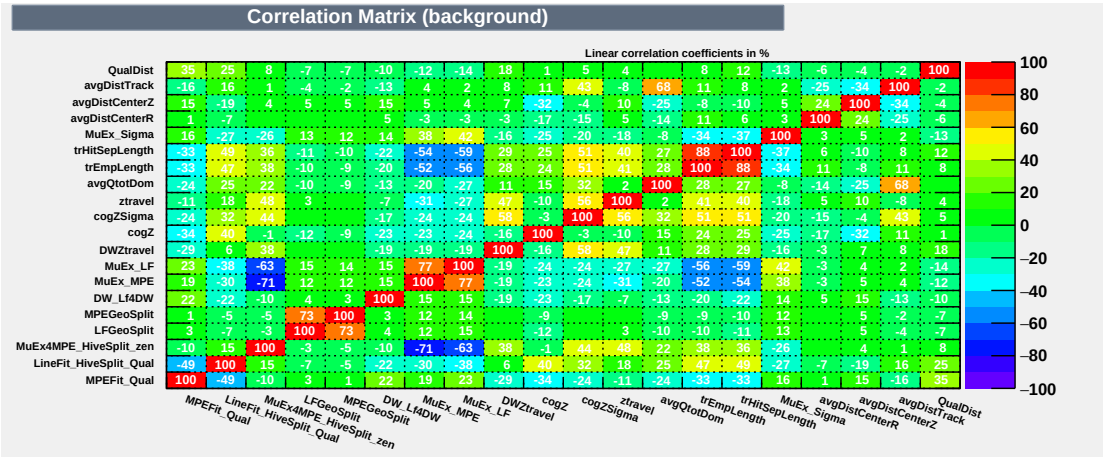

(b) Background

Figure 4.9: Linear correlation between BDT variables for signal (a) and background (b).

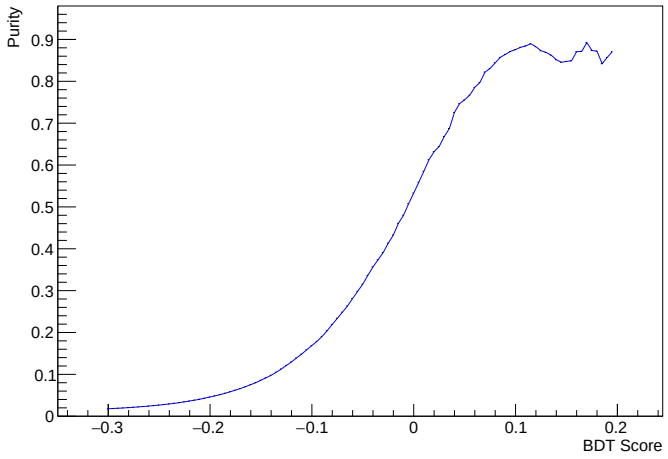

Figure 4.10: Purity of the atmospheric neutrinos with respect to the burn sample as a function of the BDT score. The variations above the BDT score of 0.1 are due to lack of statistics in the burn sample since most of the events are cut away.

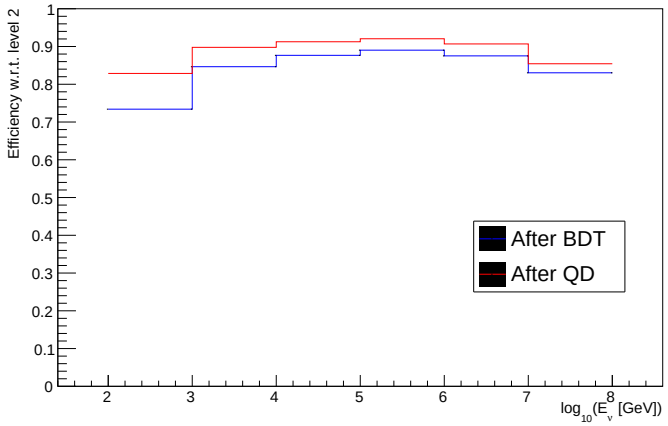

Figure 4.11: Signal efficiencies with respect to Level2 for well-reconstructed events.

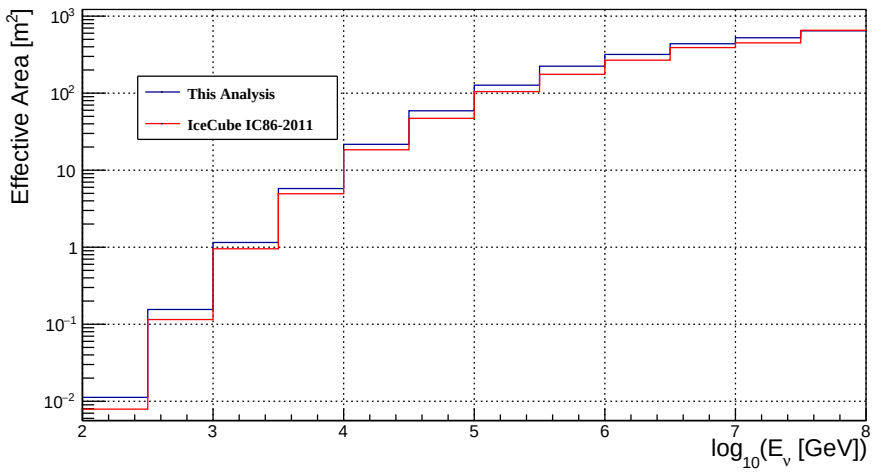

Figure 4.12: Effective area as defined in the text. This analysis is in blue, the previous track Northern Hemisphere GRB analysis is in red [84]. The effective area obtained in the current analysis is a factor 1.2 higher than the one of the previous analysis.

of signal kept. The effective area can be visualised in Fig. 4.12 where it is compared to the one of the previous IC86 Northern Hemisphere track search from GRBs [84]. Based on the effective area, the event selection performed in this analysis seems to keep more signal than the previous analysis and consequently should be more sensitive. The obtained effective area is about a factor 1.2 higher than the one of the previous GRB analysis.

However, one should always compare effective areas in combination with the median angular resolution. This comes from the fact that it is important to have more signal but it is not useful if the increase in the signal efficiency is due to mis-reconstructed signal events. Such events that will have a poor angular resolution will not contribute to the search for neutrinos from GRBs because they do not point precisely enough towards a GRB.

The median angular resolution of this analysis is 0.77° (see Fig. 4.13) while the angular resolution of the previous IC86 GRB analysis is 0.72°. The signal simulations used in the analyses are different because in the current analysis newer simulations were used which generate a higher amount of noise to better fit the recorded data. Taking this into account, the current analysis reflects an overall improvement in the event selection with respect to previous searches.

This improvement is due to several effects. The first one is the development of the preselection method QualDist. While previous analyses where using straight simple cuts as preselection, the QualDist method allows a more efficient signal-background separation.

Furthermore, the starting point of this analysis was the Level2 data where only filtering procedures have been applied. Previous searches started at a level called **OnlineL2** which starts from the MuonFilter and applies additional cuts in order to reduce the amount of events in order to run more evolved reconstructions directly at the South Pole. In the final sample

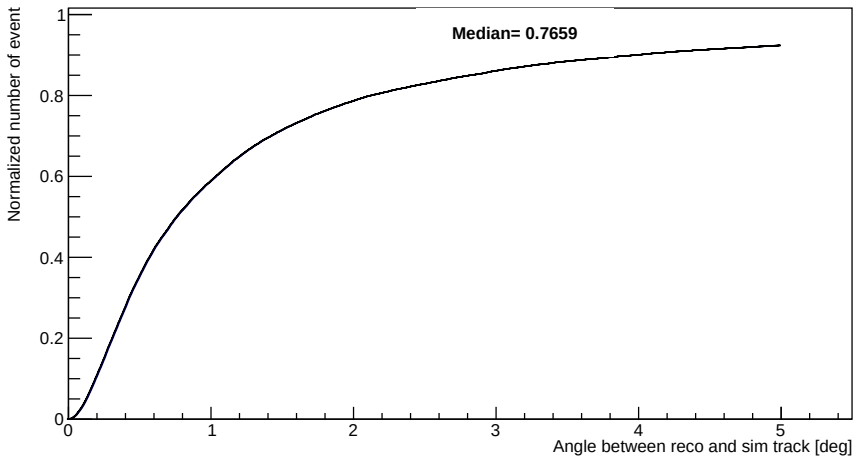

(a)

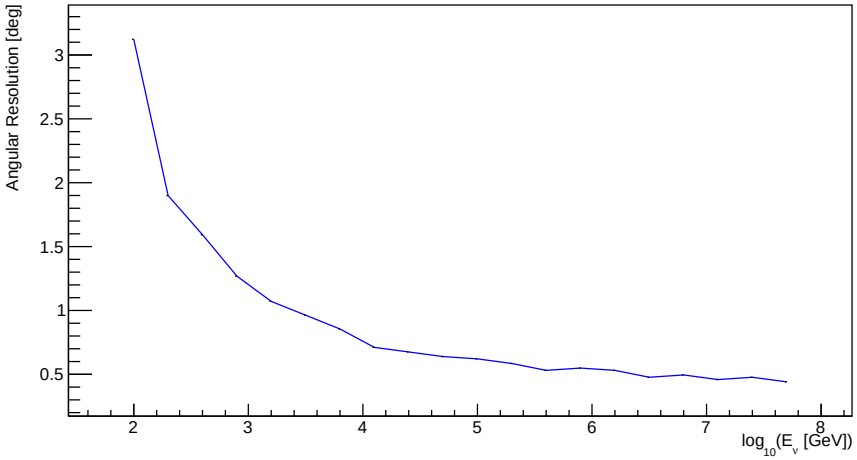

(b)

Figure 4.13: Cumulative angular resolution in (a) and median angular resolution as a function of energy in (b).

of the current analysis, 4.5% of events do not satisfy the OnlineL2 criteria and would have been discarded if the event selection had started at OnlineL2 instead of Level2. These 4.5% of events have an angular resolution of 1.43° and are thus interesting events for a point-source analysis.

The event selection performed in the current analysis is more efficient in retaining well-reconstructed signal events than previous analyses and it includes new events which were not considered in the previous IceCube analysis. This allows for a possible deviation from previously published results where no neutrino signal from GRBs was detected.

5

Statistical Methods

Once the selection of events is finalised, one needs to use a statistical method to assess the significance of the observations. This chapter is dedicated to the study of the most appropriate statistical method for the search of neutrinos from long GRBs. In order to compare different statistical methods, a toy-model has been developed. This toy-model will be explained in the beginning of this chapter. This will be followed by a description of the various methods that have been implemented and compared. Finally, the results of the study will be presented as well as the optimisation of the BDT score cut value.

5.1 Toy-Model

5.1.1 General concept

In order to allow a fair comparison between the different statistical methods, the toy-model needs to be as realistic as possible. Even though the purpose of the toy-model is to draw conclusions about the specific case of the search for neutrinos from long GRBs, we have created a tool that is generic enough such that it can be applied to other analyses that would search for neutrinos coming from short GRBs or any other subset of GRBs.

Following the requirements above, the toy-model has been implemented to work with only a few key parameters. These parameters are the expected background rate, the angular and time windows that are considered and the median angular resolution of the event selection ($\widetilde{\psi} = 0.77^{\circ}$). In addition to these parameters, the user must also provide a list of observations about GRBs. In the case of the analysis presented in this thesis, a list of long GRB

parameters, as obtained from the GCN notices of the various satellite observations, has been used. These GRB parameters include the angular position uncertainty σ_{GRB}, the T_{90} duration and the redshift.

This list of GRBs was obtained from an ICECUBE tool called GRBweb[1] which compiles information from various satellites dedicated to GRB observations as mentioned in Section 1.1. The field of view of these satellites goes from 1.4 sr (SWIFT) to almost 4π sr (Fermi GBM). Using GRBweb, it is possible to select GRBs that were detected during specific ICECUBE configurations as well as during successful runs (i.e. times without detector failure). The selection of long GRBs in the Northern Hemisphere during four years of IC86 operation gives 468 GRBs. A full overview of these 468 long GRBs and their parameters as used in the current analysis is presented in Appendix A.

Once these parameters are entered, the user can vary the number of injected signal events in order to obtain the sensitivity of the methods. The angular and time windows can be optimised and the angular resolution is given from the event selection. The difficult parameter is the expected background rate. In order to know the final background rate, one must perform an optimisation on the BDT score which depends on the statistical method used. It is then necessary to use an estimation of the background rate when searching for the optimal statistical method. It was decided to consider a background rate of 3 mHz, corresponding to the atmospheric neutrino background rate, for all the statistical method investigations (the previous IC86 GRB analysis had a final background rate of 3.8 mHz).

In high-energy particle physics, it is common to express the significance of an observation through the p-value. In the context of hypothesis testing, if the background-only hypothesis is H_0 , the p-value is the probability that the observed data support H_0. The lower the p-value, the lower is the probability that the data are compatible with the background-only hypothesis. This background-only hypothesis can be represented by different distributions depending of the statistical method used as explained in Section 5.2. By convention, a discovery is claimed if the p-value is lower than 2.9×10^{-7} which represents a 5σ (single-sided) Gaussian deviation from the mean value.

In the toy-model, the comparison of several statistical methods is achieved by comparing their average p-value. The p-value is obtained in two steps. First, one computes the test statistic T_{data} of a specific method on the data. In this chapter "data" will stand for the sum of background plus signal events. In the toy-model, the data are composed of simulated background and injected signal events. Once T_{data} is known, one needs to compute the test statistic T_{bkg} value on a large number of background-only simulations. The p-value is then obtained by counting how often $T_{\mathrm{bkg}} \geq T_{\mathrm{data}}$ and by dividing by the number of background-only simulations performed. In other words, the p-value is the answer to the question in which fraction of the cases the test statistic value of the data can be found or can be overtaken in the case of a pure background hypothesis.

In order to save computing time, a data set (background plus signal) is generated and all

[1] GRBweb is accessible from `http://grbweb.icecube.wisc.edu` .

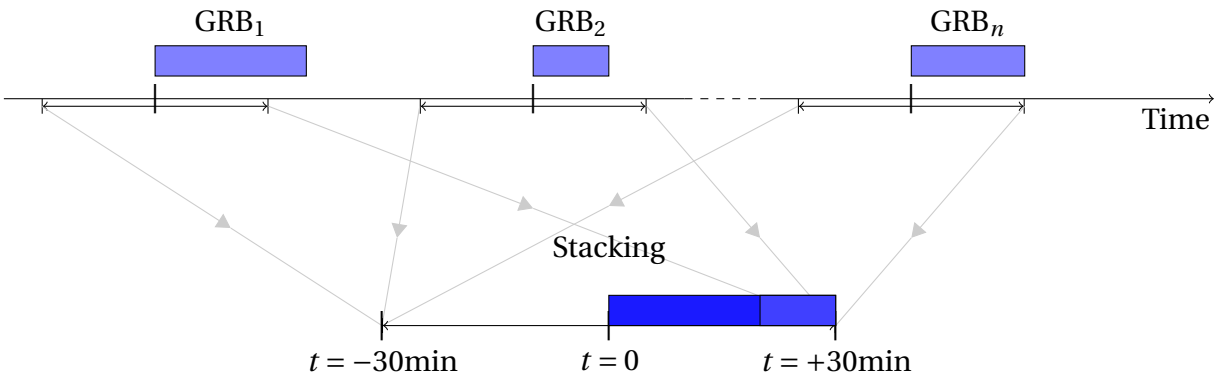

Figure 5.1: The stacking procedure. The GRB time windows are stacked in the way that all their trigger times are set in the middle of the time window (at $t = 0$).

the methods that are compared return their T_{data} from that same sample. Then, background-only simulations are performed such that at each simulation the various T_{bkg} of the different methods are computed and compared to their respective T_{data}. The procedure is then repeated with other data sets and the average of the obtained p-values is used to compare the methods.

5.1.2 The stacking procedure

The current analysis will search for a possible neutrino signal from long GRBs. However, since the expected amount of neutrinos per GRB is lower than 1 [84], one needs to stack the events of the four years GRB sample in order to obtain a possible detectable signal. This stacking procedure starts by selecting time windows centered at the GRB trigger times as sketched in Fig. 5.1. All the events belonging to these time windows are then stacked by considering their time difference between the event times and their associated GRB trigger time. In this way, all the trigger times happen at the time $t = 0$, the events detected before the GRB trigger time have a negative t and the events detected after the GRB trigger time have a positive t.

This method implies that in the case a GRB has a duration longer than half the time window, the events detected outside the time window will not be considered. Since the GRBs have different durations, the events detected during the afterglow emission from a shorter GRB will be stacked with the events detected during the prompt emission of a longer GRB. This effect makes it impossible to define a specific afterglow time. On the contrary, the identification of the events that are detected before the GRB (precursor events) is trivial since it corresponds to all events with a negative t.

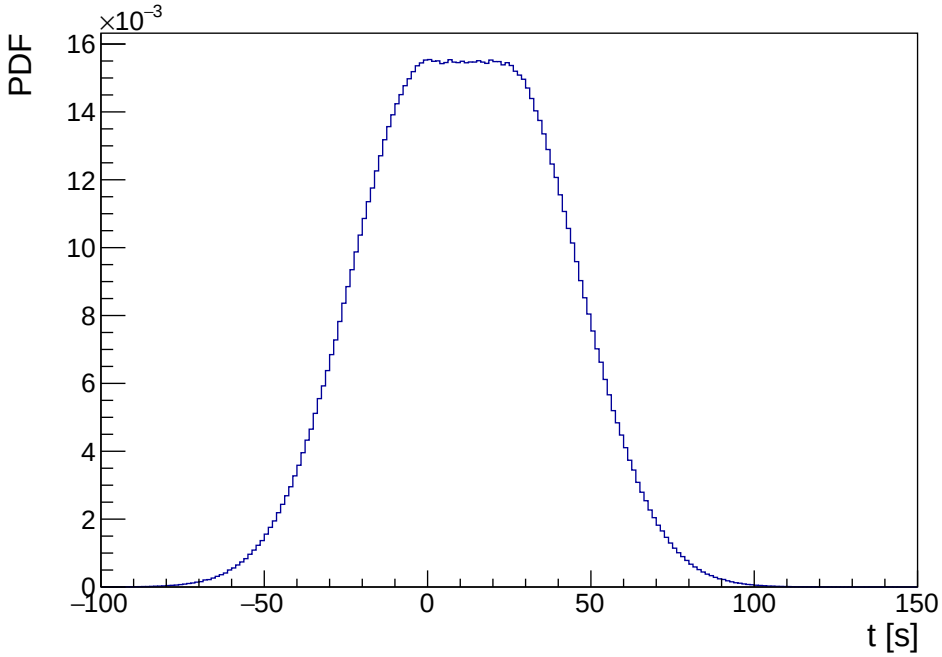

Figure 5.2: Example of a time distribution for prompt signal events.

5.1.3 Event generation

In the toy-model, an event is the set of two observables. The first one is the time between a GRB trigger and the considered event and the second one is the angle between the reconstructed event and a GRB location. In the case of background, the toy-model starts by simulating events isotropically for every considered GRB according to the specified rate and the angles between events and the GRB are computed. For the events that fulfill a maximum angle criterion, a time is drawn from an uniform distribution according to the considered time window and it is associated to the event.

In the case of signal events, the angular distance between an event and a GRB is randomly generated from a Gaussian with a standard deviation σ that depends on the angular resolution $\widetilde{\psi}$ of the event selection and the position uncertainty of the associated GRB σ_{GRB} such that $\sigma = \sqrt{\widetilde{\psi}^2 + \sigma_{\mathrm{GRB}}^2}$.

The time information of the prompt signal events is generated from a distribution which is flat during T_{90} and has Gaussian tails on each side. Fig. 5.2 shows an example of such a distribution. The Gaussian tails avoid a too sharp distribution and are computed with a standard deviation equal to T_{90}.

The aim of the toy-model and of the analysis in general is to find a method that would be sensitive to all GRB phases of possible neutrino production which are precursor, prompt and afterglow. It is then necessary to generate signal events other than prompt events to test the various methods. As explained above, due to the stacking procedure, the case of afterglow is

more difficult to define. Since the precursor events correspond to all events with a negative t, it is a clear distinct signal from the prompt events. Thus, the possibility to generate precursor events was implemented in the toy-model.

However, when simulating precursor events, the problem of which physical model to use arises. There is unfortunately no consensus on when the precursors are expected. However, several theorists seem to agree on the general time-scale of 10 to 100 s prior to the GRBs [47, 85, 86]. We decided to consider in the toy-model the best case scenario where all neutrinos are emitted at a fixed time prior to the GRB trigger time at the source. If a method fails to detect the most obvious precursor signal, then one can conclude that the method is not sensitive to precursors. Following this idea, precursor events are simulated exactly two minutes before the GRB trigger time at the source for all GRBs. The simulated time of detection of these precursor events varies with the redshift z such that a precursor event is effectively generated at a time $t = -120 \text{ s} \times (z+1)$.

In the full four years long GRB sample considered in this analysis, 19% of the bursts have a known redshift. In order to generate a redshift in the toy-model for the remaining 81% of GRBs, the distribution of the observed redshift by the SWIFT satellite was used. The unknown redshifts were then randomly drawn from this distribution of 261 observed[2] redshifts. Since GRBs that are closer are easier to detect, the redshift distribution of observed GRBs is biased towards lower values. However, the same bias applies to the list of GRBs used in the current analysis. Since redshift values are selected from the SWIFT distribution in order to fill the missing redshifts in the list of observed GRBs, it is expected that these randomly selected redshifts correctly represent the distribution of observed GRBs. The histogram used to generate unknown redshifts is presented in Fig. 5.3.

5.2 Description of the statistical methods

A total of seven methods have been implemented and compared through the toy-model. For all these methods, several parameters needed an optimisation. The first parameter to optimise is the size of the angular window centered at the GRBs position within which events will be selected and will thus contribute to the test statistic calculation.

During this first phase, already several methods appeared clearly less significant than others. As such, a first selection was made after which more specific tests and optimisations were performed on the remaining methods. The seven methods will be presented in the following and we will give a more detailed description of the most sensitive methods that have passed the first selection. Some methods are designed for the search of a clustering of signal in the arrival times of events, others focus on the angular distances between the GRBs and the events and some try to combine these two aspects in a single test statistic.

In order to write in a mathematical format the various test statistics, it is useful to define

[2] This distribution is built from GRB observations over more than the 4 years considered in the current analysis.

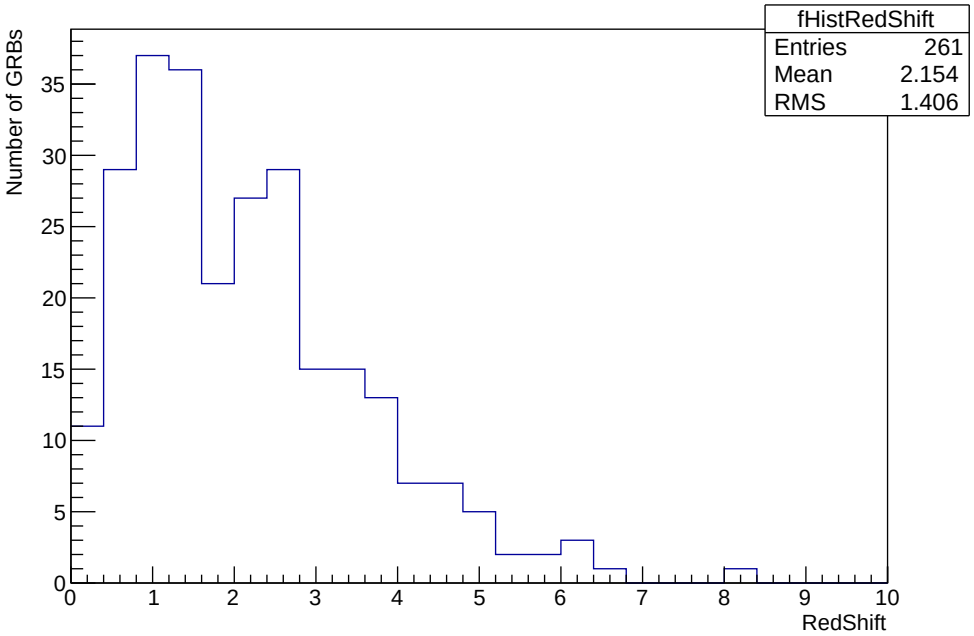

Figure 5.3: Distribution of observed redshifts by the SWIFT satellite. This distribution is used to randomly generate redshifts for GRBs for which it could not be measured.

some notations. In the remaining of the chapter, the angle between an event i and the corresponding GRB is α_i and the size of the angular window around GRBs is $\alpha_{\max}$. Similarly, the time of an event i is t_i and the time window around the GRB trigger times is $t_{\max}$. Since the GRB trigger times are placed at $t = 0$ in the stacking procedure, the events are selected between $-\frac{t_{\max}}{2}$ and $\frac{t_{\max}}{2}$.

Another useful notation is the average number of background events $\langle n_b \rangle$. This number depends on the background rate chosen as well as on the sizes of the time and angular windows. Other notations which are more method specific will be defined later.

5.2.1 Over-Density Search

The Over-Density Search (ODS) is a simple method that compares the event time differences observed in data (signal plus background) with the expected time difference for background-only events. This method uses the intuitive assumption that, since the background events are uniformly distributed in time, one expects a constant time difference between them. This assumption is actually not correct because the time differences between Poisson distributed events follow an Erlang distribution, which in the case of consecutive events reduces to an exponential. Despite this erroneous assumption, the method gives interesting results in the search for an over-density of events.

If one defines

$$S_i = \frac{t_{\max}}{\langle n_b \rangle} - (t_{i+1} - t_i)\,, \tag{5.1}$$

then the test statistic T is defined as

$$T = \sum_{i=1}^{n-1} S_i\,, \tag{5.2}$$

where only positive S_i are considered in the sum.

5.2.2 2D Scan method

This method uses an Anderson-Titterington algorithm (algorithm 14.3.5 of [87]). This algorithm searches for clusters in two dimensions by constructing circles at several grid points and by computing a likelihood ratio for each circle. Since the size of the cluster is unknown, the size of the circle varies such that it contains an increasing number of events at each iteration.

The algorithm can be applied to the current analysis by constructing the two dimensional space composed of event times t_i and angular distances to GRBs α_i. For simplicity the time window is rescaled to the angular window by multiplying the times t_i by $\frac{\alpha_{\max}}{t_{\max}}$. In this way, the two dimensional space is a square and instead of constructing circles at each grid point, squares are constructed, containing at the first step one event and then growing to contain more and more events.

The returned test statistic value is the maximum likelihood ratio encountered while varying the size and the location of the squares.

5.2.3 Ψ method

The Ψ method starts by creating a histogram with the event times. This histogram is then compared to the expected time distribution of background events. Since background is expected to be homogeneously distributed in time, the histogram is compared to a flat distribution. The comparison is performed by calculating the probability for an event to fall in the bin k based on the considered distribution. In our case, if there are n events and m bins, the probability of the bin k is $p_k = \frac{1}{m}$ (details about the Ψ method can be found in [88]).

Once the p_k are defined, the method uses an expression based on a multinomial distribution for the Ψ test statistic

$$\Psi = -10 \left[\log_{10} n! + \sum_{k=1}^{m} \left(n_k \log_{10} p_k - \log_{10} n_k! \right) \right], \tag{5.3}$$

with n_k the number of events in the bin k. The details of the derivation of this expression can be found in [88].

An important aspect of the Ψ method is that it is sensitive to the difference in the distribution shapes between data and background expectation and not to the difference between the observed number of events and the expected number of background events.

An adaptation of the Ψ method based on the angles α_i instead of the times t_i has been developed by our team in Brussels to search for neutrinos from Active Galactic Nuclei. The details of this work can be found in [89]. This adaptation allows for more stability in the p-value calculation with respect to the bin size. However, this improvement of stability has the cost of an extended computation time and cannot be applied to flat distributions.

The solution to increase the stability of the method proposed in [89] consists of an increase in the number of bins until at most one event per bin is obtained. In this ideal case, all histograms are flat. Eq. (5.3) then reduces to

$$\Psi = -10 \left[\log_{10} n! + \sum_{k=1}^{m} \left(n_k \log_{10} p_k \right) \right] \tag{5.4}$$

and only the p_k have an influence on the test statistic. In the case of a non-constant distribution of the expected background, the p_k are all different and they act like a weight for each event. This allows the method to remain sensitive.

However, in the case of a flat distribution, the p_k are all the same and our refined approach loses its sensitivity. It was thus decided that in the toy-model, the Ψ method will follow the description made in [88].

5.2.4 Auto-Correlation method

The purpose of the Auto-Correlation method (A-C) is to search for a deviation from the background event time distribution. For this, the method starts by generating a distribution with the time differences between all possible event pairs. The distribution is then binned and the number of pairs per bin is compared to a background-only simulation in order to extract the probability of having a certain number of pairs in a specific bin.

Technically, the method has been implemented in two steps. The first step generates background-only events and stores the time differences between all the possible event pairs in a histogram. The histogram is then used to compute the probability of having a number of pairs larger than or equal to a value n_p in a certain bin k.

In the second step, the data composed of background and signal follow the same procedure in order to have a histogram containing all pairs. One then associates in this new histogram to each bin a probability calculated at the first step in function of the bin contents. Once the probabilities of all bins are known, the logarithm of the lowest one is reported as the test statistic. This lowest probability actually corresponds to a pre-trial p-value. In details, if p_k is the probability associated to the bin k, the test statistic T is

$$T = -\log_{10} \left(\min_{k=1..n} p_k \right). \tag{5.5}$$

In order to obtain the post-trial p-value, one follows the same scheme as for the other methods. Once the test statistic is known for data, the procedure is repeated on a large number of background-only simulations and the value of the data test statistic is compared to those obtained under the pure background hypothesis.

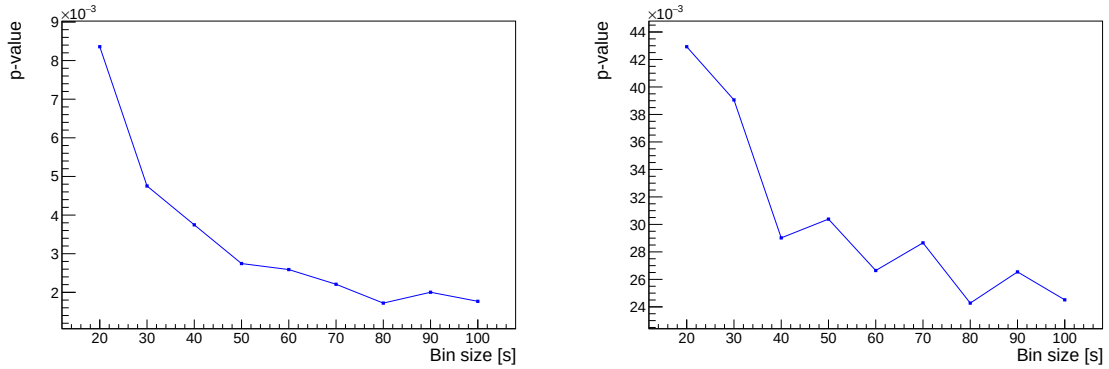

(a) $t_{max} = 1$ hour. (b) $t_{max} = 2$ hours.

Figure 5.4: Result of the bin optimisation for the A-C method. The value of 80 s seems to be the optimal bin size.

Since the sensitivity of the method depends on the binning choice, an optimisation has been performed in order to select the most appropriate binning. Since not all parameters can be optimised in one step, some parameters had to be fixed in order to search for the most appropriate binning as explained below.

As mentioned above, all the toy-model simulations were performed at a background rate of 3 mHz; the angular window α_{max} was set to 3° which is the result of the first optimisation performed on all methods and will be explained later in this section. Concerning the angular resolution, the value 0.77° was used.

The number of injected signal events was set to 10 which represents $\approx 0.02 \times 468$ GRBs reflecting a situation in which only 2% of all GRBs provide a detectable signal. The decision of using 10 signal events was not motivated by theoretical arguments but by empirical arguments. Indeed, since the purpose of the optimisation is to find the appropriate binning, it is more interesting to compare different bin sizes in a situation where there are enough signal events to have variations in the p-value as a function of the bin size. However, one should not increase too much the number of signal events in order to remain in a realistic situation. A number of signal events set to 10 allows a bin size comparison in the case of a signal detection while remaining a realistic number of expected signal events.

In addition to the parameters mentioned above, one needs also to specify a time window t_{max}. In order to limit the amount of calculations, only two t_{max} values have been considered. They are 1 hour and 2 hours around the GRB trigger times. The results of the bin optimisations for these two time windows are presented in Fig. 5.4.

From Fig. 5.4, the size of 80 s for the bin seems optimal. This value will be used in the following. The variations that can be seen in Fig. 5.4 are due to the limited number of data generations, because of the needed CPU time, after which the average of the obtained p-values is computed.

5.2.5 Likelihood method

This method is the one used in previous ICECUBE IC86 GRB analyses. It is a method designed for the search of prompt neutrinos and, as it will be shown, it is not sensitive to precursor or afterglow neutrinos. The details about the development of this method can be found in [82].

In order to determine the test statistic one first has to construct the expected background PDF for the angular part B_α and for the time part B_t. Since the background is isotropic in space and is uniform in time, one has

$$B_\alpha = \frac{\sin\alpha}{1-\cos\alpha_{\max}} \tag{5.6}$$

$$B_t = \frac{1}{t_{\max}}. \tag{5.7}$$

Similarly for the signal, one should define S_α and S_t. Since in the case of a toy-model we know what PDF was used to generate the signal events, it is straightforward to define the Likelihood signal PDF. However, once the statistical method is applied on real data, the source PDF is unknown. A strong difference between the expected source PDF and the assumed one in the toy-model could have an important effect on the efficiency of the method. The dependency of the efficiency of the method with respect to the simulated source PDF in the toy model could also be relevant in other methods which do not assume a particular source PDF.

As explained in Section 5.1.3, the angular source PDF is a Gaussian and the prompt time PDF is flat during T_{90} and has Gaussian tails. There is, however, a difference between the time PDF used to generate signal events and S_t. In the case of S_t, the PDF is truncated at $t = -3T_{90}$ and at $t = 4T_{90}$. One truncates the PDF to avoid a too high background contamination. Since this prompt time PDF was used in previous analyses, this is the one that will be used for the Likelihood method in the current analysis as well. The signal PDF S and the background PDF B are shown on Fig. 5.5.

In more detail,

$$S_\alpha(\alpha) = \frac{1}{\sigma\sqrt{2\pi}} e^{-\frac{1}{2}\frac{\alpha^2}{\sigma^2}} \quad \text{where} \quad \sigma = \sqrt{\tilde{\psi}^2 + \sigma^2_{\text{GRB}}} \tag{5.8}$$

$$S_t(t) = \begin{cases} \frac{1}{T_{90}(1+\sqrt{2\pi})} e^{\frac{-t^2}{2T_{90}^2}} & \text{if} \quad t \in [-3T_{90}, 0] \\ \frac{1}{T_{90}(1+\sqrt{2\pi})} & \text{if} \quad t \in [0, T_{90}] \\ \frac{1}{T_{90}(1+\sqrt{2\pi})} e^{\frac{-(t-T_{90})^2}{2T_{90}^2}} & \text{if} \quad t \in [T_{90}, 4T_{90}] \\ 0 & \text{if} \quad t < -3T_{90} \text{ or } t > 4T_{90}. \end{cases} \tag{5.9}$$

Using the signal PDF $S = S_\alpha \times S_t$ and the background PDF $B = B_\alpha \times B_t$, the Likelihood test statistic T can be defined as

$$T = \sup_{n_s} \left[-n_s + \sum \ln\left(\frac{n_s S}{\langle n_b \rangle B} + 1 \right) \right], \tag{5.10}$$

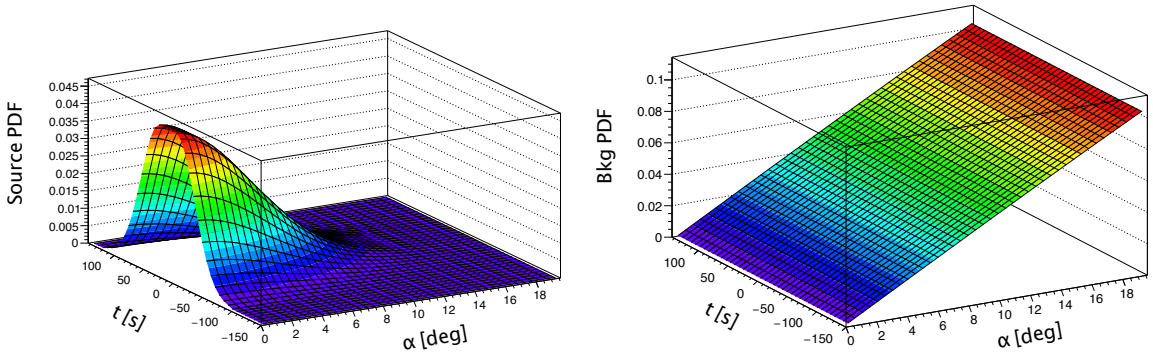

(a) S (b) B

Figure 5.5: Signal (a) and Background (b) PDF as used in the Likelihood method.

where n_s is the number of source neutrinos.

Instead of using the combined time and angular information in the Likelihood PDFs, one could also use only S_t or S_α. The use of S_t only is not interesting because in that case the method basically reduces to a Cut and Count method. The case where the Likelihood is used only on the angular information is more interesting because it allows the method to be sensitive to a neutrino emission from the three GRB phases. In the following, the name Likelihoodα will be used for the Likelihood method that only uses the angular PDFs. When the method uses time and angular information, the name simply remains Likelihood.

5.2.6 The PLT method

The name PLT is actually composed from the first character of the three author names of [90]. It is a method designed to be sensitive to small perturbations of the expected background by a possible signal. The signal is thus treated as a perturbation of the expected background. Following [90] and using, as above, $B(x)$ as the background PDF and $S(x)$ as the signal PDF, one can define the following PDF

$$p(x|\eta,\theta) = (1-\eta)B(x) + \eta S(x|\theta)\,, \tag{5.11}$$

where η represents the strength of the perturbation and θ the location of the perturbation. For example, if we consider the times t_i, one should replace the x of the previous equation by the t_i and θ will be the time at which the signal is present. One can also consider a multi-dimensional space like for the 2D Scan method. In that case, θ becomes a vector.

According to [90] and by following the example of the search for a signal in time, one can

then define a "score process"[3]

$$\mathscr{S}(\theta) = \frac{\partial \log\left[\prod_{i=1}^{n} p(t_i|\eta,\theta)\right]}{\partial \eta}|_{\eta=0} \tag{5.12}$$

$$= \sum_{i=1}^{n} \frac{S(t_i|\theta) - B(t_i)}{B(t_i)} \tag{5.13}$$

in the case of a number n of events.

One can then construct the test statistic T by maximising $\mathscr{S}$ with respect to θ

$$T = \sup_{\theta} \mathscr{S}(\theta)\,. \tag{5.14}$$

The interest of the PLT method with respect to the Likelihood method is that it could be sensitive to the three phases and not only to the prompt one due to the maximisation with respect to θ which can be interpreted as a "scanning" in time for the search of the signal.

Unfortunately, the PLT method suffers from an important drawback. The function $\mathscr{S}$ can have an unstable behavior that makes it difficult to numerically find the maximum of the function. This effect is stronger in the case of PLT applied to the time information as can be seen from Fig. 5.6(b). Hence, the PLT method has been tested on only the angular information as well as on the combination of time and angle. In the case of a time and angle combination, the strong instability of the method applied on the time information is balanced by the more stable angular part. For comparison, the function $\mathscr{S}(\alpha)$ applied on the angles α_i is shown in Fig. 5.6(a).

When the PLT method is applied using both the times t_i and the angles α_i, the function $\mathscr{S}$ becomes two dimensional. The function $\mathscr{S}$ in such a case can be seen from Fig. 5.7 in the case of pure background and in the case of 10 injected signal events.

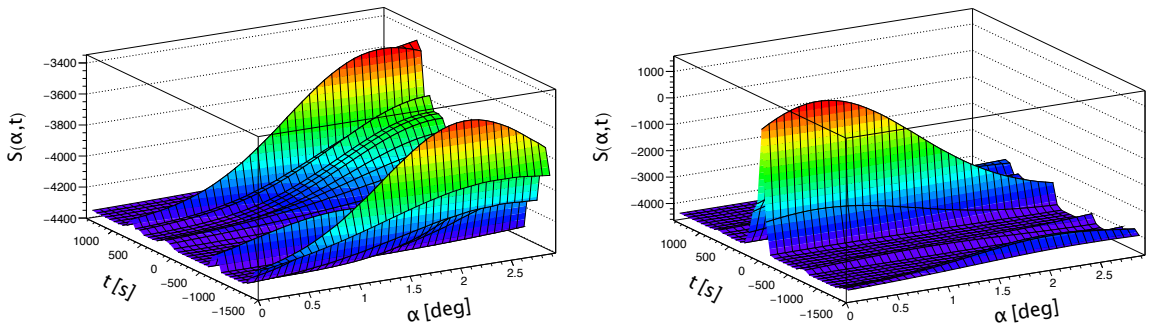

(a) Pure background. (b) 10 signal events injection.

Figure 5.7: The two dimensional function $\mathscr{S}(\theta)$ for pure background (left) and for an injection of 10 signal events (right).

[3] In [90], the score process is normalised. However, we did not use the normalisation because we are not interested in the intrinsic value of the test statistic but we only need a value to compare to background randomisations.

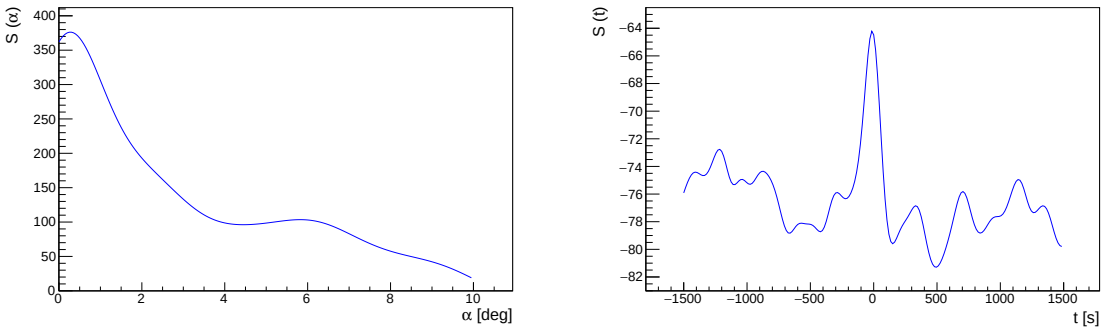

(a) $\mathscr{S}(\alpha)$. (b) $\mathscr{S}(t)$.

Figure 5.6: Function $\mathscr{S}(\theta)$ applied on the angular information ($\theta = \alpha$) on the left and on timing information ($\theta = t$) on the right. The various peaks make it difficult to numerically find the maximum. For this example, 10 signal events were injected.

As for the Likelihood method, PLTα will be used for the PLT method applied only on the angular part. The name PLT will stand for the two dimensional PLT that uses time and angular PDFs.

An attempt was made to replace the time signal PDF S_t by a Gaussian distribution in order to search for a generic increase in the stacked times of the events. The standard deviation of the Gaussian distribution was optimised in the same way as the bin size for A-C and it was found to be 60 s. The results using a Gaussian distribution or the PDF defined in the previous section for S_t were identical. This is a hint that the time information plays only a marginal role in PLT. In the following PLT will always be calculated with S_t being a Gaussian distribution.

5.2.7 Hybrid methods

A method is called hybrid if it is composed of a mix of two test statistics from the methods described above. As we will see in the next section, an interesting hybrid method is the one composed of a likelihood based test statistic (Likelihood or PLT) for the angular part and the A-C for the time part.

A comparison of the different hybrid methods will be shown in the Section 5.3. It is useful to introduce here the names given to these hybrid methods. The simplest way of combining two test statistics is to multiply them. This multiplication creates a new test statistic that can be used in the usual scheme. Two hybrid methods were created in this way, **Llh-AC** and **PLT-AC**.

Another possible combination is to keep both test statistics separated and to require in the p-value calculation that $T_{\text{bkg}} \geq T_{\text{data}}$ for the first method AND $T_{\text{bkg}} \geq T_{\text{data}}$ for the second method. This possibility has been implemented in a combination of Likelihoodα and A-C and is simply named **Hybrid**.

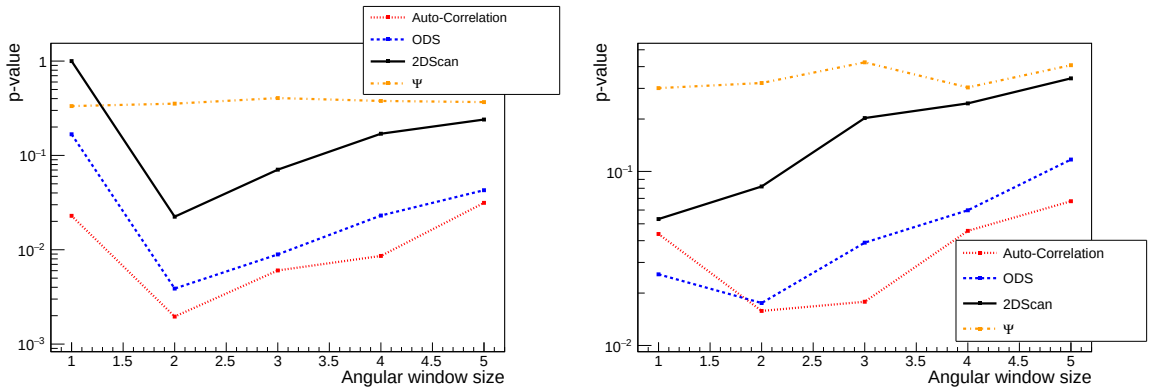

(a) $t_{\max} = 1$ hour (b) $t_{\max} = 2$ hours

Figure 5.8: Result of the angular window $\alpha_{\max}$ optimisation for a time window of 1 hour and 2 hours. Every method has an optimal size for the angular window (smallest p-value). The auto-correlation method clearly stands out. However, the A-C method loses sensitivity when extending the time window from 1 hour to 2 hours.

A third possible combination is to compute a p-value for each method and to multiply the two p-values afterwards. Such a multiplication has to take into account an extra trial factor of 2 because if one looks twice to the data, there is twice more chance to find a signal by chance. This is the last possibility that has been implemented and it is named **Likelihood*AC**.

5.3 Results of the toy-model

As explained in the previous section, the first step was to optimise the size of the angular windows $\alpha_{\max}$ for each method. The results of this optimisation can be seen in Fig. 5.8 and Fig. 5.9. The parameters are the following. The background rate is 3 mHz, the angular resolution $\widetilde{\psi}$ is 0.77° and the number of injected signal events is 10 (an explanation of this number has been given in Section 5.2.4). Since this calculation was performed before the bin size optimisation of A-C, the bin size has the default value of 60 s. The time window varies from 1 hour to 2 hours.

From Fig. 5.8 and Fig. 5.9, it clearly appears that the A-C method as well as the Likelihood and PLT methods are capable of reaching lower p-values than the other methods. Further investigations will thus only concern these methods. An important aspect of A-C can be seen in Fig. 5.8. The A-C method loses sensitivity when the time window increases. In order to keep a high sensitivity while still being sensitive to possible precursor events, the following comparisons will be performed for a 1 hour time window only.

The sizes that will be used for the angular windows per method are summarised in Table 5.1. In the case of A-C, though the minimum in Fig. 5.8 is at 2°, the value of 3° will be used.

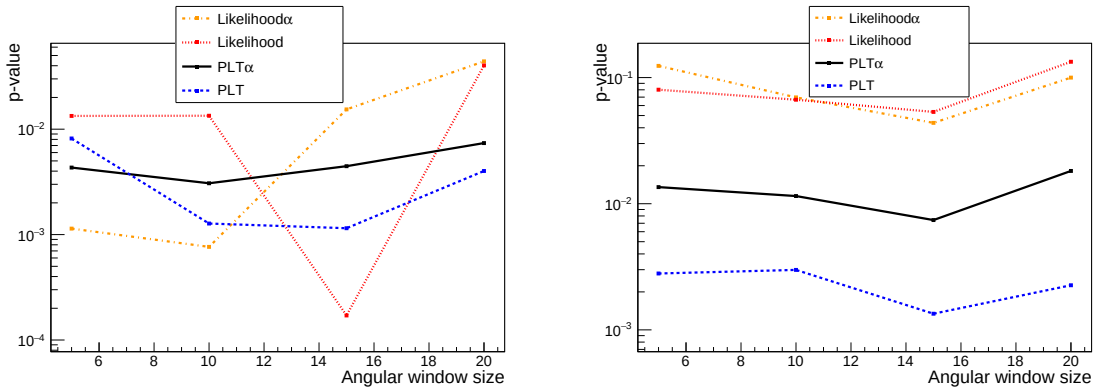

(a) $t_{\text{max}} = 1$ hour (b) $t_{\text{max}} = 2$ hours

Figure 5.9: Result of the angular window α_{max} optimisation for Likelihood and PLT for a time window of 1 hour and 2 hours. The two methods are considered both with only the angular PDF (Likelihoodα and PLTα) and with the two PDFs for time and angle.

Table 5.1: Size of the angular window α_{max}.

Likelihood	15°
PLT	15°
Likelihoodα	10°
PLTα	10°
Auto-Correlation	3°

The reason is that in the case of events that have a larger reconstruction angular uncertainty[4], the situation where too few events enter the 2° region to be able to use the A-C method might occur. This is due to the fact that for a time window of 1 hour and an angular window of 2°, the average number of background event is 2.9. When increasing to 3°, the average becomes 6.4. The value of 3° for the angular window is thus more conservative.

Since the A-C method only uses time information, it would be convenient to couple it with another method to take advantage of the information regarding the angular distribution of events. Such a combination forms a hybrid method, as explained in Section 5.2.7. The comparison between the different hybrid methods as well as the Likelihood and PLT methods has been performed by varying the number of injected signal events. Such a comparison allows to study the behavior of the various methods with respect to the signal strength. A comparison of the various hybrid methods is presented in Fig. 5.10. The behavior of the most interesting hybrid methods as well as the Likelihood and PLT methods is shown in Fig. 5.11.

In addition to the variation of the number of injected signal events, the statistical methods

[4]This concerns 50% of the events by definition of the median angular resolution.

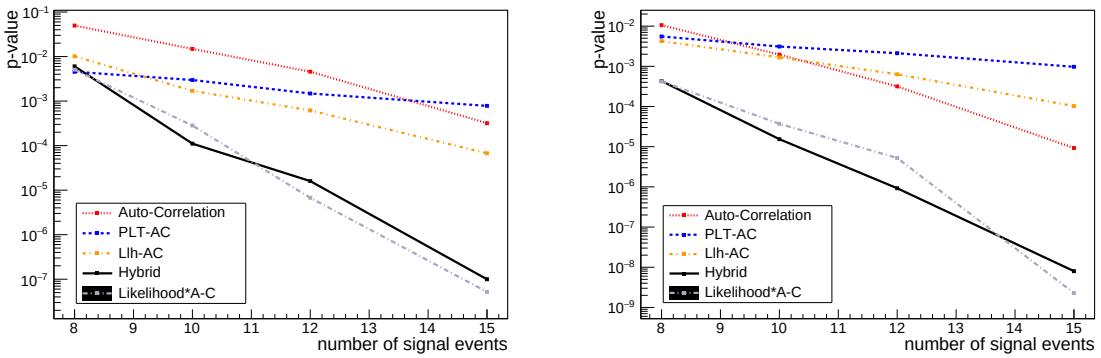

(a) precursor (b) prompt

Figure 5.10: Comparison of the various hybrid methods in the case of a prompt (right) and a precursor (left) signal. The Hybrid method seems to be the most efficient one for the search of neutrinos from long GRBs.

have been compared by generating a precursor signal as explained in Section 5.1.3.

The results of these comparisons favor the Hybrid method. This concludes the study of the statistical methods using the toy-model. The different parameters being the angular and time windows were optimised and the most sensitive method was chosen.

5.4 BDT cut optimisation

Following ICECUBE conventions, the appropriate BDT cut value is chosen based on three quantities. The two first ones are the 90% and the 50% **discovery potentials** (DP) and the third one is the so-called **sensitivity**. The discovery potentials are defined as the fluence required to have a probability of 90% or 50% to have a certain excess or a discovery. The sensitivity is defined as the fluence corresponding to the 90% confidence level upper-limit in the case where the test statistic is equal to the median value of the background-only test statistic distribution.

The sensitivity and discovery potential calculations are slightly different from the toy-model. The aim of the toy-model was to provide a generic framework to investigate different statistical methods. The sensitivity calculation is more specific to the details of the current analysis because it uses the declination distribution of the burn sample after the BDT selection as well as an event-per-event reconstruction uncertainty. Furthermore, the average number of background events $\langle n_b \rangle$ is directly obtained from the data by counting the number of events in an angular window of the same size as the one around the GRBs and located at the same declination but at the opposite right ascension.

The reconstruction uncertainty is calculated using the **Cramer-Rao** formalism [91, 92]. This tool allows to estimate a lower bound on the uncertainty of the reconstructed zenith σ_θ

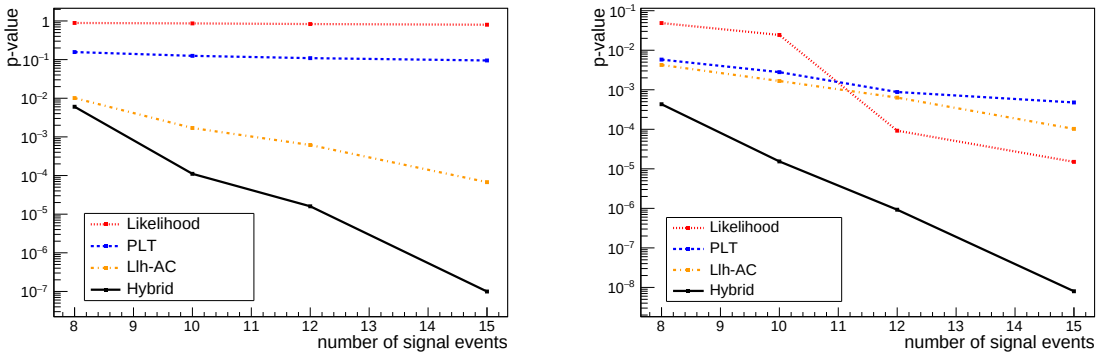

(a) precursor (b) prompt

Figure 5.11: Comparison of the most interesting methods selected from the angular window optimisation as well as the most sensitive hybrid methods in the case of a prompt (right) and a precursor (left) signal. The Hybrid method seems to be the most sensitive one for the search of neutrinos from long GRBs.

and azimuth σ_ϕ angle. The overall angular uncertainty σ of the reconstruction used for the current analysis is

$$\sigma = \frac{\sqrt{\sigma_\theta^2 + \sigma_\phi^2 \sin^2(\theta)}}{\sqrt{2}}. \tag{5.15}$$

Unfortunately, Cramer-Rao needs an energy dependent correction factor. This correction factor is obtained by fitting the ratio of the true angular error[5] over the Cramer-Rao error in function of the reconstructed energy as shown in Fig. 5.12(a). The ratio between the true angular error and Cramer-Rao after correction is presented in Fig. 5.12(b) where one can see that the Cramer-Rao σ is not energy dependent anymore.

Since the possible precursor or afterglow signal is completely unknown, the sensitivity and discovery potentials were calculated for a prompt signal injection only. The interest of generating precursors in the toy-model was to test the possible efficiency of the various methods to the most obvious precursor signal. From this study, it is clear that only the Hybrid and Llh-AC methods have a chance to detect precursor neutrinos. However, it is necessary to use the more reliable prompt signal injection when optimising the BDT cut value.

5.4.1 Pseudo-experiments

The usual procedure to calculate the sensitivity and discovery potentials is to compute a test statistic distribution using a background-only simulation and to extract from it the values

[5]Since this is done on simulation, the angle between the simulated neutrino and the reconstructed track is known.

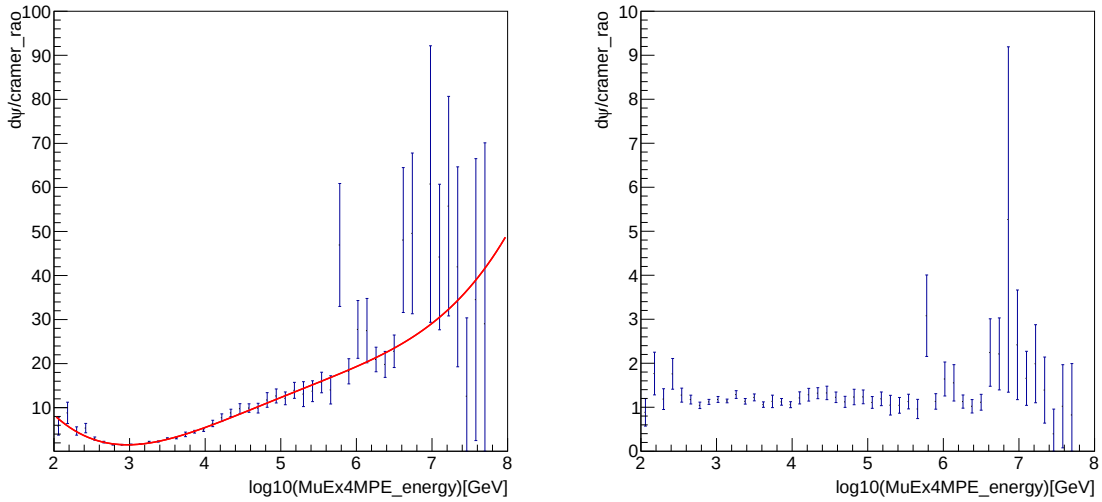

(a) Before correction

(b) After correction

Figure 5.12: Ratio of the simulated angular error over the Cramer-Rao σ. The red line on the left figure is a polynomial fit used to correct the energy dependence of the Cramer-Rao σ.

above which the probability of obtaining such a test statistic corresponds to a 3σ or 5σ Gaussian deviation from the mean value. By convention in IceCube, the σ are expressed for the case of a single-sided Gaussian. This means that 3σ corresponds to a probability of 1.35×10^{-3} and 5σ is 2.9×10^{-7}.

Once these values are computed, one uses the same background-only simulation and injects signal in it. This signal injection is performed by the determination of an injection value for each simulated event depending on the fluence and the proper simulation event weighting OneWeight (see Section 3.5).

In order to increase the number of NuGen simulated events that can be used and since the acceptance of the IceCube detector is only declination dependent, an entire declination band of a 1° size is used for the signal injection for a given GRB. This band is centered at the GRB position and covers declinations from $\delta_{\min}$ to $\delta_{\max}$. If the weight of a NuGen simulated event i is w_i, the spectrum fluence $\frac{dF}{dE}$ ($\equiv E^{-2}$ in this analysis) and n_{GRB} the total number of GRBs that enter the analysis, then the injection value V_i is

$$V_i = \frac{w_i \frac{dF}{dE}}{2\pi\left(\sin(\delta_{\max}) - \sin(\delta_{\min})\right) n_{\mathrm{GRB}}}. \tag{5.16}$$

Since OneWeight has the units [GeV$\cdot$cm$^2\cdot$sr] and the fluence $\frac{dF}{dE}$ has the units [GeV$^{-1}\cdot$cm^{-2}], the injection value V_i can be regarded as the average Poisson number of occurrence when computing the probability for an event to occur [82]. Furthermore, since $V_i << 1$ the probability for an event to occur more than once is negligible. Hence, the probability for the event

i to occur is [82]

$$p_i = \frac{V_i}{1!} e^{V_i} \approx V_i \,. \tag{5.17}$$

In practice, the value V_i is compared to a random number generated between 0 and 1 in order to decide whether the event i will be injected or not.

Once the signal injection is complete, the test statistic is calculated on the data composed of the background and the injected signal events. The calculation of the test statistic value on the data produced by such a signal injection is called a **pseudo-experiment**. The discovery potentials are then computed by searching, for several BDT cut values, the fluence that allows to have a test statistic which is larger than the 3σ or 5σ values in 90% or 50% of the pseudo-experiments. On the other hand, the sensitivity calculation is performed by searching the fluence for which the test statistic is larger than the median of the background test statistic distribution.

In order to allow a comparison to the method used in previous ICECUBE analyses, all the sensitivity and discovery potential calculations have been performed for the Likelihood method in addition to the Hybrid method. The Llh-AC method have also been used in the case of a strong difference between the results obtained in this section and those obtained by using the toy-model.

The background test statistic distributions for the Likelihood, Llh-AC and Hybrid methods are presented in Fig. 5.13, Fig. 5.14 and Fig. 5.15, respectively. In the case of the Hybrid method, the values of the two test statistics are presented as a 2D histogram since one has to compare the test statistic values for the angular Likelihood and the A-C separately. From this histogram, pairs of test statistic values are extracted such that the probability that the angular Likelihood test statistic is larger than the first value of the pair AND the value of the A-C test statistic is larger than the second value of the pair amounts to the required 3σ or 5σ. This is the straightforward two dimensional extension of the usual procedure.

5.4.2 Sensitivity and discovery potentials

The calculations of the sensitivity and discovery potentials following the above definitions are straightforward for the Likelihood and the Llh-AC methods. However, the Hybrid method needs more care because it combines two test statistics. If the test statistic applied to a pseudo experiment is $T_{\mathrm{PE,Llh}}$ for the Likelihoodα method and $T_{\mathrm{PE,AC}}$ for the auto-correlation method and the test statistics corresponding to a specific number of σ or to the median of the background test statistic distribution are T_{Llh} and T_{AC}, then the discovery potentials are calculated by searching for the fluence such that

$$T_{\mathrm{PE,Llh}} > T_{\mathrm{Llh}} \quad \text{AND} \quad T_{\mathrm{PE,AC}} > T_{\mathrm{AC}} \tag{5.18}$$

in 90% or 50% of the pseudo-experiments.

When calculating the sensitivity, the above equation cannot be used. This arises from the fact that the fluence required for the pseudo-experiment test statistics to be larger than both

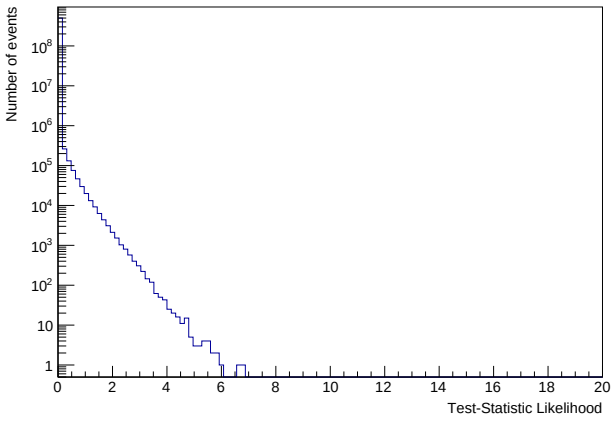

Figure 5.13: Likelihood test statistic distribution for background events (see Section 5.2.5 for details about the test statistic).

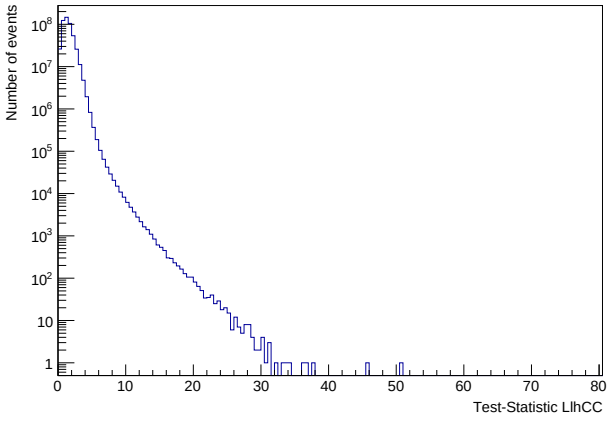

Figure 5.14: Llh-AC test statistic distribution for background events (see Section 5.2.7 for details about the test statistic).

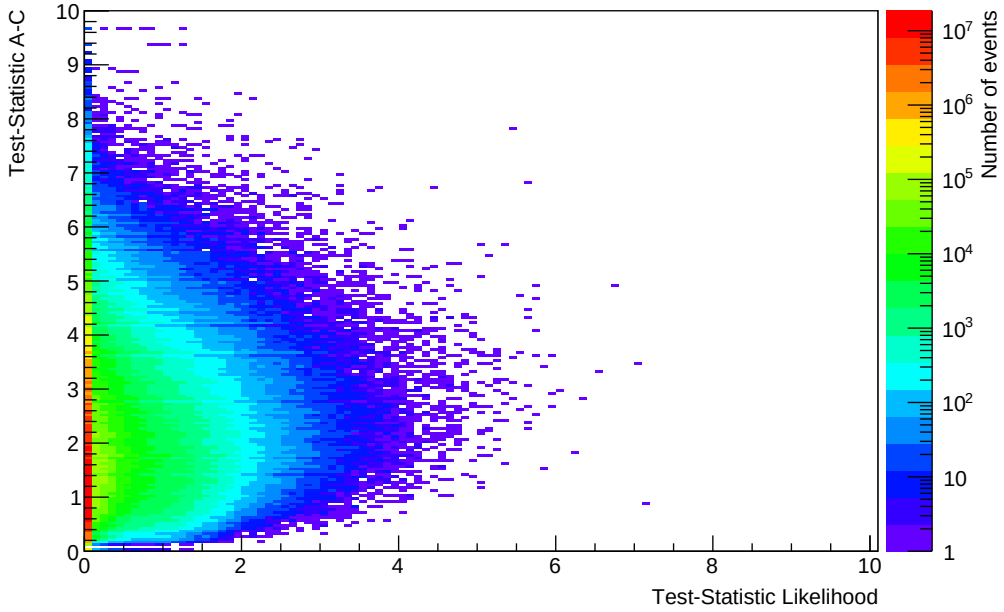

Figure 5.15: Hybrid test statistic distribution for background events (see Section 5.2.7 for details about the test statistic).

Likelihoodα and A-C test statistics is higher than the fluence required to be larger than only one of them. A possible way to understand the problem is by reasoning in terms of upper-limits. If one method is applied to the data and no excess is found with respect to the background expectation, then an upper-limit can be set. If the other method is applied to the data with the same result, the upper-limit that can be set using the "AND" of the two methods will be less constraining than the one set using only one method.

In the case of a p-value calculation, this is valid because if no signal is found using two methods, the probability that there is a signal is even lower but in the case of the upper-limit calculation, the use of Eq. (5.18) is obviously wrong. The proper way to combine the two test statistics in the case of the upper-limit and hence in the case of the sensitivity is

$$T_{\mathrm{PE,Llh}} > T_{\mathrm{Llh}} \quad \mathrm{OR} \quad T_{\mathrm{PE,AC}} > T_{\mathrm{AC}}\,. \tag{5.19}$$

This means that the sensitivity corresponds to the fluence such that the pseudo-experiments have a probability of 90% to be above one of the median of the test statistic distributions.

Once more, it is more intuitive to think in terms of upper-limits. If a certain test statistic value is obtained from the data, then the upper-limit is the fluence that can be excluded (at a specific confidence level) because if this fluence was the one emitted by GRBs the test statistic would have been different (with a specific probability). In the case of two test statistics, the upper-limit becomes the fluence that can be excluded because if this was the one emitted by GRBs, the values of one or both test statistics would have been different, hence the "OR".

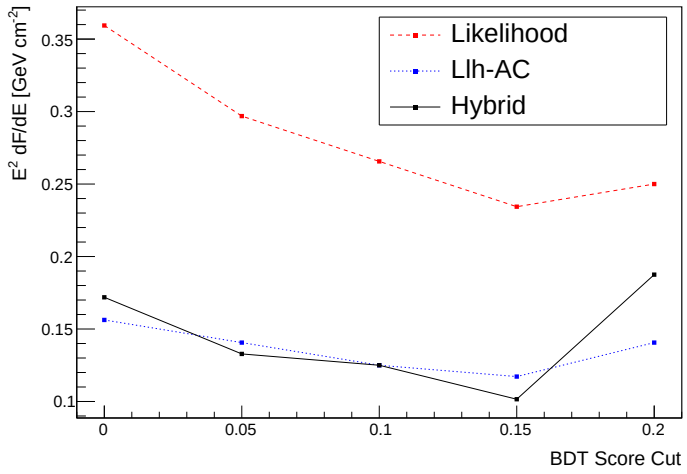

Figure 5.16: The (90% confidence level) sensitivity for the Likelihood, Hybrid and Llh-AC methods. The Hybrid and the Llh-AC methods are better than the Likelihood method.

The sensitivity for the Likelihood, Hybrid and Llh-AC methods are presented in Fig. 5.16. The 50% and 90% discovery potentials are shown in Fig. 5.17. In these figures, the fluence corresponds to all the 468 long GRBs of the 4 year sample.

From Fig. 5.16 and Fig. 5.17, remembering that only Hybrid and Llh-AC might be sensitive to precursors or afterglows, it is seen that the Hybrid method is the most suitable one for the search of neutrinos from long GRBs during the three possible phases.

In order to efficiently compare to other analyses, it is relevant to show the flux instead of the fluence. This is done for the Hybrid method only as can be seen in Fig. 5.18 and Fig. 5.19. For comparison purposes, the flux is renormalised to one year of long GRBs. Since 80% of GRBs are longs GRBs and the usual assumed number of GRBs per year is 667, the flux is renormalised to 0.8×667. This number of GRBs is used in the ICECUBE GRB group even if it is known to be inaccurate. It is actually very difficult to estimate the total number of GRBs per year because this depends on the angular acceptance as well as on the sensitivity of all satellites observing GRBs. Furthermore, GRBs that are further away have a lower probability of detection but they also have a lower contribution to the total neutrino flux. An effective number of GRBs per year would thus be more appropriate which makes the estimation even more difficult.

The purpose of the flux calculation is to compare to previous analyses as well as to theoretical predictions, as we will see in the next chapter. The precise number of GRBs per year is thus not a key value but only a necessary assumption in order to allow comparisons. Since the number 667 was used in previous analyses, this number will be used in the following.

Since these 667 GRBs represent all GRBs that have occurred during a year, including those that were not detected by satellites, the flux is calculated as quasi-diffuse. This means that if

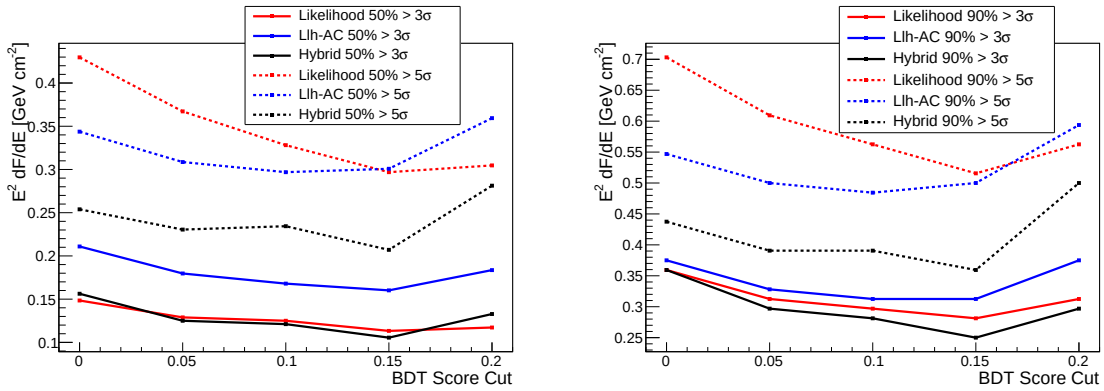

(a) 50% discovery potentials (b) 90% discovery potentials

Figure 5.17: The 50% and 90% discovery potentials for the Likelihood, Hybrid and Llh-AC methods. The Hybrid method is the best one.

the fluence is F_0, the flux Φ_0 is

$$\Phi_0 = \frac{F_0 \times 0.8 \times 667}{4\pi \times 365.25 \times 24 \times 3600 \times 468}. \tag{5.20}$$

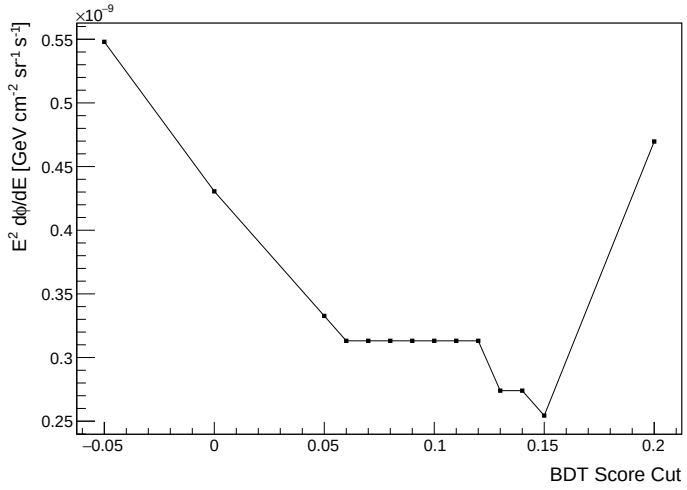

Figure 5.18: Flux sensitivity (90% confidence level) for the Hybrid method. The chosen BDT score cut is 0.07.

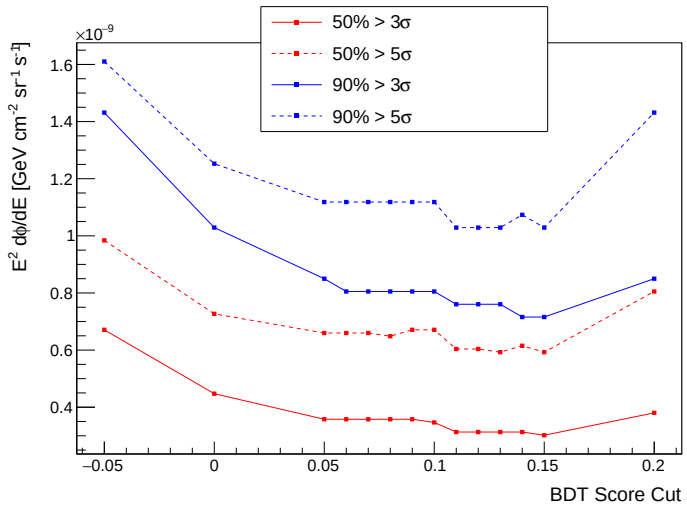

Figure 5.19: Flux discovery potentials for the Hybrid method. The chosen BDT score cut is 0.07.

As can be seen from Fig. 5.19, the discovery potentials are mainly flat between 0.05 and 0.15. The structures arising after 0.1 are due to the lack of statistics in the background sample. A possible effect that can contribute to these structures could be that the number of events in the 3° angular window for of the A-C method becomes too low (one needs at least two events to form a pair).

The BDT cut value should be as small as possible to preserve a maximum amount of signal but it should not be too low in order to avoid leaving the plateau. The chosen BDT score cut value is 0.07. The summary table with the various sensitivity and discovery potential values for the 0.07 BDT score cut value is shown in Table 5.2. These final sensitivity and discovery potential values are a factor three better than those of the previous IC86 analysis [82].

Table 5.2: Summary table of the sensitivity and discovery potentials of the analysis. The sensitivity as well as the discovery potentials are a factor 3 better than in the previous IC86 GRB analysis [82]. The fluence is the total fluence of the 468 GRBs; the number of neutrinos are corrected for the signal efficiencies (i.e. this is the number of neutrinos at Level2) and the flux is re-normalised to 0.8 × 667 long GRBs per year.

	Fluence [GeV cm^{-2}]	#neutrinos(over 468GRBs)	Flux [GeV cm^{-2} s^{-1} sr^{-1}]
Sensitivity	0.125	8	3.6×10^{-10}
50% DP (5σ)	0.230	14.7	6.6×10^{-10}
90% DP (3σ)	0.390	24.8	1.1×10^{-9}

6

Results and discussion

In this final chapter, the results of the search for neutrinos in correlation with long GRBs in the Northern Hemisphere using four years of IceCube data are presented. The various steps of the analysis explained in the previous chapters were presented to and reviewed by the IceCube collaboration prior to the approval for the application of the analysis procedure to the data. This reflects the strict unblinding policy within the IceCube collaboration. After the description of the various systematic errors of the current analysis, the calculation of the significance of a possible signal using the optimised statistical method described in the previous chapter will be presented. It will be followed by several possible upper-limits on the flux and the fluence of neutrinos emitted from long GRBs. Finally, the various model constraints that the results of this analysis imply will be discussed.

6.1 Systematic errors

The main systematic errors come from the neutrino simulations. They are used in every step of the analysis, from the event selection optimisation to the calculation of upper-limits. Since the uncertainty on the DOM efficiency or on the ice models did not change since the previous GRB analysis [82], the systematic errors of that analysis will be used. If a difference in the simulations had appeared in between the two analyses, this could only reduce the overall systematic error. Hence, using the previously calculated systematics is conservative. The calculation of the systematic errors by the various uncertainties explained below is performed for an E^{-2} energy spectrum.

The systematic errors arise from several sources. The first one is the quantum efficiency

Table 6.1: Summary of the systematic errors for an E^{-2} spectrum [82].

DOM efficiency	+4%
Ice properties	+1.7%
Others	+8%
Total	+9.1%

of the PMTs inside the DOMs. A lower efficiency of the DOM would lead to the detection of a smaller number of photo-electrons which would affect the reconstructions as well as several variables used in the BDT. The DOM quantum efficiency is estimated to ±10% [93]. The effect on the various reconstructions and variables can be estimated by using dedicated simulations with variable DOM efficiencies. It was found that the uncertainty on the efficiency of the DOM lead to a conservative uncertainty on the upper-limits of 4% [82].

A second source of uncertainties is the photon propagation in the ice. The simulations use the ice models developed using ICECUBE measurements (see Section 2.5.2). The uncertainties on the ice models and thus on the photon propagation are estimated to be 10% [74, 82]. This yields a conservative uncertainty on the upper-limits of 1.7%. The other errors that contribute to the systematic errors are the uncertainty on the neutrino interaction cross-section at high energies and the uncertainties on the bed rock density which is located beneath ICECUBE. These other errors contribute to the systematics by 8% [82].

The sum in quadrature of the effects listed above gives a total conservative systematic error of 10% with respect to baseline as shown in Table 6.1. This error has been included in the upper-limits presented hereafter by an increase of the calculated upper-limits by 10%.

6.2 Significance of the observations

After having applied the event selection described in Chapter 4, the number of remaining events is 6408. As explained in the previous chapter, the calculation of the significance is performed using the Hybrid method. In this method, the Likelihoodα and A-C test statistics are computed on the data and compared to the background test statistic expectations in order to obtain a p-value. The number of events inside the 10° angular windows around the GRBs used for the Likelihoodα test statistic calculation is 90 while the number of background events (same angular window size but opposite azimuth) is 93. These 90 events are presented in Table 6.2. The BDT distributions of the remaining events after the event selection and after the time and the angular selections are shown in Fig. 6.1. In the case of the A-C test statistic, 7 events were selected inside the 3° angular windows.

In order to take the detector acceptance dependency into account, a specific procedure was followed in the background test statistic calculation. Instead of using the background test statistic distributions computed for the sensitivity and discovery potentials, the measured arrival directions were scrambled in right ascension keeping the declination of the events to

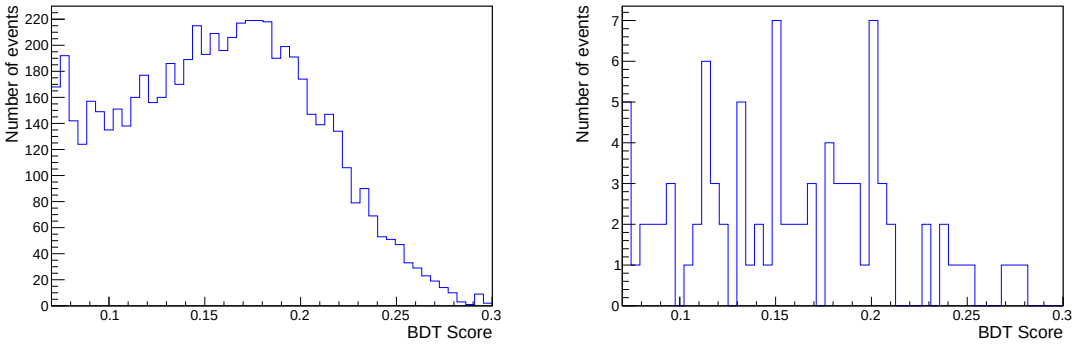

(a) (b)

Figure 6.1: BDT score distribution of the final event sample. The BDT score distribution after the event selection (6408 events) is shown on panel (a) and after the time and angular window selections (90 events) is shown on panel (b).

account for the strong declination acceptance dependency of the detector.

The Hybrid method applied on the data yielded a Likelihoodα test statistic of 0 corresponding to the background expectations and an A-C test statistic of 1.3 also compatible with the background expectations. The p-value obtained after randomisation is 47% which is perfectly compatible with the background-only hypothesis. Following this result, upper-limits on the flux of neutrino emission from long GRBs have been calculated.

Table 6.2: Final event selection in a time window of 1 hour around GRB trigger times and in angular windows of 10° around the GRB positions.

GRB Name	time (w.r.t. GRB trigger) [s]	angular separation [deg]	σ_{GRB} [deg]	T_{90} [s]
110517B	-938.901	6.56229	2.11	23.04
110520A	502.73	7.61633	0.0003	15.7
110521A	-984.91	4.12287	0.0003	13.8
110522A	1372.48	8.16832	5.56	28.16
110601A	116.897	4.87636	3	52.21
110626A	1695.44	4.10439	7.66	6.4
110906B	-472.433	5.75685	4.03	23.94
110915B	1167.86	8.55315	0.0405	18
110921A	-1580.56	9.89821	0.0003	48
110928B	-245.104	6.61123	1.42	148.23
111012A	133.011	9.12516	2.08	20.74
111216A	-934.495	8.23897	1.37	83.78

Table 6.2: Final event selection in a time window of 1 hour around a GRB trigger time and in an angular window of 10° around the GRB position.

GRB Name	time (w.r.t. GRB trigger) [s]	angular separation [deg]	σ_{GRB} [deg]	T_{90} [s]
120120A	-947.445	8.12932	5.71	32.26
120206A	254.162	9.39681	2.25	9.48
120226A	-1249.34	2.36405	0.5	80
120412B	287.257	6.16365	2.8	101.19
120415C	1436.22	7.00936	4.96	12.54
120422A	1508.53	8.56364	0.0003	5.35
120504A	-363.784	7.88869	4.06	41.98
120703C	-1160.2	5.63873	5.15	77.57
120802A	470.449	7.6431	0.0005	50
120806A	-1119.91	8.8078	4.25	26.63
120811C	-1075.36	3.85431	0.0003	26.8
120811C	686.947	7.69957	0.0003	26.8
120824A	-1496.9	9.73056	3	111.62
120916A	-982.886	5.30849	0.4953	26
121102B	204.502	4.05815	12.15	2.05
121122B	797.708	9.16222	12.89	8.7
121125A	-1754.28	9.76959	0.0003	52.2
121210A	-689.703	4.55511	8.25	12.8
121211B	1221.06	6.99559	5.23	8.96
130112A	-940.463	9.90818	4.93	35.33
130115A	-164.208	9.41083	2.78	13.57
130304A	658.171	9.76396	1.2	67.84
130307B	-775.483	9.92602	4.42	63.49
130409A	350.41	5.36148	2.22	26.11
130418A	-114.989	9.95056	0.0003	300
130521B	-440.986	9.72786	0.1207	23
130528A	828.712	8.70351	0.0003	59.4
130528A	1288.72	6.14462	0.0003	59.4
130528B	-286.466	6.8758	5.5	66.3
130530A	-1343.96	9.38044	1.04	58.62
130606C	-701.196	7.35	1.67	24.13
130612A	-1296.39	8.52169	0.0003	7.42
130612A	1421.26	1.33075	0.0003	7.42
130623C	658.138	9.15863	7.12	44.55
130630A	-1031.15	6.04709	1	17.15
130725A	550.776	3.7009	0.0253	101.8

Table 6.2: Final event selection in a time window of 1 hour around a GRB trigger time and in an angular window of 10° around the GRB position.

GRB Name	time (w.r.t. GRB trigger) [s]	angular separation [deg]	σ_{GRB} [deg]	T_{90} [s]
130725C	-1215.99	8.68262	2.27	6.65
130828B	-1458.8	0.685197	2.43	3.91
130906A	-528.512	3.28168	12.39	11.26
130925B	1181.03	6.79858	4.12	265.47
131018B	1763.65	9.00118	0.13	39.93
131108A	-848.809	9.82181	0.5	23.04
131202B	87.4588	6.04182	2.24	86.02
140112A	302.918	8.62192	7.14	12.03
140112A	1272.18	5.38828	7.14	12.03
140215A	455.411	8.12483	0.0003	84.2
140217A	1208.16	4.65842	3.08	41.48
140224A	778.962	9.52388	5.93	2.3
140224B	-1008.4	9.47442	3.69	17.15
140311B	465.048	2.10286	0.0003	72.19
140404A	-562.602	7.51324	4.88	84.99
140404B	-37.2965	9.26229	2.19	26.63
140501B	1545.61	9.48612	2.73	22.15
140517A	1450.53	1.88882	2.17	20.48
140518A	1700.62	4.10182	0.0182	60.5
140521A	-1499.75	5.72273	0.0111	11.55
140521A	-804.649	9.1531	0.0111	11.55
140523A	690.434	8.93297	0.4	22
140608B	1392.05	9.27475	2.91	6.4
140610C	1230.3	5.91901	1	36.86
140621A	1049.45	6.91958	0.72	6.3
140628C	174.444	9.60202	9.04	75.52
140705B	1484.73	6.78417	5.83	26.88
140819A	1403.03	6.72819	12.02	6.65
140824A	-1079.95	8.42093	0.0003	3.09
140824A	498.454	2.80036	0.0003	3.09
140906A	-1265.15	7.91396	7.66	37.63
140907A	-1207.81	5.51534	0.0002	79.2
140907A	-730.183	6.38788	0.0002	79.2
141029B	-0.690936	9.25313	1	202.44
141102C	255.451	9.33452	12.79	25.08
141102C	1015.63	4.70181	12.79	25.08

Table 6.2: Final event selection in a time window of 1 hour around a GRB trigger time and in an angular window of 10° around the GRB position.

GRB Name	time (w.r.t. GRB trigger) [s]	angular separation [deg]	σ_{GRB} [deg]	T_{90} [s]
141102C	1445.52	9.01822	12.79	25.08
141226A	568.84	3.8334	6.26	38.65
141230A	-1573.79	3.79399	3.86	9.86
141230A	465.158	6.05288	3.86	9.86
150120B	380.741	9.87506	0.0002	24.3
150131B	1756.77	0.621863	5.31	8.2

6.3 Upper-limits

6.3.1 Prompt flux upper-limit

There are several ways to calculate upper-limits. The most straightforward method is almost identical to the sensitivity calculation. Instead of using the median of the background test statistic distribution, the test statistic values obtained from the data are used. In the case of a 90% confidence level (CL) upper-limit, the fluence corresponding to the upper-limit is the one for which 90% of the pseudo-experiments give test-statistic values strictly larger than the ones obtained from data. For this upper-limit, as for the sensitivity calculation, the signal injection corresponds to a prompt signal.

As explained in the previous chapter, in the Hybrid method, the test statistics of the pseudo-experiments T_{PE} are larger than those of data T_{data} if $T_{\mathrm{PE}} > T_{\mathrm{data}}$ for the Likelihoodα test statistic OR if $T_{\mathrm{PE}} > T_{\mathrm{data}}$ for the A-C test statistic.

The first upper-limit is calculated using the above method and assuming a generic E^{-2} spectrum. The obtained value is 0.146 GeV cm^{-2} for the 468 long GRBs[1]. This corresponds to a flux[2] of 4.2×10^{-10} GeV cm^{-2} sr^{-1} s^{-1} assuming 0.8×667 long GRBs per year. Such a limit allows to be model independent but has the drawback that it cannot be used for model constraints nor can be compared to previous ICECUBE limits.

In order to compare to previous ICECUBE results as well as to set constraining limits on models, a model dependent limit has been calculated. This limit is computed using a doubly broken power spectrum. If the first energy break is ϵ_{b} and the flux normalisation is Φ_0, the

[1] The systematic errors are included in this value.

[2] This flux is quasi-diffuse because a solid angle of 4π sr is used in its calculation.

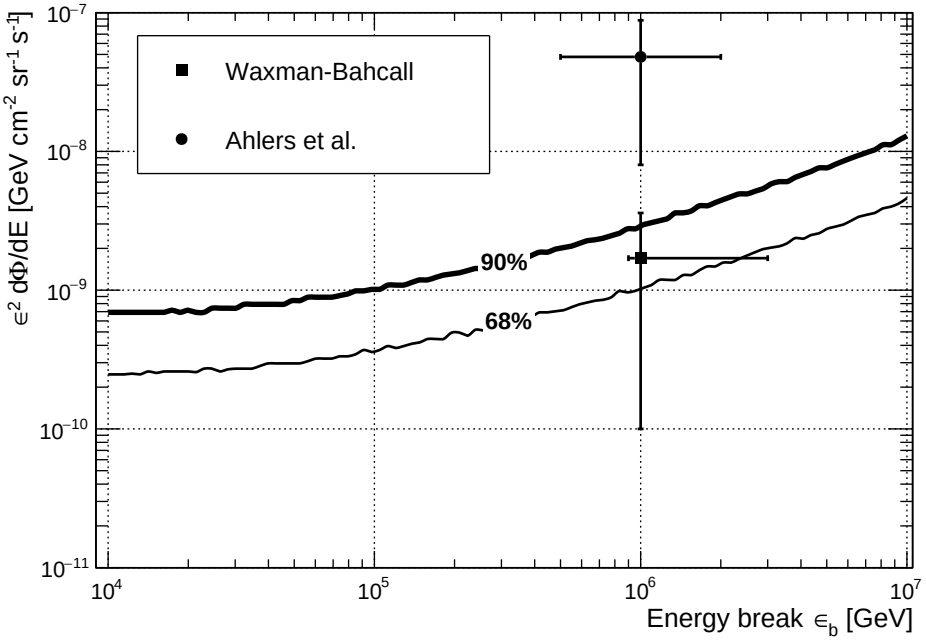

Figure 6.2: Upper-limits (90% and 68% CL) on the flux of neutrinos from long GRBs as a function of the energy break ϵ_b assuming 0.8×667 long GRBs per year. The Alhers et al. prediction is clearly excluded and the Waxman-Bahcall prediction is in tension with the limits.

flux model can be written as [84]

$$\frac{d\Phi}{dE} = \Phi_0 \times \begin{cases} E^{-1}\epsilon_{\rm b}^{-1} & \text{if} \quad E < \epsilon_{\rm b}\,, \\ E^{-2} & \text{if} \quad \epsilon_{\rm b} \leq E < 10\epsilon_{\rm b}\,, \\ E^{-4}\,(10\epsilon_{\rm b})^2 & \text{if} \quad E \geq 10\epsilon_{\rm b}\,. \end{cases} \tag{6.1}$$

This model follows the following assumptions. When the protons have enough energy to interact with any surrounding photons to produce neutrinos, the neutrino spectrum follows the proton one (assumed to be E^{-2}). For lower energy protons, the neutrino production is efficient only if protons interact with photons that have a sufficient energy and this changes the neutrino spectrum to E^{-1} below $\epsilon_{\rm b}$. At a certain energy, the synchrotron energy loss of the pions produced by the proton-photon interactions cannot be neglected and this steepens the neutrino spectrum to E^{-4} (above $10\epsilon_{\rm b}$) [82].

The upper-limits calculated using this spectrum as a function of $\epsilon_{\rm b}$ are shown in Fig. 6.2. As for the sensitivity calculation the flux is calculated by renormalising the computed fluence by assuming that there are 0.8×667 long GRBs per year. The systematic errors explained in the previous section are included in this limit. The expected flux from the Alhers et al. [52] and Waxman-Bahcall [48] models are shown with their possible parameter variations.

From Fig. 6.2, one can see that the Ahlers et al. model of the neutron escape is strongly

excluded while the Waxman-Bahcall model of the proton escape is in tension with the limits. The flux predictions of the two models have been lowered with respect to those published in [84] to take into account that the current study focuses on long GRBs which represent 80% of all GRBs in our 4 year sample.

Unfortunately, the obtained upper-limits do not allow to draw newer conclusions than the ones of the combined IC40-IC86 GRB analysis [84]. This combined analysis included 508 GRBs which represents a larger sample than the one used in the current analysis.

6.3.2 Precursor upper-limit

Since our analysis is sensitive to possible precursor neutrinos, it is possible to set a limit on the precursor fluence. However, it is difficult to use a precise model for the precursor spectrum as well as for their time PDF. A solution is to use a generic E^{-2} energy spectrum and to use several possible time differences between precursor neutrinos and GRB trigger times.

As in the toy-model (see Section 5.1.3), the neutrinos are assumed to be emitted at a precise time before the GRB trigger time at the source. The simulated times of the events in the detector are then smeared because of the GRB redshifts. If for a GRB the redshift could not be measured, a redshift is drawn randomly from the SWIFT redshift distribution shown in Fig. 5.3. The assumption is made that our 468 long GRBs constitute a fair sample of all observed long GRBs such that the unknown redshifts can be chosen randomly from the SWIFT redshift distribution. As explained in Section 5.1.3, the redshift distribution is biased toward lower values due to the fact that closer GRBs are easier to detect. Since we are searching for neutrinos from a list of observed GRBs, the same bias applies to our list of GRBs. Thus, when selecting redshifts randomly from a distribution to compensate for the missing redshifts of the GRBs in our list, one should use a distribution of observed GRBs. The various 90% CL upper-limits are presented in Fig. 6.3. These are the first ever upper-limits on precursor neutrinos from GRBs as a function of the emission time.

A previous upper-limit was calculated using the ICECUBE detector in its 22 string configuration (IC22) [94] assuming a precursor emission within a time window of 100 s before the GRB trigger times. This limit is model-dependent and assumes an energy spectrum that follows a E^{-2} spectrum until a break at 10 TeV followed by clear drop at 60 TeV [94]. Furthermore, the injection does not take into account the smearing effect of the redshift. A direct comparison with the limit shown in Fig. 6.3 is thus difficult.

In order to achieve a comparison, a limit was calculated using the same injection time window and in the conservative choice of a suppresion of the injection above 60 TeV. The obtained limit on the fluence is 0.163 GeV cm^{-2} for the 468 long GRBs. Since the previous limit was around 0.5 GeV cm^{-2} for 41 GRBs, our limit represents an improvement by a factor 35.

However, once this limit is compared to the original fluence prediction (see [85] for details), one needs to take into account the effect of the redshift in order to avoid an underestimation of the upper-limit. Once the effect of the redshift is properly treated, the obtained

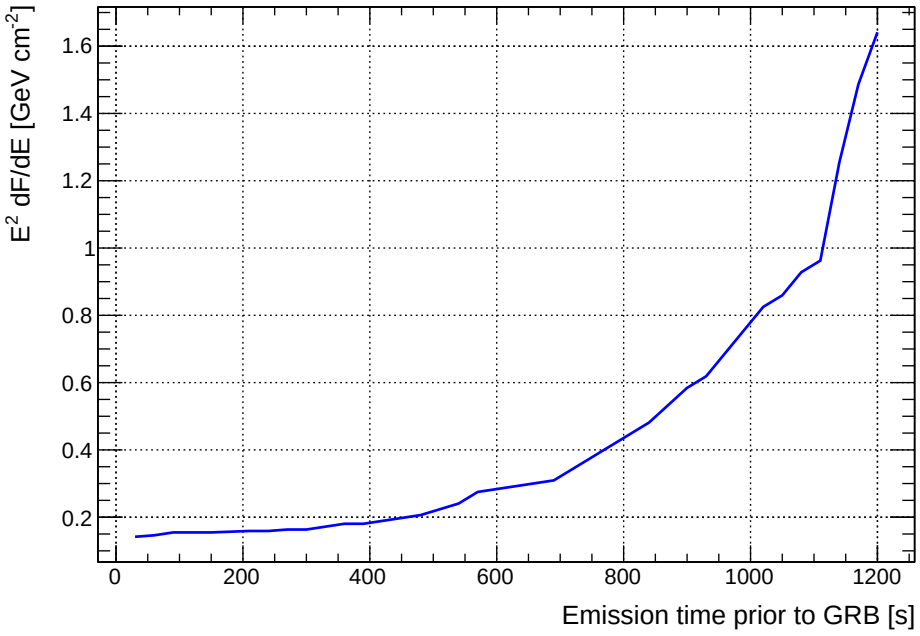

Figure 6.3: Upper-limits (90% CL) on the fluence of precursor neutrinos from 468 long GRBs as a function of the emission time prior to the GRB trigger times. These limits assume an E^{-2} energy spectrum. These are the first ever limits on the fluence of precursor neutrinos as a function of the emission time.

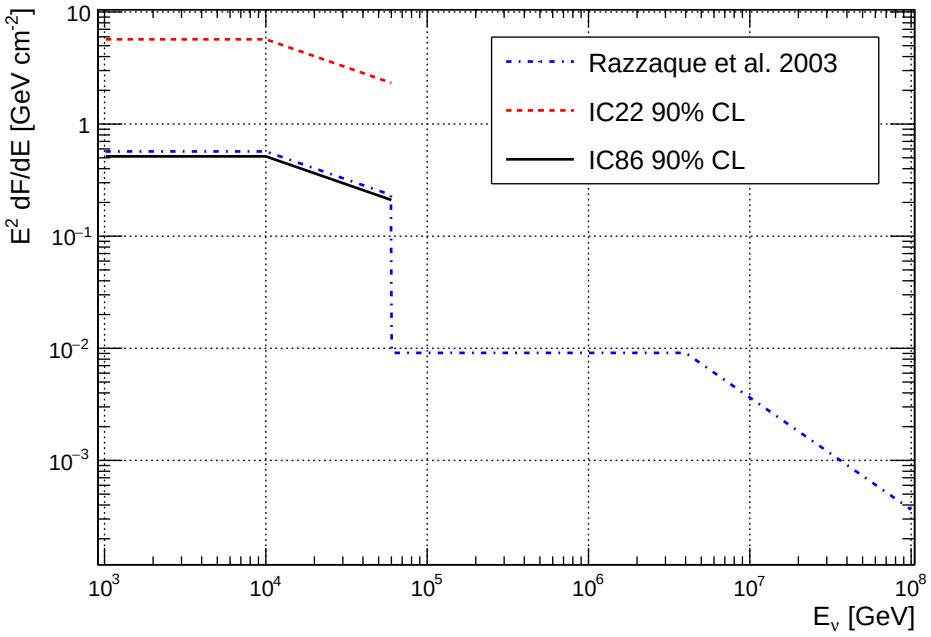

Figure 6.4: Upper-limits (90% CL) on the fluence of precursor neutrinos from 468 long GRBs. The Razzaque et al. [85] prediction for a H-star is in blue, the IC22 upper-limit scaled to 468 GRBs is in red and the upper-limit obtained in the current thesis is in black. The obtained limit is below the theoretical prediction of Razzaque et al. for a H-star and improves by a factor 11 the previous IceCube limit in which redshift effects were not taken into account.

upper-limit increases to be 0.515 GeV cm^{-2} which is 11 times lower than the IC22 limit. Despite this increase due to the effect of redshift, this limit remains lower than the predicted fluence in the case of a H-star[85] as can be seen from Fig. 6.4. This means that the scenario that assumes that GRBs are the results of the collapse of a star composed of a helium core surrounded by a hydrogen shell is constrained by the obtained upper-limit.

6.3.3 Bayesian upper-limit

The above upper-limits need to assume a specific signal time PDF. It is possible to set an upper-limit based on the 468 samples of one hour centered at the GRB trigger times without assuming a specific source PDF by using the method described in [89]. This method, developed by our Brussels team in the light of the current analysis, uses the Bayesian formalism to calculate an upper-limit on the rate. It was shown to be more conservative than the traditional Feldman-Cousins method [95] while being more robust to possible under-fluctuations of the background.

Another advantage of the method is that it allows to obtain the full source PDF from which

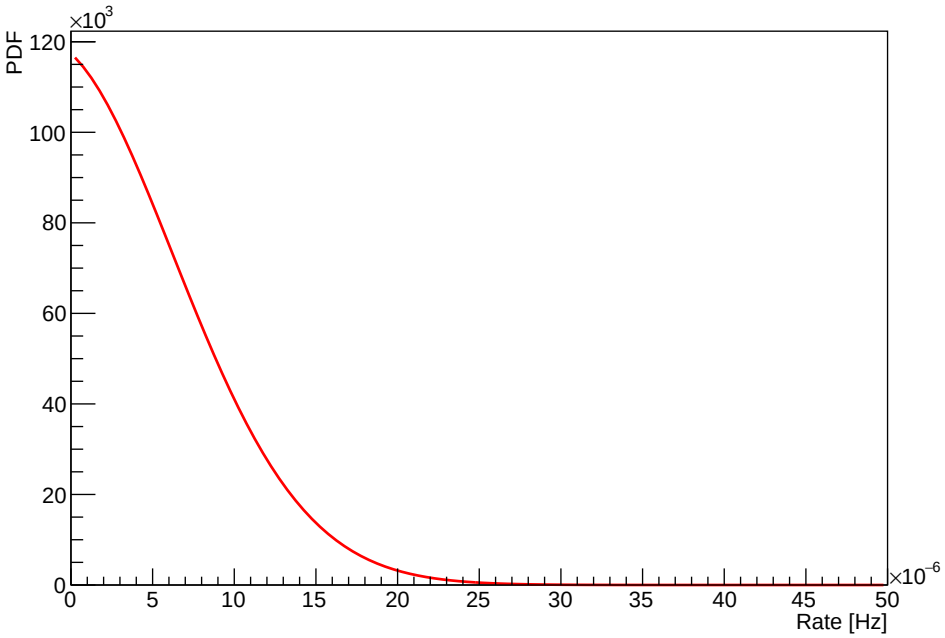

Figure 6.5: Source rate PDF obtained using the method described in [89]. The maximum corresponds to a rate of 0 events/s compatible with the background expectation. The integration of the PDF gives an upper-limit.

a simple integration yields the 68% CL, 90% CL or any other upper-limits. Using the measured number of off-source events (93) and of on-source events (90) as well as the on-time (1684800 s) which is equal to the off-time, the obtained 90% CL upper-limit is 1.375×10^{-5} event/s. The source PDF is shown in Fig. 6.5. From this figure, one can notice that the maximum of the PDF is realised for a rate equal to 0 event/s. This is expected since the observed data are compatible with the background-only hypothesis.

Since we know the on-time, the number of events per GRB that this limit represents can be calculated. The obtained limit on the number of events per GRB is 0.05. This is the upper-limit on the number of events after the event selection and after the 10° angular window selection. It is interesting to remark that this number is almost 4 times higher than the number of events that corresponds to the fluence upper-limit for a prompt signal injection.

The upper-limit on the rate can also be converted to a fluence using the effective area as shown in Fig. 4.12. Since the energy averaged effective area corresponding to an E^{-2} energy spectrum is 4842 $\mathrm{GeV}^{-1}\,\mathrm{cm}^2$, the 90% CL fluence per solid angle upper-limit $f_{\mathrm{u.l.}}$ corresponding to an E^{-2} neutrino energy spectrum is

$$f_{\mathrm{u.l.}} = \frac{1.375 \times 10^{-5} \times 1684800}{4842 \times \Omega} = \frac{4.8 \times 10^{-3}}{\Omega}\,\mathrm{GeV\,cm^{-2}sr^{-1}} = 1 \times 10^{-4}\,\mathrm{GeV\,cm^{-2}sr^{-1}}\,, \qquad (6.2)$$

where Ω is the solid angle calculated as the sum of the 468 patches of 10°. This result is inter-

esting as its calculation is independent of the previous upper-limits and it allows to set a limit on the fluence per solid angle for a possible neutrino emission during the 468 samples of 1 hour.

Conclusions

The analysis presented in this thesis is essentially composed of two parts, the event selection and the development of the statistical method. The event selection starts with the optimisation of the IceDwalk reconstruction and continues with the development of the QualDist method. This method as well as its optimisation procedure have been created during this thesis work for the purpose of the analysis. This new method combined with the creation of new variables used in the BDT selection allowed a gain in effective area by a factor 1.2 with respect to the previous GRB analysis [82].

The development of a toy-model for the investigation of the most sensitive method for the search of neutrinos from long GRBs allowed to design a new hybrid method that improved the sensitivity and discovery potentials by a factor 3 with respect to the previous analysis while gaining sensitivity to possible precursor and afterglow neutrinos. It is important to note that these improvements are achieved with respect to GRB analyses which are already very mature as they have improved since the AMANDA detector.

However, no significant signal from long GRBs has been found, confirming previously published results. This allowed to calculate upper-limits for the prompt and the precursor phases. The prompt upper-limits rule out the Ahlers et al. model [52] predicting that the UHECRs originate from neutrons escaping the fireball. The Waxman-Bahcall model [48] predicting that the UHECRs originate from proton escape of the fireball could not be excluded even if the limits restrict its parameter variations. These results, combined with the fact that the search for neutrinos from short GRBs [96] did not detect any significant signal either, strongly constrain the hypothesis that GRBs are the main sources of UHECRs.

For the first time in ICECUBE, upper-limits on the fluence of precursor neutrinos as a function of their emission time have been set. Furthermore, the limit obtained with our analysis using the signal injection of the previous ICECUBE precursor limit improved the previous published limit by a factor 35. This improvement, once redshift effects are taken into account, allows to set a 90% upper-limit which is lower than the predicted precursor fluence in the case of a H-star as described in [85].

It is important to remark that the current analysis has been optimised for discovery; from the design of the toy-model comparing p-values to the optimisation of the BDT score cut mainly based on discovery potentials. Since the various searches performed with the ICECUBE detector, using different event selections and different statistical methods, did not find

any significant neutrino signal in correlation with GRBs, a GRB neutrino signal is to my opinion unlikely to appear in a cubic kilometer scale detector in a near future.

In the analysis that has been described in this thesis, the event selection allowed to analyse events that were discarded in previous analyses [82]. Furthermore, the energy PDF constraint used in previous likelihood based analyses was relaxed and the time window was extended to an hour in order to be sensitive to prompt, precursor and afterglow neutrinos. Yet, no significant signal was found. The main conclusion of this thesis is that the GRB analyses in ICECUBE have arrived at a turn. Future analyses should not be optimised on discovery as it was done until now but they should focus on the improvement of the sensitivity in order to lower the possible upper-limit and definitely rule out GRBs as main sources of UHECRs.

However, there are several improvements of the analysis that could increase the probability of a neutrino signal detection from GRBs. An analysis that uses more years of data could restrict to well-located GRBs in order to improve the Likelihood method sensitivity to signal events. Another possibility, in the case of a precursor search, is to restrict an analysis on GRBs with a measured redshift such that the arrival times of the events could be corrected for the redshift prior to the use of a statistical method. A selection of GRBs that have the highest γ fluence would also be an interesting subset to study.

In the attempt of developing an analysis that would be optimised on the best possible upper-limit instead of the discovery potential, one should not use the toy-model as it was described in the current analysis. This is due to the fact that comparing p-values allows to search for the method that is the most suitable for a discovery but this method might not be the one that would set the most stringent upper-limits.

Hence, if a future analysis is designed to definitely rule out GRBs as main sources of the UHECRs, it should select the statistical method based on the possible upper-limit in the case of an absence of signal. If such a strategy was followed in the current analysis, the Likelihood method would not be chosen because its background distribution, containing a large peak at zero, is not optimal for an upper-limit calculation. Another method would have been more appropriate which might have led to a different BDT score optimisation and in the end possible better upper-limits.

One should realise that ruling out GRBs as main sources of UHECRs does not rule out neutrino production in GRBs. The presence of hadrons in the case of a collapse of a massive star combined with the observed γ-rays should produce neutrinos but the flux of these neutrinos could be lower than the Waxman-Bahcall prediction if GRBs only contribute to a small amount (or not at all) of the UHECRs. As mentioned above, in the light of recent ICECUBE results, I doubt that these neutrinos will be detected in a cubic kilometer detector. However, the future Gen2 detector [97] which is planned to be 10 times larger than ICECUBE and which includes a denser core that would lower the current ICECUBE energy threshold will strongly increase the detection effective area. With such a detector, the search for neutrinos from GRBs would enter a different phase. One would not attempt to prove or rule out that GRBs are the main sources of UHECRs but one would estimate the contribution of GRBs to the UHECR flux

and in the case of a non observation of neutrinos, one could severely constrain the presence of hadrons in GRBs.

Summary

In the beginning of the last century, several scientists discovered an ionising radiation that seemed to come from the sky. After experiments at high altitudes using balloons, it was found that charged particles coming from space were the cause of this radiation. These particles were called cosmic rays.

Since their discovery, scientists have tried to identify the sources of these cosmic rays. More specifically, the origin of the high energy cosmic rays is an enigma as one also needs to explain the mechanism behind their acceleration. Within our Galaxy, supernovae are believed to be responsible for the high energy cosmic rays.

However, at even higher energies, the sources of the so-called Ultra High Energy Cosmic Rays (UHECRs) are believed to be located outside our Galaxy. This is due to the fact that at a certain energy, the magnetic field of our Galaxy is not sufficient anymore to contain these particles.

The search for the sources of the UHECRs is thus focusing on the highest energetic phenomena outside our Galaxy. Since the most powerful objects known are Gamma Ray Bursts (GRBs) in which the energy of a supernova is released in just a few seconds, it is natural to associate these objects to the UHECRs.

Such an association implies the presence of protons (being the main component of the UHECRs) inside the GRBs. This is supported by the generally accepted GRB progenitor hypothesis. This hypothesis states that GRBs originate from the collapse of extremely massive stars or from the merger of compact binary systems like neutron stars and black holes. In both cases such a cataclysmic event would create a black hole generating the power required to accelerate the surrounding matter.

Following this scenario, the accelerated protons should interact with the ambient energetic photons to produce pions and subsequently high-energy neutrinos. Hence the detection of high-energy neutrinos from GRBs would provide an unique proof that the GRBs contain a hadronic component and that they are sources of UHECRs.

Since neutrinos are electrically neutral and interact only very weakly, they directly point back to their source and can reach the Earth unhindered. However, their detection requires a very large detector. Such a detector has been built at the South Pole where a cubic kilometer of ice has been instrumented with light detectors to form the IceCube observatory.

The analysis developed in the current thesis focuses on long duration GRBs (longer than 2

s) which are believed to originate from star collapses while the short duration GRBs (shorter than 2 s) are believed to originate from compact binary mergers. The selection of the events detected by the IceCube detector has been designed and optimised to search for a specific type of neutrino, the muon neutrino. The reason for this is that these neutrinos may produce a muon, which leaves a track like signature in the detector that allows to reconstruct the location of its origin.

Using a newly developed event selection, the background (mainly composed of muons produced in cosmic ray interactions in our atmosphere) could be dramatically reduced while allowing for a better signal acceptance than previous IceCube GRB analyses.

Once the background events were rejected and the neutrino induced events coming from the Northern Hemisphere (to use the Earth as a shield against the atmospheric muon background) were extracted from the data, a study of statistical methods was performed in order to define the most suitable method to search for neutrinos from long GRBs. This statistical method is required to state how significant our observations are. The newly designed statistical method allowed to improve the sensitivity of the analysis by a factor three with respect to previous analyses while extending the search time around the GRB to one hour, instead of the usual so-called prompt emission studies.

Unfortunately, no significant signal events in correlation with GRBs have been observed. This allowed to set upper-limits on the neutrino flux from GRBs. These limits rule out the model that predicts that the UHECRs originate from neutrons escaping the high intensity magnetic field surrounding GRBs. The model that predicts that a part of the protons accelerated by the GRBs do not interact with photons and form the UHECRs is not excluded but its parameter variations are constrained.

Furthermore, a limit on the fluence of neutrinos that could be emitted prior to the observed GRB when the environment is still opaque to photons has also been calculated. This limit as a function of the emission time prior to the GRB is the first one ever set by an (IceCube) analysis and represents thus a novel result. The previous limit by IceCube on such precursor neutrinos was calculated by assuming a specific model and only a time offset of about 100 s. The current analysis allowed to improve this previous limit by a factor 35.

The various models predicting neutrinos from GRBs are more and more constrained and if no signal neutrinos are found in the near future, GRBs will be definitely ruled out as main source of the UHECRs.

Samenvatting in het Nederlands

Begin vorige eeuw ontdekten wetenschappers dat er ioniserende straling was in onze atmosfeer. Experimenten op hoge hoogtes met behulp van ballonnen wezen uit dat deze straling veroorzaakt wordt door geladen deeltjes uit de ruimte die onze atmosfeer bombarderen. Deze geladen deeltjes werden kosmische stralen genoemd.

Wetenschappers trachten, sinds de ontdekking van de komische stralen, de origine van deze straling te achterhalen. Tot vandaag blijft deze origine een raadsel aangezien het mechanisme dat de geladen deeltjes versnelt nog niet begrepen is. Er wordt aangenomen dat, binnen ons sterrenstelsel, de Melkweg, supernovae de oorzaak zijn voor de versnelling van hoogenergetische kosmische stralen.

Op nog hogere energieën kunnen ultra-hoogenergetische kosmische stralen (UHEKS) ontsnappen uit het magnetisch veld van de Melkweg. Daarom wordt verondersteld dat de bronnen van deze UHEKS zich waarschijnlijk buiten onze Melkweg bevinden.

De zoektocht naar de oorsprong van deze UHEKS richt zich daarom op de hoogst energetische fenomenen buiten de Melkweg. Aangezien Gamma Ray Bursts (GRBs) de hoogst energetische, waargenomen objecten zijn, is het natuurlijk om deze objecten te linken aan de UHEKS. Tijdens een GRB wordt de energie van een supernova vrijgelaten in enkele seconden.

De associatie van de UHEKS met GRBs impliceert dat er protonen (de dominante component van de UHEKS) aanwezig moeten zijn in de GRBs. Deze aanname wordt ondersteund door de algemeen aanvaarde GRB progenitor hypothese die stelt dat GRBs afkomstig zijn van de ineenstorting van extreem massieve sterren, of van de fusie van dubbelsterren waarbij beide sterren neutronensterren zijn. In beide gevallen zou een zwart gat gecreëerd worden in dit extreem destructieve proces en zou het nodige vermogen gegenereerd worden om de materie van de ster te versnellen tot extreme energieën.

In dit scenario zouden de versnelde protonen interageren met de fotonen, waarbij vervolgens pionen en hoogenergetische neutrino's gecreëerd worden. De detectie van hoogenergetische neutrino's die geassocieerd zijn aan GRBs, zou dan een rechtstreeks en uniek bewijs zijn dat GRBs afkomstig zijn van de implosie van sterren en dat zij verantwoordelijk zijn voor de productie en versnelling van UHEKS.

Aangezien neutrino's slechts heel zwak interageren, vereist de detectie van deze deeltjes een gigantische detector. Zulk een detector is gebouwd op de Zuidpool, waar een kubische kilometer ijs geïnstrumenteerd is met licht sensoren. Deze neutrino detector wordt de IceCube neutrinodetector genoemd.

De analyse die ontwikkeld is in het onderzoek dat beschreven wordt in deze thesis focust op lange GRBs (langer dan 2 s), die vermoedelijk afkomstig zijn van de ineenstorting van massieve sterren, daar waar korte GRBs (korter dan 2 s) waarschijnlijk afkomstig zijn van de fusie van dubbelsterren waarbij beide sterren neutronensterren zijn. De selectie van 'events' gedetecteerd door IceCube werd ontwikkeld en geoptimaliseerd om te zoeken naar een bepaald type neutrino, namelijk het muon-neutrino.

Gebruik makende van deze vernieuwende event-selectie werd de achtergrond straling in de detector, die vooral bestaat uit atmosferische muonen, sterk gereduceerd. Bovendien was de ontwikkelde event-selectie efficiënter voor het behoud van de verwachte GRB geassocieerde neutrino's dan voorgaande selecties.

Eens de achtergrond muonen en neutrino's verwijderd waren en de neutrino's komende van het noordelijk halfrond geselecteerd waren, werd bestudeerd welke statistische methode het best gebruikt kon worden voor de zoektocht naar neutrino's geassocieerd met lange GRBs. Deze statistische methode is nodig om te berekenen hoe significant een observatie is. Een nieuwe methode werd ontwikkeld en deze methode verhoogde de sensitiviteit van de analyse met een factor drie tegenover voorgaande analyses. Bovendien werd in deze analyse tot zowel een uur voor als na de GRB gezocht naar neutrino's, daar waar andere analyses zoeken naar neutrino's die simultaan met de fotonen van de GRBs aankomen op aarde.

Spijtig genoeg werd geen significant signaal gevonden in correlatie met de GRBs. Er werden dus bovenlimieten gezet op de mogelijke neutrinoflux afkomstig van GRBs. De gevonden limieten weerleggen modellen die voorspellen dat UHEKS afkomstig zijn van neutronen die ontsnappen van het intense magnetische veld rondom de GRB. Het bekende model van Waxman-Bahcall, dat voorspelt dat een deel van de protonen die versneld zijn in de GRB niet interageert met fotonen, is niet uitgesloten, maar de mogelijke variaties van de parameters in dit model zijn sterk beperkt.

Ook werd er een limiet gezet op de 'fluence' (stroom) van neutrino's die uitgezonden kan zijn voorgaande aan de GRB, wanneer de fotonen nog niet kunnen ontsnappen. Het is de eerste keer dat een dergelijke limiet, die weergegeven werd als functie van de tijd van emissie voor de GRB, bepaald werd voor een IceCube analyse. De vorige, gelijkaardige limiet die berekend werd, ging uit van een specifiek model, daar waar de hier berekende limiet algemener is. Vergeleken met de voorgaande limiet is deze analyse 35 keer gevoeliger.

De verschillende modellen die neutrino's van GRBs voorspellen worden nu meer en meer beperkt. Indien in de nabije toekomst geen signaal van neutrino's afkomstig van GRBs gevonden wordt, zullen GRBs definitief uitgesloten worden als belangrijkste bron van UHEKS.

APPENDIX
A

Long GRBs used in the analysis

Table A.1: List of the 468 long GRBs used in the presented analysis. A redshift of -2.150 indicates that the redshift of that GRB was not measured.

Name	RA(deg)	Decl(deg)	Err(deg)	T90(s)	Date	UT(Trigger)	F(Erg/cm^2)	Z
GRB110517B	190.1500	6.2900	2.1100	23.040	2011-05-17	13:44:47.600	8.740e-006	-2.150
GRB110520A	134.3410	56.4270	0.0003	15.700	2011-05-20	20:28:48.000	1.100e-006	-2.150
GRB110521A	120.1330	45.8270	0.0003	13.800	2011-05-21	15:51:31.000	4.400e-007	-2.150
GRB110522A	228.9100	55.5300	5.5600	28.160	2011-05-22	06:08:17.449	2.110e-006	-2.150
GRB110522B	184.4600	49.3300	6.4000	27.140	2011-05-22	07:06:01.931	1.060e-006	-2.150
GRB110529B	172.6000	8.7900	2.1000	45.820	2011-05-29	06:17:41.014	6.780e-006	-2.150
GRB110530A	282.0680	61.9290	0.0002	19.600	2011-05-30	15:31:02.000	3.300e-007	-2.150
GRB110531A	190.5100	11.8500	11.0600	38.650	2011-05-31	10:45:10.560	2.300e-006	-2.150
GRB110601A	310.7100	11.4800	3.0000	52.210	2011-06-01	16:20:16.076	1.240e-005	-2.150
GRB110604A	271.0030	18.4720	0.0507	45.000	2011-06-04	14:49:45.666	3.100e-005	-2.150
GRB110605A	14.9500	52.4600	1.0000	82.690	2011-06-05	04:23:32.304	1.930e-005	-2.150
GRB110610A	308.1790	74.8250	0.0003	47.000	2011-06-10	15:22:06.000	8.700e-006	-2.150
GRB110622A	133.9600	19.4600	1.7900	70.400	2011-06-22	03:47:19.105	5.430e-005	-2.150
GRB110625A	286.7510	6.7550	0.0132	24.000	2011-06-25	21:08:22.000	6.100e-005	-2.150
GRB110626A	131.9100	5.5600	7.6600	6.400	2011-06-26	10:44:54.213	1.160e-006	-2.150
GRB110629A	69.3700	25.0100	4.8200	61.700	2011-06-29	04:09:58.198	2.430e-006	-2.150
GRB110705B	122.9600	28.8000	3.0800	19.200	2011-07-05	08:43:43.418	8.940e-006	-2.150

Table A.1: List of the 468 long GRBs used in the presented analysis. A redshift of -2.150 indicates that the redshift of that GRB was not measured.

Name	RA(deg)	Decl(deg)	Err(deg)	T90(s)	Date	UT(Trigger)	F(Erg/cm^2)	Z
GRB110706A	100.0800	6.1400	8.0300	12.040	2011-07-06	04:51:04.029	3.270e-006	-2.150
GRB110706C	9.0600	31.7300	4.1100	16.890	2011-07-06	17:27:56.345	2.340e-006	-2.150
GRB110706D	347.4700	7.1100	2.5800	33.220	2011-07-06	23:26:51.412	6.550e-006	-2.150
GRB110708A	340.1210	53.9600	0.0162	50.000	2011-07-08	04:43:22.000	2.000e-006	-2.150
GRB110709A	238.8910	40.9240	0.0003	44.700	2011-07-09	15:24:29.000	3.700e-005	-2.150
GRB110709C	155.3800	23.1200	1.5300	24.060	2011-07-09	11:06:53.366	6.910e-006	-2.150
GRB110710A	229.0900	48.4000	3.8700	22.720	2011-07-10	22:53:50.597	9.320e-006	-2.150
GRB110719A	24.5810	34.5860	0.0004	41.000	2011-07-19	06:09:11.000	1.800e-006	-2.150
GRB110722A	215.0600	5.0000	1.9900	73.470	2011-07-22	16:39:16.676	2.110e-005	-2.150
GRB110722B	8.2800	62.7400	4.6600	14.340	2011-07-22	17:01:45.914	1.800e-006	-2.150
GRB110726A	286.7170	56.0710	0.0001	5.200	2011-07-26	01:30:40.000	2.200e-007	1.036
GRB110726B	317.7100	2.4700	3.8200	29.950	2011-07-26	05:03:59.487	4.360e-006	-2.150
GRB110729A	353.3900	4.9700	1.3600	408.580	2011-07-29	03:25:05.929	4.640e-005	-2.150
GRB110801A	89.4370	80.9560	0.0001	385.000	2011-08-01	19:49:42.000	7.300e-006	1.858
GRB110806A	112.0400	2.3800	2.4200	28.410	2011-08-06	22:25:31.115	7.190e-006	-2.150
GRB110812A	358.4090	72.2060	0.0304	30.000	2011-08-12	00:20:08.000	-1.000e-005	-2.150
GRB110812B	77.7600	1.7100	2.4900	11.260	2011-08-12	21:35:08.607	1.170e-006	-2.150
GRB110813A	61.2400	34.5600	1.0000	22.780	2011-08-13	05:40:50.931	4.770e-006	-2.150
GRB110815A	85.2970	32.4420	0.1137	20.000	2011-08-15	09:40:55.971	5.000e-005	-2.150
GRB110820A	343.1920	70.2980	0.0004	256.000	2011-08-20	17:38:27.000	8.200e-007	-2.150
GRB110820C	90.5100	21.6300	3.9600	11.270	2011-08-20	11:25:44.348	7.980e-007	-2.150
GRB110824A	152.0500	1.3200	1.6800	76.610	2011-08-24	00:13:09.941	1.490e-005	-2.150
GRB110825A	44.8960	15.4000	0.3437	6.900	2011-08-25	02:27:03.000	5.450e-005	-2.150
GRB110827A	164.0590	53.8170	0.0223	8.500	2011-08-27	00:01:52.000	1.800e-007	-2.150
GRB110831A	352.3500	33.6600	5.8600	98.880	2011-08-31	06:45:26.606	4.420e-006	-2.150
GRB110903A	197.0610	58.9850	0.0203	370.000	2011-09-03	02:39:33.115	4.200e-005	-2.150
GRB110903B	164.2100	42.0800	1.1800	28.670	2011-09-03	00:13:06.293	1.520e-005	-2.150
GRB110904A	359.6900	35.9000	2.6300	83.910	2011-09-04	02:58:15.961	1.110e-005	-2.150
GRB110904C	323.7400	23.9400	1.6800	20.480	2011-09-04	12:44:19.330	3.810e-006	-2.150
GRB110906B	26.3200	17.6500	4.0300	23.940	2011-09-06	07:15:13.419	3.800e-006	-2.150
GRB110915B	77.5480	1.9250	0.0405	18.000	2011-09-15	18:24:19.000	-1.000e-005	-2.150
GRB110919A	279.9700	66.4300	1.0000	35.070	2011-09-19	15:12:15.784	2.680e-005	-2.150
GRB110920A	87.5700	38.7600	5.0000	9.730	2011-09-20	08:07:16.410	2.690e-006	-2.150
GRB110921A	294.0980	36.3290	0.0003	48.000	2011-09-21	13:51:20.000	4.200e-006	-2.150
GRB110926A	69.4400	10.4300	3.2700	75.270	2011-09-26	02:33:36.644	1.200e-005	-2.150
GRB110928A	257.7330	36.5360	0.0004	26.700	2011-09-28	01:51:31.000	6.900e-007	-2.150
GRB110928B	153.4000	34.2900	1.4200	148.230	2011-09-28	04:19:51.410	1.420e-005	-2.150
GRB111005B	340.3000	75.8000	5.2800	30.720	2011-10-05	09:33:03.376	2.060e-006	-2.150
GRB111010A	87.0900	43.9800	3.1800	82.430	2011-10-10	05:40:34.564	1.100e-005	-2.150
GRB111010C	69.8000	41.8800	1.6700	52.990	2011-10-10	17:00:35.288	1.260e-005	-2.150
GRB111012A	154.0100	68.0900	2.0800	20.740	2011-10-12	10:56:37.442	1.650e-005	-2.150
GRB111012B	97.2200	67.0500	1.7100	7.930	2011-10-12	19:27:39.098	3.290e-006	-2.150
GRB111016A	153.8340	27.4620	0.0003	550.000	2011-10-16	18:37:04.000	4.000e-006	-2.150
GRB111018B	106.0800	66.1400	7.1500	8.190	2011-10-18	14:16:48.868	1.110e-006	-2.150

Table A.1: List of the 468 long GRBs used in the presented analysis. A redshift of -2.150 indicates that the redshift of that GRB was not measured.

Name	RA(deg)	Decl(deg)	Err(deg)	T90(s)	Date	UT(Trigger)	F(Erg/cm^2)	Z
GRB111018C	124.1800	81.2900	7.4600	29.700	2011-10-18	18:50:14.710	1.760e-006	-2.150
GRB111022B	108.9650	49.6840	0.0003	101.640	2011-10-22	17:13:04.000	9.000e-007	-2.150
GRB111029A	44.7840	57.1110	0.0004	7.600	2011-10-29	09:44:40.000	3.900e-007	-2.150
GRB111103B	265.6930	1.6100	0.0003	167.000	2011-11-03	10:59:03.000	2.000e-005	-2.150
GRB111105A	153.4800	7.2800	14.2400	43.520	2011-11-05	10:57:36.083	1.680e-006	-2.150
GRB111109C	129.9800	44.6500	1.5000	9.670	2011-11-09	20:57:16.657	6.690e-006	-2.150
GRB111124A	94.0600	4.6300	9.4200	8.960	2011-11-24	07:24:10.086	6.260e-007	-2.150
GRB111127A	103.7000	3.5000	2.0900	19.010	2011-11-27	19:27:01.698	8.640e-006	-2.150
GRB111201A	190.4850	32.9940	0.0213	16.890	2011-12-01	14:22:45.260	1.000e-006	-2.150
GRB111203A	53.2200	33.4700	3.2300	55.550	2011-12-03	01:17:04.034	4.650e-006	-2.150
GRB111208A	290.2150	40.6690	0.0223	40.960	2011-12-08	08:28:10.789	1.000e-006	-2.150
GRB111211A	153.0910	11.1820	0.0304	25.000	2011-12-11	22:17:33.000	9.200e-006	0.478
GRB111215A	349.5550	32.4940	0.0002	796.000	2011-12-15	14:04:08.000	4.500e-006	-2.150
GRB111215B	222.4030	16.4390	0.0767	75.000	2011-12-15	20:28:02.720	5.300e-005	-2.150
GRB111216A	185.9900	5.8300	1.3700	83.780	2011-12-16	09:20:31.510	4.170e-005	-2.150
GRB111225A	13.1550	51.5720	0.0001	106.800	2011-12-25	03:50:37.000	1.300e-006	0.297
GRB111226A	21.5000	3.8700	1.0000	74.750	2011-12-26	19:04:58.285	1.150e-005	-2.150
GRB111228A	150.0670	18.2980	0.0002	101.200	2011-12-28	15:44:43.000	1.800e-005	0.714
GRB111228B	330.6500	14.4700	3.5700	2.940	2011-12-28	10:52:50.520	2.750e-006	-2.150
GRB111230A	150.1900	33.4300	2.7800	28.160	2011-12-30	16:23:08.604	2.900e-006	-2.150
GRB120105A	203.6900	40.0700	2.8000	22.530	2012-01-05	14:00:35.901	1.470e-006	-2.150
GRB120106A	66.1080	64.0380	0.0002	61.600	2012-01-06	14:16:24.000	9.700e-007	-2.150
GRB120109A	251.3300	30.8000	11.3300	38.660	2012-01-09	19:46:01.942	1.920e-006	-2.150
GRB120111A	95.3400	5.0000	5.3800	76.800	2012-01-11	01:13:27.628	3.970e-006	-2.150
GRB120114A	317.9040	57.0360	0.0233	43.270	2012-01-14	16:20:05.680	-1.000e-005	-2.150
GRB120116A	16.2410	33.9310	0.0003	41.000	2012-01-16	18:06:28.000	2.900e-006	-2.150
GRB120118C	166.5700	47.8700	7.1700	17.150	2012-01-18	21:32:45.806	1.620e-006	-2.150
GRB120120A	134.7200	35.4700	5.7100	32.260	2012-01-20	10:21:25.415	1.500e-006	-2.150
GRB120129A	30.4400	59.2820	3.8260	3.070	2012-01-29	13:55:46.244	2.700e-005	-2.150
GRB120130B	64.9600	9.4800	5.5500	3.580	2012-01-30	21:44:54.331	5.250e-007	-2.150
GRB120130C	323.3000	58.5600	1.0000	38.910	2012-01-30	22:30:34.465	1.040e-005	-2.150
GRB120202A	203.5070	22.7750	0.0253	100.000	2012-02-02	21:40:17.000	7.000e-007	-2.150
GRB120206A	73.4500	58.4100	2.2500	9.480	2012-02-06	22:46:16.685	5.880e-006	-2.150
GRB120213A	301.0120	65.4110	0.0004	48.900	2012-02-13	00:27:19.000	1.900e-006	-2.150
GRB120213B	183.4900	5.7600	4.2000	13.820	2012-02-13	14:32:44.609	2.680e-006	-2.150
GRB120217A	122.4400	36.7700	3.2300	5.890	2012-02-17	19:23:50.572	1.750e-006	-2.150
GRB120217B	298.7300	32.7000	1.5000	2.620	2012-02-17	21:41:57.768	4.860e-006	-2.150
GRB120219A	129.7900	51.0320	0.0003	90.500	2012-02-19	14:30:08.000	5.400e-007	-2.150
GRB120224B	118.4200	41.3400	4.6000	60.930	2012-02-24	06:46:28.523	9.120e-006	-2.150
GRB120224C	331.0600	10.1800	3.5900	29.180	2012-02-24	21:33:07.385	2.600e-006	-2.150
GRB120226A	300.0500	48.8100	0.5000	80.000	2012-02-26	20:54:19.724	7.500e-005	-2.150
GRB120226B	87.5900	52.3500	1.1500	14.590	2012-02-26	10:44:16.385	5.850e-006	-2.150
GRB120227A	84.7600	8.5000	6.3300	19.710	2012-02-27	09:22:45.971	3.740e-006	-2.150
GRB120308A	219.0850	79.6870	0.0003	60.600	2012-03-08	06:13:38.000	1.200e-006	-2.150

Table A.1: List of the 468 long GRBs used in the presented analysis. A redshift of -2.150 indicates that the redshift of that GRB was not measured.

Name	RA(deg)	Decl(deg)	Err(deg)	T90(s)	Date	UT(Trigger)	F(Erg/cm^2)	Z
GRB120308B	30.7500	55.2200	1.1900	25.600	2012-03-08	14:06:05.773	6.720e-006	-2.150
GRB120311A	273.0920	14.2960	0.0004	3.500	2012-03-11	05:33:38.000	3.000e-007	-2.150
GRB120312A	251.8120	23.8810	0.0213	14.200	2012-03-12	16:06:28.000	5.700e-007	-2.150
GRB120320A	212.5180	8.6960	0.0004	25.740	2012-03-20	11:56:15.000	5.900e-007	-2.150
GRB120324A	291.0790	24.1300	0.0003	118.000	2012-03-24	05:59:11.000	4.500e-005	-2.150
GRB120326A	273.9050	69.2600	0.0003	69.600	2012-03-26	01:20:29.000	3.540e-006	1.798
GRB120328B	229.0380	25.2990	1.0770	29.700	2012-03-28	06:26:20.953	7.740e-005	-2.150
GRB120404A	235.0100	12.8850	0.0003	38.700	2012-04-04	12:51:02.000	1.600e-006	1.633
GRB120412B	38.9100	7.0600	2.8000	101.190	2012-04-12	22:04:40.564	7.030e-006	-2.150
GRB120415A	213.5400	16.7300	4.3600	12.540	2012-04-15	01:49:57.682	2.230e-006	-2.150
GRB120415C	150.4600	61.2700	4.9600	12.540	2012-04-15	22:59:19.133	2.310e-006	-2.150
GRB120420B	109.2600	10.7600	1.1100	254.920	2012-04-20	20:35:13.070	4.330e-005	-2.150
GRB120422A	136.9100	14.0180	0.0003	5.350	2012-04-22	07:12:03.000	2.300e-007	0.280
GRB120430A	47.2500	18.5200	5.7500	14.590	2012-04-30	23:30:43.349	5.560e-007	-2.150
GRB120504A	329.9400	46.8300	4.0600	41.980	2012-05-04	11:13:39.935	3.360e-006	-2.150
GRB120510A	44.0470	72.8870	0.0008	130.000	2012-05-10	08:47:44.000	3.820e-006	-2.150
GRB120512A	325.5580	13.6360	0.0101	40.000	2012-05-12	02:41:40.000	9.330e-006	-2.150
GRB120520A	45.8600	35.2800	8.3000	5.760	2012-05-20	22:46:24.663	4.410e-007	-2.150
GRB120521C	214.2860	42.1450	0.0003	26.700	2012-05-21	23:22:07.000	1.100e-006	6.000
GRB120522B	56.0700	54.8500	2.0200	28.160	2012-05-22	08:39:16.839	9.320e-006	-2.150
GRB120528A	295.1300	6.5000	5.9800	16.390	2012-05-28	10:36:00.217	3.790e-006	-2.150
GRB120530A	175.9600	78.8300	3.2700	77.060	2012-05-30	02:53:41.862	7.170e-006	-2.150
GRB120531A	290.4000	1.2200	11.0300	25.350	2012-05-31	09:26:38.365	9.100e-007	-2.150
GRB120605A	243.6100	41.5100	2.6200	18.110	2012-06-05	10:52:15.904	3.250e-006	-2.150
GRB120608B	313.2600	12.6400	5.0800	24.840	2012-06-08	18:38:33.035	3.170e-006	-2.150
GRB120612B	211.8800	34.5600	7.0800	63.240	2012-06-12	16:19:45.548	2.060e-006	-2.150
GRB120618A	77.3100	75.8500	2.5900	17.600	2012-06-18	03:03:49.875	5.580e-006	-2.150
GRB120624B	170.8860	8.9330	0.0101	274.000	2012-06-24	22:19:30.985	1.920e-004	-2.150
GRB120625A	51.2600	51.0700	1.1700	7.430	2012-06-25	02:50:46.037	1.020e-005	-2.150
GRB120703B	69.4900	34.7400	2.6000	64.510	2012-07-03	10:01:11.688	1.110e-005	-2.150
GRB120703C	210.5100	46.2600	5.1500	77.570	2012-07-03	11:56:56.870	2.600e-006	-2.150
GRB120711B	331.7100	59.9960	0.0324	60.000	2012-07-11	03:11:02.580	5.600e-007	-2.150
GRB120715A	272.1500	58.7900	3.7300	29.690	2012-07-15	01:35:15.573	2.200e-006	-2.150
GRB120716A	313.0890	9.5580	0.1747	234.490	2012-07-16	17:05:03.908	1.470e-005	2.480
GRB120716B	304.5300	59.4100	5.0900	24.960	2012-07-16	13:51:02.134	5.220e-006	-2.150
GRB120722A	230.4970	13.2510	0.0004	42.400	2012-07-22	12:53:26.000	1.200e-006	0.959
GRB120724A	245.1800	3.5080	0.0003	72.800	2012-07-24	06:39:02.000	6.800e-007	1.480
GRB120727B	37.7600	16.3600	1.0000	10.490	2012-07-27	16:20:19.529	9.240e-006	-2.150
GRB120729A	13.0740	49.9400	0.0003	71.500	2012-07-29	10:56:14.000	5.100e-006	0.800
GRB120802A	44.8420	13.7680	0.0005	50.000	2012-08-02	08:00:51.000	1.900e-006	3.796
GRB120803B	314.2360	53.3040	0.0003	37.500	2012-08-03	11:06:06.000	2.500e-006	-2.150
GRB120805A	216.5380	5.8250	0.0005	48.000	2012-08-05	21:28:09.000	8.200e-007	-2.150
GRB120806A	308.9900	6.3300	4.2500	26.630	2012-08-06	00:10:08.866	4.900e-006	-2.150
GRB120811C	199.6830	62.3010	0.0003	26.800	2012-08-11	15:34:52.000	3.000e-006	2.671

Table A.1: List of the 468 long GRBs used in the presented analysis. A redshift of -2.150 indicates that the redshift of that GRB was not measured.

Name	RA(deg)	Decl(deg)	Err(deg)	T90(s)	Date	UT(Trigger)	F(Erg/cm^2)	Z
GRB120819B	171.5400	49.4200	7.9400	66.300	2012-08-19	01:08:26.765	1.330e-006	-2.150
GRB120824A	70.9200	17.6300	3.0000	111.620	2012-08-24	14:16:00.734	5.920e-006	-2.150
GRB120830C	110.0300	17.5300	3.3900	49.670	2012-08-30	16:51:36.680	5.660e-006	-2.150
GRB120905A	355.9600	16.9900	1.8000	195.590	2012-09-05	15:46:21.166	1.960e-005	-2.150
GRB120911A	357.9790	63.0990	0.0003	22.020	2012-09-11	07:08:33.988	2.340e-006	-2.150
GRB120913A	146.4000	26.9590	0.0122	40.960	2012-09-13	20:18:22.887	3.800e-009	-2.150
GRB120914A	267.9400	1.8200	5.3500	10.240	2012-09-14	03:26:42.114	7.350e-007	-2.150
GRB120916A	205.6310	36.7000	0.4953	26.000	2012-09-16	04:07:46.689	1.950e-005	-2.150
GRB120923A	303.7950	6.2210	0.0003	27.200	2012-09-23	05:16:06.000	3.200e-007	-2.150
GRB120926A	318.3900	58.3800	1.5100	4.290	2012-09-26	08:02:56.573	2.480e-006	-2.150
GRB121005B	149.7300	25.4000	5.3900	141.570	2012-10-05	08:09:12.865	5.170e-006	-2.150
GRB121011A	260.2150	41.1100	0.0004	31.000	2012-10-11	11:15:30.264	1.000e-005	0.580
GRB121019A	43.4700	62.1400	7.5200	14.340	2012-10-19	05:35:09.226	5.890e-007	-2.150
GRB121102B	258.4700	14.0900	12.1500	2.050	2012-11-02	01:32:47.937	5.670e-007	-2.150
GRB121104A	72.1400	14.0800	4.0500	59.130	2012-11-04	15:02:15.495	4.450e-006	-2.150
GRB121108A	83.1940	54.4740	0.0003	89.000	2012-11-08	17:47:39.000	9.600e-007	-2.150
GRB121113A	313.1700	59.8200	2.0600	95.490	2012-11-13	13:02:43.531	2.690e-005	-2.150
GRB121117B	279.1400	44.9300	4.3200	331.780	2012-11-17	00:25:37.726	1.060e-005	-2.150
GRB121118A	299.3790	65.6540	1.1443	33.800	2012-11-18	13:48:54.256	6.780e-006	-2.150
GRB121122A	35.2620	45.1390	3.7097	8.190	2012-11-22	21:14:52.546	5.460e-005	-2.150
GRB121122B	52.6700	46.4700	12.8900	8.700	2012-11-22	13:31:27.521	8.150e-007	-2.150
GRB121122C	355.4500	6.3400	2.6600	125.440	2012-11-22	20:52:49.028	9.070e-006	-2.150
GRB121125A	228.5280	55.3130	0.0003	52.200	2012-11-25	08:32:27.000	9.500e-006	-2.150
GRB121125B	177.5300	38.5400	5.2400	12.860	2012-11-25	11:14:47.490	8.570e-007	-2.150
GRB121202A	256.7970	23.9480	0.0002	20.100	2012-12-02	04:20:05.000	2.000e-006	-2.150
GRB121210A	202.5400	17.7700	8.2500	12.800	2012-12-10	01:56:01.527	2.020e-006	-2.150
GRB121211B	72.3700	8.6300	5.2300	8.960	2012-12-11	16:41:02.769	1.340e-006	-2.150
GRB121212A	177.7920	78.0370	0.0003	10.000	2012-12-12	06:56:12.000	1.200e-007	-2.150
GRB121220A	31.0700	48.2800	8.3000	5.120	2012-12-20	07:28:13.239	4.530e-007	-2.150
GRB121221A	214.2600	33.5500	4.2200	38.910	2012-12-21	21:59:29.970	5.040e-006	-2.150
GRB121223A	50.1100	21.3700	2.7400	11.010	2012-12-23	07:11:19.812	7.020e-006	-2.150
GRB130102A	311.4230	49.8180	0.0003	77.500	2013-01-02	18:10:53.000	7.200e-007	-2.150
GRB130104A	174.0900	25.9200	2.4400	26.370	2013-01-04	17:18:07.049	5.670e-006	-2.150
GRB130106B	28.7600	63.3800	1.8700	70.400	2013-01-06	23:52:25.792	1.540e-005	-2.150
GRB130109A	17.4500	19.2400	3.7200	8.960	2013-01-09	04:56:26.261	2.540e-006	-2.150
GRB130112A	236.0300	52.1900	4.9300	35.330	2013-01-12	06:52:07.524	2.610e-006	-2.150
GRB130115A	171.0900	22.6200	2.7800	13.570	2013-01-15	17:10:39.182	2.720e-006	-2.150
GRB130117A	341.2400	2.8100	6.1700	78.850	2013-01-17	02:05:11.425	2.850e-006	-2.150
GRB130118A	278.3000	40.9800	6.7000	21.570	2013-01-18	11:33:29.360	8.280e-007	-2.150
GRB130122A	194.2850	59.0150	0.0003	64.000	2013-01-22	23:44:09.000	7.400e-007	-2.150
GRB130131A	171.1260	48.0760	0.0003	51.600	2013-01-31	13:56:22.000	3.100e-007	-2.150
GRB130131B	173.9560	15.0380	0.0003	4.300	2013-01-31	19:10:08.000	3.400e-007	2.539
GRB130208A	181.6000	50.9300	4.6700	41.470	2013-02-08	16:24:23.836	2.260e-006	-2.150
GRB130215A	43.4860	13.3870	0.0152	46.000	2013-02-15	01:31:25.437	2.020e-005	0.597

Table A.1: List of the 468 long GRBs used in the presented analysis. A redshift of -2.150 indicates that the redshift of that GRB was not measured.

Name	RA(deg)	Decl(deg)	Err(deg)	T90(s)	Date	UT(Trigger)	F(Erg/cm^2)	Z
GRB130215B	3.1100	59.3800	2.1000	58.110	2013-02-15	15:34:16.190	2.150e-005	-2.150
GRB130216A	67.9010	14.6700	0.0101	6.500	2013-02-16	22:15:24.000	6.230e-006	-2.150
GRB130216B	58.8660	2.0360	0.0152	15.290	2013-02-16	18:58:11.695	4.800e-006	-2.150
GRB130217A	96.7200	6.8000	8.1900	14.840	2013-02-17	16:31:19.119	1.100e-006	-2.150
GRB130219A	303.7300	40.8300	1.2100	96.000	2013-02-19	18:35:51.730	3.180e-005	-2.150
GRB130220A	306.2000	31.7400	1.1400	6.400	2013-02-20	23:08:48.202	7.240e-006	-2.150
GRB130224A	205.9000	59.7200	2.6200	70.910	2013-02-24	08:53:02.377	4.960e-006	-2.150
GRB130228A	265.8300	55.9300	0.5000	111.750	2013-02-28	02:40:02.166	1.240e-005	-2.150
GRB130304A	98.9300	53.5700	1.2000	67.840	2013-03-04	09:49:53.099	3.700e-005	-2.150
GRB130305A	116.7740	52.0370	0.0182	25.600	2013-03-05	11:39:11.369	5.700e-005	-2.150
GRB130307B	319.5200	10.7700	4.4200	63.490	2013-03-07	05:42:19.325	3.970e-006	-2.150
GRB130314A	206.2100	46.7700	1.4100	142.850	2013-03-14	03:31:16.299	1.460e-005	-2.150
GRB130318A	200.7400	8.1200	9.9400	137.990	2013-03-18	10:56:31.179	3.410e-006	-2.150
GRB130324A	255.4300	0.0500	6.0300	37.760	2013-03-24	01:00:24.747	1.900e-006	-2.150
GRB130327A	92.0390	55.7150	0.0003	9.000	2013-03-27	01:47:34.000	2.300e-007	-2.150
GRB130331A	164.4700	29.6400	2.4300	13.820	2013-03-31	13:35:44.870	9.330e-006	-2.150
GRB130404A	30.7500	1.5400	7.2400	3.330	2013-04-04	10:15:40.052	8.430e-007	-2.150
GRB130406C	138.2100	42.8300	14.8400	2.560	2013-04-06	08:29:36.580	2.980e-007	-2.150
GRB130407B	53.5300	44.1700	9.2900	32.000	2013-04-07	19:12:43.057	1.750e-006	-2.150
GRB130408B	118.7700	66.3400	3.9300	9.210	2013-04-08	15:40:22.855	2.050e-006	-2.150
GRB130409A	30.5200	44.1000	2.2200	26.110	2013-04-09	23:01:59.658	7.870e-006	-2.150
GRB130416A	99.2800	24.7000	14.3400	3.080	2013-04-16	16:34:07.062	2.810e-007	-2.150
GRB130418A	149.0370	13.6670	0.0003	300.000	2013-04-18	19:00:53.000	1.800e-006	1.218
GRB130419A	355.2780	9.9000	0.0263	75.700	2013-04-19	13:30:29.000	7.800e-007	-2.150
GRB130420A	196.1060	59.4240	0.0003	123.500	2013-04-20	07:28:29.000	1.400e-005	1.297
GRB130420B	183.1280	54.3910	0.0003	13.830	2013-04-20	12:56:32.988	1.040e-007	-2.150
GRB130427A	173.1360	27.6980	0.0006	162.830	2013-04-27	07:47:57.000	1.980e-003	0.340
GRB130502B	66.6480	71.0840	0.0930	27.392	2013-05-02	07:51:12.763	1.210e-004	-2.150
GRB130504C	91.7150	3.8460	0.1550	67.000	2013-05-04	23:29:00.540	1.340e-004	-2.150
GRB130505A	137.0610	17.4850	0.0003	14.000	2013-05-05	08:22:24.527	3.130e-004	2.270
GRB130508A	305.3510	34.9660	0.0223	42.000	2013-05-08	17:08:53.000	6.600e-007	-2.150
GRB130511A	196.6450	18.7100	0.0003	5.430	2013-05-11	11:30:47.000	2.200e-007	1.303
GRB130515C	146.7700	11.2600	10.5000	2.560	2013-05-15	18:06:51.391	6.800e-007	-2.150
GRB130517A	41.8600	42.6600	1.5000	32.520	2013-05-17	18:44:12.981	1.870e-005	-2.150
GRB130518A	355.6710	47.4780	0.0294	22.000	2013-05-18	13:54:50.000	9.300e-005	2.490
GRB130521A	87.5680	14.4700	0.0162	11.000	2013-05-21	22:49:16.000	4.200e-007	-2.150
GRB130521B	281.6410	22.7230	0.1207	23.000	2013-05-21	21:24:31.599	1.900e-005	-2.150
GRB130522A	134.1500	17.6200	4.9000	27.900	2013-05-22	12:14:31.135	3.990e-006	-2.150
GRB130528A	139.5010	87.3010	0.0003	59.400	2013-05-28	16:41:23.000	8.000e-006	-2.150
GRB130528B	352.7000	27.8100	5.5000	66.300	2013-05-28	12:04:31.329	3.340e-006	-2.150
GRB130530A	160.9500	25.2300	1.0400	58.620	2013-05-30	17:15:23.006	6.330e-006	-2.150
GRB130603A	86.8970	82.9090	0.0003	76.000	2013-06-03	05:59:32.000	1.900e-006	-2.150
GRB130604A	250.1880	68.2270	0.0004	37.700	2013-06-04	06:54:26.000	1.400e-006	-2.150
GRB130606A	249.3960	29.7960	0.0003	276.580	2013-06-06	21:04:39.000	4.400e-006	5.910

Table A.1: List of the 468 long GRBs used in the presented analysis. A redshift of -2.150 indicates that the redshift of that GRB was not measured.

Name	RA(deg)	Decl(deg)	Err(deg)	T90(s)	Date	UT(Trigger)	F(Erg/cm^2)	Z
GRB130606C	339.3700	12.4900	1.6700	24.130	2013-06-06	07:35:30.405	9.360e-006	-2.150
GRB130608A	24.6110	41.5030	0.0003	44.400	2013-06-08	23:14:21.000	9.000e-007	-2.150
GRB130609A	152.6690	24.1320	0.0004	7.000	2013-06-09	03:05:08.000	7.700e-007	-2.150
GRB130610A	224.4200	28.2070	0.0001	46.400	2013-06-10	03:12:13.000	6.100e-006	-2.150
GRB130612A	259.7940	16.7200	0.0003	7.420	2013-06-12	03:22:23.361	5.700e-007	2.006
GRB130612B	247.9400	31.0200	1.7900	10.240	2013-06-12	10:57:14.628	8.330e-006	-2.150
GRB130615B	184.8600	69.6200	6.2000	21.760	2013-06-15	09:33:07.462	2.740e-006	-2.150
GRB130620A	74.4200	61.1900	12.2700	14.590	2013-06-20	11:57:06.927	1.180e-006	-2.150
GRB130623B	194.6100	35.5100	7.2000	29.440	2013-06-23	03:06:37.123	9.450e-007	-2.150
GRB130623C	203.5900	49.0300	7.1200	44.550	2013-06-23	09:30:24.065	1.070e-006	-2.150
GRB130623E	107.4300	36.0400	4.6300	42.240	2013-06-23	18:57:50.985	8.690e-006	-2.150
GRB130624A	337.3200	11.4500	6.9000	95.230	2013-06-24	02:13:56.084	1.150e-006	-2.150
GRB130625A	343.2780	82.1740	0.0004	38.100	2013-06-25	07:00:39.000	1.800e-006	-2.150
GRB130626B	24.8900	4.9300	4.0300	28.160	2013-06-26	14:17:32.492	4.820e-006	-2.150
GRB130630A	170.0100	60.0600	1.0000	17.150	2013-06-30	06:31:19.699	1.650e-005	-2.150
GRB130701A	357.2290	36.1010	0.0003	4.380	2013-07-01	04:17:43.000	5.800e-006	1.155
GRB130702A	216.4000	15.8000	0.5000	26.000	2013-07-02	00:05:23.000	5.720e-006	0.145
GRB130702B	292.1600	10.3900	12.9500	16.390	2013-07-02	22:48:59.526	7.530e-007	-2.150
GRB130716B	348.8700	45.3400	6.2700	91.140	2013-07-16	08:26:19.203	2.990e-006	-2.150
GRB130720A	243.5000	14.9700	6.5800	48.640	2013-07-20	02:46:40.720	4.240e-006	-2.150
GRB130725A	230.0600	0.6240	0.0253	101.800	2013-07-25	11:37:11.000	9.700e-007	-2.150
GRB130725C	42.4500	64.8200	2.2700	6.650	2013-07-25	12:38:40.770	5.180e-006	-2.150
GRB130806A	35.9290	67.5320	0.0004	6.100	2013-08-06	02:51:33.000	1.700e-007	-2.150
GRB130813A	204.0300	56.3400	10.4700	11.260	2013-08-13	18:59:22.758	1.230e-006	-2.150
GRB130815A	164.7100	49.5700	1.6000	236.290	2013-08-15	10:05:07.886	4.590e-005	-2.150
GRB130818A	192.2900	57.5800	2.2300	25.350	2013-08-18	22:34:33.785	3.530e-006	-2.150
GRB130828A	259.8300	28.0000	0.3000	136.450	2013-08-28	07:20:00.153	6.050e-005	-2.150
GRB130828B	188.2500	27.8900	2.4300	3.910	2013-08-28	19:23:54.001	2.780e-006	-2.150
GRB130829A	182.4260	46.5200	0.0132	42.560	2013-08-29	05:43:33.000	1.200e-006	-2.150
GRB130829B	258.5100	6.0000	1.6900	6.660	2013-08-29	16:08:01.073	3.680e-006	-2.150
GRB130831A	358.6250	29.4300	0.0003	32.500	2013-08-31	13:04:16.000	7.600e-006	0.479
GRB130831C	267.4500	61.0300	8.0600	24.830	2013-08-31	01:24:13.793	2.130e-006	-2.150
GRB130906A	194.1100	4.2000	12.3900	11.260	2013-09-06	05:19:30.538	6.270e-007	-2.150
GRB130907A	215.8920	45.6070	0.0002	206.080	2013-09-07	21:39:15.997	7.900e-004	1.238
GRB130913A	341.9600	1.2940	0.0507	10.000	2013-09-13	00:28:21.000	1.300e-007	-2.150
GRB130919C	59.8000	48.5200	5.7200	80.900	2013-09-19	08:27:04.735	4.680e-006	-2.150
GRB130925B	83.4300	55.3000	4.1200	265.470	2013-09-25	13:05:43.127	1.490e-005	-2.150
GRB131002A	253.2210	82.0540	0.0003	55.040	2013-10-02	06:55:06.994	1.400e-006	-2.150
GRB131014B	15.0500	21.4300	6.9400	30.210	2013-10-14	12:18:36.157	1.950e-006	-2.150
GRB131018B	304.4100	23.1100	0.1300	39.930	2013-10-18	16:08:39.181	2.730e-006	-2.150
GRB131024B	144.5030	44.2720	0.0005	64.000	2013-10-24	21:35:31.000	4.260e-006	-2.150
GRB131028A	61.2250	71.5950	2.7067	17.150	2013-10-28	01:49:02.346	1.620e-004	-2.150
GRB131029A	200.7850	48.2980	0.2600	84.000	2013-10-29	23:20:48.000	3.000e-005	-2.150
GRB131108A	156.4000	9.9000	0.5000	23.040	2013-11-08	20:41:52.947	3.650e-005	2.400

Table A.1: List of the 468 long GRBs used in the presented analysis. A redshift of -2.150 indicates that the redshift of that GRB was not measured.

Name	RA(deg)	Decl(deg)	Err(deg)	T90(s)	Date	UT(Trigger)	F(Erg/cm^2)	Z
GRB131108B	353.6000	33.8800	4.7000	14.590	2013-11-08	00:34:42.828	2.820e-006	-2.150
GRB131110B	9.8100	8.1600	3.9600	27.320	2013-11-10	08:57:01.343	3.270e-006	-2.150
GRB131122A	152.5550	57.7400	0.0162	70.000	2013-11-22	21:25:01.000	2.000e-006	-2.150
GRB131122B	261.6700	33.3800	1.6900	23.040	2013-11-22	11:45:05.397	2.830e-005	-2.150
GRB131125A	114.6750	48.4140	0.9113	2.810	2013-11-25	16:32:51.048	5.530e-007	-2.150
GRB131127A	332.7300	36.6090	0.0003	92.100	2013-11-27	10:11:35.000	1.900e-006	-2.150
GRB131127D	246.3000	33.9200	8.6600	15.100	2013-11-27	16:41:46.343	1.220e-006	-2.150
GRB131128A	355.3080	31.3060	0.0003	3.000	2013-11-28	15:06:24.000	4.400e-007	-2.150
GRB131202B	169.6600	21.2500	2.2400	86.020	2013-12-02	21:45:20.420	1.240e-005	-2.150
GRB131209B	253.8800	72.6000	6.1400	4.090	2013-12-09	23:06:16.406	6.570e-007	-2.150
GRB131215A	258.6540	7.8620	0.0608	300.000	2013-12-15	09:08:20.000	1.400e-005	-2.150
GRB131215B	104.0700	68.2600	1.3800	23.040	2013-12-15	07:08:45.197	8.050e-006	-2.150
GRB131217B	227.7300	25.1600	3.1200	9.210	2013-12-17	04:23:28.060	5.750e-006	-2.150
GRB131227A	67.3780	28.8830	0.0003	18.000	2013-12-27	04:44:51.000	8.400e-007	-2.150
GRB131230A	91.1100	64.2900	11.0700	3.070	2013-12-30	12:41:27.116	5.910e-007	-2.150
GRB140102A	211.9190	1.3330	0.0003	10.496	2014-01-02	21:17:36.245	2.000e-005	-2.150
GRB140103A	232.1140	37.7520	0.0172	17.300	2014-01-03	00:30:43.000	6.000e-007	-2.150
GRB140108A	325.1120	58.7450	0.0004	97.800	2014-01-08	17:18:42.000	1.910e-005	0.600
GRB140110C	31.8600	65.1600	3.1900	81.150	2014-01-10	19:31:34.447	8.320e-006	-2.150
GRB140112A	8.4400	11.9900	7.1400	12.030	2014-01-12	01:26:46.894	1.600e-006	-2.150
GRB140113B	329.3700	18.1300	12.2800	4.610	2014-01-13	14:58:25.793	5.700e-007	-2.150
GRB140114A	188.5220	27.9510	0.0003	139.700	2014-01-14	11:57:40.000	3.200e-006	-2.150
GRB140122A	56.0800	15.0900	5.2600	3.590	2014-01-22	14:19:47.783	9.050e-007	-2.150
GRB140126A	208.7000	31.2800	5.8400	75.780	2014-01-26	19:33:41.643	5.350e-006	-2.150
GRB140204A	166.1100	62.5300	5.6400	71.170	2014-02-04	13:07:02.560	2.350e-006	-2.150
GRB140206A	145.3350	66.7610	0.0002	93.600	2014-02-06	07:17:20.000	1.470e-005	2.730
GRB140209A	81.3280	32.4880	0.0101	21.300	2014-02-09	07:30:57.000	9.500e-006	-2.150
GRB140211A	124.2330	20.2370	0.0142	89.400	2014-02-11	12:23:03.000	1.800e-006	-2.150
GRB140215A	104.1490	41.7860	0.0003	84.200	2014-02-15	04:07:10.000	1.840e-005	-2.150
GRB140216A	194.0400	31.4600	13.7300	2.430	2014-02-16	07:56:04.592	9.740e-007	-2.150
GRB140217A	359.3900	76.7500	3.0800	41.480	2014-02-17	01:01:41.999	3.080e-006	-2.150
GRB140218A	347.4800	44.5400	3.6200	53.500	2014-02-18	10:14:29.328	5.610e-006	-2.150
GRB140219B	221.9300	50.0000	8.2300	6.080	2014-02-19	07:38:54.449	2.700e-006	-2.150
GRB140224A	2.7800	20.3700	5.9300	2.300	2014-02-24	09:10:17.167	6.590e-007	-2.150
GRB140224B	23.7400	39.4800	3.6900	17.150	2014-02-24	18:55:19.824	2.420e-006	-2.150
GRB140226A	221.4920	14.9940	0.0006	15.000	2014-02-26	10:02:57.000	5.600e-006	-2.150
GRB140227A	235.3100	31.5500	8.1900	17.150	2014-02-27	17:43:06.586	7.140e-007	-2.150
GRB140304A	30.6430	33.4740	0.0003	31.750	2014-03-04	13:22:31.482	2.600e-006	5.390
GRB140305A	344.4970	15.4480	0.0172	13.700	2014-03-05	15:00:20.000	4.700e-007	-2.150
GRB140306A	27.9430	48.9750	0.1647	54.000	2014-03-06	03:29:44.404	1.350e-004	-2.150
GRB140308B	350.1600	73.0300	2.6700	12.030	2014-03-08	17:02:38.673	6.440e-006	-2.150
GRB140311A	209.3050	0.6420	0.0003	71.400	2014-03-11	21:05:16.000	2.300e-006	4.950
GRB140311B	252.3250	52.7240	0.0003	72.190	2014-03-11	21:14:35.646	7.900e-006	-2.150
GRB140311C	183.6500	62.8100	3.3200	14.330	2014-03-11	14:49:13.096	4.600e-006	-2.150

Table A.1: List of the 468 long GRBs used in the presented analysis. A redshift of -2.150 indicates that the redshift of that GRB was not measured.

Name	RA(deg)	Decl(deg)	Err(deg)	T90(s)	Date	UT(Trigger)	F(Erg/cm^2)	Z
GRB140318A	184.0890	20.2090	0.0003	8.430	2014-03-18	00:09:07.000	2.900e-007	-2.150
GRB140319A	136.0100	81.5300	3.6400	50.370	2014-03-19	23:08:30.359	7.130e-006	-2.150
GRB140320B	145.5410	60.2790	0.0203	100.000	2014-03-20	09:26:00.000	5.000e-007	-2.150
GRB140320C	134.4180	71.2000	0.0304	30.000	2014-03-20	13:17:20.000	2.000e-007	-2.150
GRB140320D	87.8930	85.4290	3.7177	22.000	2014-03-20	20:21:38.309	2.100e-004	-2.150
GRB140328A	320.0400	17.9700	14.7000	4.160	2014-03-28	13:26:26.028	7.470e-007	-2.150
GRB140331A	134.8640	2.7170	0.0003	209.000	2014-03-31	05:49:48.000	6.700e-007	-2.150
GRB140404A	14.8900	78.8900	4.8800	84.990	2014-04-04	00:43:26.090	1.920e-006	-2.150
GRB140404B	172.7300	33.1800	2.1900	26.630	2014-04-04	04:06:47.514	8.180e-006	-2.150
GRB140406A	70.1000	13.5400	5.8600	37.120	2014-04-06	03:26:48.185	2.800e-006	-2.150
GRB140406B	357.5500	5.6300	2.6000	109.310	2014-04-06	02:52:13.758	1.150e-005	-2.150
GRB140414B	45.6800	13.8200	2.3000	25.600	2014-04-14	16:38:37.966	5.990e-006	-2.150
GRB140416A	40.1860	39.5270	4.1323	32.768	2014-04-16	01:26:36.209	7.200e-005	-2.150
GRB140419A	126.9900	46.2400	0.0003	94.700	2014-04-19	04:06:51.000	5.800e-005	3.956
GRB140423A	197.2850	49.8420	0.0002	134.000	2014-04-23	08:31:53.000	2.000e-005	3.260
GRB140428A	194.3650	28.3310	0.0223	17.420	2014-04-28	22:40:50.000	3.400e-007	4.700
GRB140429A	338.6000	34.8500	6.0900	9.220	2014-04-29	23:24:41.786	6.200e-007	-2.150
GRB140430A	102.9360	23.0240	0.0003	173.600	2014-04-30	20:33:36.000	1.100e-006	1.600
GRB140501B	62.7800	43.2500	2.7300	22.150	2014-05-01	11:55:10.490	6.970e-006	-2.150
GRB140502A	319.1880	48.9700	0.0003	16.900	2014-05-02	08:30:20.000	1.600e-006	-2.150
GRB140508A	255.6310	46.7470	0.2717	44.280	2014-05-08	03:03:54.598	6.240e-005	-2.150
GRB140508C	272.1000	72.5300	3.5600	50.440	2014-05-08	15:05:26.137	2.610e-006	-2.150
GRB140515A	186.0650	15.1050	0.0003	23.400	2014-05-15	09:12:36.000	5.900e-007	6.320
GRB140516B	115.1600	4.2900	7.7700	33.790	2014-05-16	16:47:38.662	2.280e-006	-2.150
GRB140516C	74.2800	32.8500	3.8100	22.010	2014-05-16	18:21:00.835	6.610e-006	-2.150
GRB140517A	127.7500	13.5700	2.1700	20.480	2014-05-17	19:31:17.692	4.480e-006	-2.150
GRB140518A	227.2310	42.3960	0.0182	60.500	2014-05-18	09:17:46.000	1.000e-006	4.707
GRB140519A	278.4700	34.4100	5.4300	47.610	2014-05-19	01:01:44.955	3.920e-006	-2.150
GRB140521A	320.1770	67.5870	0.0111	11.550	2014-05-21	17:34:18.731	2.990e-006	-2.150
GRB140521B	308.7300	38.8600	10.1000	46.590	2014-05-21	04:25:12.143	2.750e-006	-2.150
GRB140523A	133.3000	24.9500	0.4000	22.000	2014-05-23	03:05:57.811	5.130e-005	-2.150
GRB140603A	217.4500	25.9100	2.1300	138.240	2014-06-03	11:24:59.139	1.860e-005	-2.150
GRB140606B	327.1090	33.0470	2.1927	8.000	2014-06-06	03:11:50.769	6.600e-006	0.384
GRB140607A	86.3730	18.9040	0.0193	109.900	2014-06-07	17:13:31.000	2.200e-006	-2.150
GRB140608B	211.9600	53.8200	2.9100	6.400	2014-06-08	17:07:10.509	1.950e-006	-2.150
GRB140610C	121.7200	6.3200	1.0000	36.860	2014-06-10	13:09:06.401	1.840e-005	-2.150
GRB140614B	322.6310	14.9300	0.0003	49.800	2014-06-14	06:38:11.000	5.500e-007	-2.150
GRB140621A	25.0830	22.4240	0.7200	6.300	2014-06-21	19:50:07.000	1.130e-005	-2.150
GRB140628C	359.1500	31.5600	9.0400	75.520	2014-06-28	16:53:18.980	1.820e-006	-2.150
GRB140629A	248.9770	41.8770	0.0003	42.000	2014-06-29	14:17:30.000	3.400e-006	2.275
GRB140630A	27.5800	47.7300	2.2400	63.740	2014-06-30	12:07:52.823	7.630e-006	-2.150
GRB140703A	12.9960	45.1020	0.0003	84.220	2014-07-03	00:37:07.190	7.400e-007	3.140
GRB140705B	163.8600	56.9700	5.8300	26.880	2014-07-05	12:55:28.740	3.180e-006	-2.150
GRB140709A	304.6660	51.2220	0.0101	98.600	2014-07-09	01:13:41.000	8.800e-006	-2.150

Table A.1: List of the 468 long GRBs used in the presented analysis. A redshift of -2.150 indicates that the redshift of that GRB was not measured.

Name	RA(deg)	Decl(deg)	Err(deg)	T90(s)	Date	UT(Trigger)	F(Erg/cm^2)	Z
GRB140709B	146.0540	63.5290	0.0004	155.000	2014-07-09	15:15:45.000	1.600e-005	-2.150
GRB140710A	41.0680	35.4990	0.0003	3.520	2014-07-10	10:16:40.000	2.300e-007	0.558
GRB140713A	281.1050	59.6340	0.0003	5.380	2014-07-13	18:43:45.303	5.200e-007	-2.150
GRB140714A	220.9900	40.3100	1.1400	132.100	2014-07-14	06:25:55.424	1.570e-005	-2.150
GRB140715A	65.0500	24.0700	1.5600	77.310	2014-07-15	05:33:18.161	9.650e-006	-2.150
GRB140716B	215.2300	57.0100	5.6700	3.330	2014-07-16	07:20:12.701	2.400e-007	-2.150
GRB140720B	141.3500	10.7600	11.6200	9.980	2014-07-20	06:43:43.125	1.880e-006	-2.150
GRB140723B	24.6300	11.1900	2.2300	45.060	2014-07-23	11:58:04.254	2.350e-005	-2.150
GRB140725A	13.3400	66.4500	5.2800	19.970	2014-07-25	14:00:06.867	1.510e-006	-2.150
GRB140727A	68.5300	57.6600	11.3700	13.820	2014-07-27	17:56:44.855	1.320e-006	-2.150
GRB140729A	193.9500	15.3500	0.3400	16.000	2014-07-29	00:36:53.751	2.000e-005	-2.150
GRB140801A	44.0690	30.9380	0.0004	7.170	2014-08-01	18:59:53.257	1.220e-005	1.320
GRB140808A	221.2220	49.2150	0.0006	338.000	2014-08-08	00:53:59.264	3.200e-006	3.290
GRB140809A	170.1100	72.3600	4.1100	69.120	2014-08-09	03:11:10.196	2.100e-006	-2.150
GRB140810A	119.0400	27.5500	0.1200	100.000	2014-08-10	18:46:11.433	1.500e-004	-2.150
GRB140817A	127.2640	58.1900	0.0003	244.000	2014-08-17	07:02:01.000	3.400e-006	-2.150
GRB140818A	199.5540	6.8880	0.0608	109.250	2014-08-18	05:30:09.122	3.680e-005	-2.150
GRB140819A	287.4900	24.1000	12.0200	6.650	2014-08-19	03:50:26.135	3.360e-007	-2.150
GRB140821A	174.7200	13.5300	1.0000	32.510	2014-08-21	23:56:02.841	6.310e-005	-2.150
GRB140824A	206.6170	33.2940	0.0003	3.090	2014-08-24	08:40:28.000	1.900e-007	-2.150
GRB140824B	18.3300	58.6400	1.4900	108.800	2014-08-24	14:33:12.039	1.500e-005	-2.150
GRB140824C	55.6300	4.3500	2.0600	4.090	2014-08-24	13:08:46.174	2.690e-006	-2.150
GRB140825B	342.8400	31.0900	2.6600	78.590	2014-08-25	07:52:45.567	7.810e-006	-2.150
GRB140827A	130.6500	35.8000	1.8200	20.990	2014-08-27	18:18:03.338	1.220e-005	-2.150
GRB140828A	142.0290	14.5690	0.0132	23.560	2014-08-28	06:54:12.179	3.500e-006	-2.150
GRB140829A	255.5900	55.9300	3.5300	77.560	2014-08-29	21:07:27.466	5.120e-006	-2.150
GRB140831B	4.2900	44.0100	9.9000	3.590	2014-08-31	08:59:07.217	1.090e-006	-2.150
GRB140906A	248.3600	49.5100	7.6600	37.630	2014-09-06	04:11:38.696	1.900e-006	-2.150
GRB140906B	185.8400	0.9800	1.6000	20.740	2014-09-06	10:18:02.364	9.910e-006	-2.150
GRB140907A	48.1460	46.6050	0.0002	79.200	2014-09-07	16:07:08.000	5.500e-006	1.210
GRB140917A	171.3700	20.4100	6.1800	16.520	2014-09-17	12:17:06.416	6.220e-006	-2.150
GRB140928B	163.7700	48.4700	7.0700	7.680	2014-09-28	02:23:23.977	2.780e-006	-2.150
GRB140930A	41.6100	57.5800	10.5300	3.260	2014-09-30	03:12:32.489	2.490e-007	-2.150
GRB141004A	76.7340	12.8190	0.0003	3.920	2014-10-04	23:20:54.000	2.200e-006	0.573
GRB141005A	291.0930	36.0950	0.0003	3.390	2014-10-05	05:13:06.968	2.600e-006	-2.150
GRB141015A	87.5190	18.3290	0.0004	11.000	2014-10-15	09:12:59.000	1.600e-007	-2.150
GRB141020A	224.9960	55.3130	0.0003	15.550	2014-10-20	07:48:39.000	4.600e-007	-2.150
GRB141026A	44.0840	26.9280	0.0003	146.000	2014-10-26	02:36:51.000	1.300e-006	-2.150
GRB141026B	132.8200	62.4800	13.3000	2.560	2014-10-26	17:48:07.097	3.970e-007	-2.150
GRB141029B	102.5000	25.0700	1.0000	202.440	2014-10-29	03:13:18.617	3.800e-005	-2.150
GRB141030A	161.3700	33.4000	6.6500	21.090	2014-10-30	17:54:13.884	-2.400e-006	-2.150
GRB141031B	356.9050	41.3530	0.0003	16.000	2014-10-31	14:56:45.000	2.500e-007	-2.150
GRB141031C	26.7200	45.9800	9.0100	38.660	2014-10-31	06:10:40.949	1.600e-006	-2.150
GRB141102C	114.2200	22.7300	12.7900	25.080	2014-11-02	18:41:18.957	8.440e-007	-2.150

Table A.1: List of the 468 long GRBs used in the presented analysis. A redshift of -2.150 indicates that the redshift of that GRB was not measured.

Name	RA(deg)	Decl(deg)	Err(deg)	T90(s)	Date	UT(Trigger)	F(Erg/cm^2)	Z
GRB141109B	222.3030	73.1310	0.0003	54.200	2014-11-09	07:47:39.000	6.300e-007	-2.150
GRB141109C	204.2900	79.0300	2.7700	32.000	2014-11-09	10:43:57.808	5.210e-006	-2.150
GRB141118A	156.8740	19.0700	11.7580	8.448	2014-11-18	16:15:48.540	2.300e-006	-2.150
GRB141130A	222.8220	47.3190	0.0003	62.900	2014-11-30	23:10:56.000	8.790e-006	-2.150
GRB141206A	320.5600	2.4200	9.2900	4.610	2014-12-06	06:05:51.710	5.370e-007	-2.150
GRB141207A	159.9900	3.9100	0.2150	20.000	2014-12-07	19:11:22.452	4.870e-005	-2.150
GRB141208A	239.1600	10.9700	9.4900	14.330	2014-12-08	00:55:02.978	1.770e-006	-2.150
GRB141212B	250.8760	31.7500	0.0004	10.500	2014-12-12	13:23:48.000	1.650e-006	-2.150
GRB141220A	195.0580	32.1460	0.0122	8.448	2014-12-20	06:02:51.666	4.700e-006	1.319
GRB141221A	198.2870	8.2050	0.0003	36.900	2014-12-21	08:07:10.000	3.400e-006	-2.150
GRB141222B	97.4300	40.1300	1.0000	34.050	2014-12-22	16:34:30.340	2.330e-005	-2.150
GRB141225A	138.7780	33.7920	0.0003	56.320	2014-12-25	23:01:13.817	6.500e-006	0.915
GRB141226A	163.8500	28.3900	6.2600	38.650	2014-12-26	21:07:24.518	3.210e-006	-2.150
GRB141229B	170.1000	23.0600	4.3000	22.020	2014-12-29	21:52:10.852	2.150e-006	-2.150
GRB141230A	56.9800	1.5900	3.8600	9.860	2014-12-30	03:24:22.637	1.200e-006	-2.150
GRB141230B	181.4700	11.6500	4.2300	28.930	2014-12-30	20:00:25.666	3.160e-006	-2.150
GRB150106A	40.8300	0.3100	13.1400	79.880	2015-01-06	22:05:56.248	1.020e-006	-2.150
GRB150110A	217.0000	18.9000	1.0000	74.300	2015-01-10	10:23:38.232	2.810e-006	-2.150
GRB150110B	289.3750	32.5230	0.0003	10.600	2015-01-10	22:08:30.000	5.300e-007	-2.150
GRB150120B	39.2910	8.0780	0.0002	24.300	2015-01-20	07:21:55.000	5.400e-007	-2.150
GRB150120C	48.1100	26.9400	9.9400	56.830	2015-01-20	16:26:17.465	1.950e-006	-2.150
GRB150127C	300.6800	32.6600	9.6600	84.220	2015-01-27	22:26:38.543	1.770e-006	-2.150
GRB150128B	272.2700	27.7800	3.3200	85.250	2015-01-28	18:59:14.294	1.170e-005	-2.150
GRB150131A	16.1200	11.3600	5.8100	8.190	2015-01-31	08:03:02.497	1.450e-006	-2.150
GRB150131B	62.2700	19.2700	5.3100	8.200	2015-01-31	22:49:26.183	2.490e-006	-2.150
GRB150202B	86.7700	58.5500	1.0000	167.420	2015-02-02	23:59:08.273	3.150e-005	-2.150
GRB150203A	98.3990	6.9540	0.0004	25.800	2015-02-03	04:09:07.000	1.290e-006	-2.150
GRB150206B	220.5900	57.5000	6.7600	5.120	2015-02-06	09:46:27.485	1.100e-006	-2.150
GRB150210A	112.1500	13.2700	0.3300	31.300	2015-02-10	22:26:24.283	7.800e-005	-2.150
GRB150211A	254.8460	55.3900	0.0101	13.600	2015-02-11	11:52:11.000	2.400e-005	-2.150
GRB150211B	336.5600	38.9800	9.0800	18.430	2015-02-11	05:44:16.828	8.700e-007	-2.150
GRB150212A	285.4970	47.3890	0.0122	11.400	2015-02-12	10:57:19.000	8.900e-007	-2.150
GRB150213B	253.4520	34.1890	0.0003	181.000	2015-02-13	22:31:30.000	3.000e-006	-2.150
GRB150226B	51.1000	28.4800	2.5800	174.600	2015-02-26	13:05:23.154	8.630e-006	-2.150
GRB150226C	157.7600	18.3700	11.3000	32.760	2015-02-26	22:45:49.001	8.420e-007	-2.150
GRB150302A	175.5310	36.8110	0.0006	23.740	2015-03-02	05:42:36.000	2.600e-007	-2.150
GRB150309A	277.1020	86.4290	0.0003	242.000	2015-03-09	23:03:06.000	3.900e-005	-2.150
GRB150314A	126.6700	63.8340	0.0003	10.690	2015-03-14	04:54:50.854	8.530e-005	1.758
GRB150317A	138.9850	55.4660	0.0004	23.290	2015-03-17	04:22:42.000	6.500e-007	-2.150
GRB150323A	128.1780	45.4650	0.0003	149.600	2015-03-23	02:49:14.000	1.100e-005	0.593
GRB150323B	260.4470	38.3160	0.0250	56.320	2015-03-23	09:28:39.209	2.190e-005	-2.150
GRB150323C	192.6170	50.1910	0.0003	43.270	2015-03-23	17:05:09.638	2.500e-006	-2.150
GRB150326A	345.3900	8.1900	12.1100	5.890	2015-03-26	12:30:42.320	4.690e-007	-2.150
GRB150330A	331.0280	52.2970	1.0617	194.560	2015-03-30	19:52:18.572	1.280e-004	-2.150

Table A.1: List of the 468 long GRBs used in the presented analysis. A redshift of -2.150 indicates that the redshift of that GRB was not measured.

Name	RA(deg)	Decl(deg)	Err(deg)	T90(s)	Date	UT(Trigger)	F(Erg/cm^2)	Z
GRB150411A	342.7500	28.3900	12.0100	15.360	2015-04-11	00:37:49.347	7.030e-007	-2.150
GRB150413A	190.3960	71.8390	0.0193	263.600	2015-04-13	13:54:58.000	1.420e-005	3.139
GRB150416A	58.7500	52.9600	1.9300	33.280	2015-04-16	18:33:25.965	6.240e-006	-2.150
GRB150426B	283.5200	0.6500	3.2500	61.700	2015-04-26	22:59:10.683	6.180e-006	-2.150
GRB150428A	188.5390	6.9540	0.0003	53.200	2015-04-28	01:30:40.000	1.610e-005	-2.150
GRB150428B	292.6390	4.1250	0.0003	130.900	2015-04-28	03:12:03.000	3.700e-006	-2.150
GRB150428D	242.3300	69.5100	6.0600	32.510	2015-04-28	07:19:02.950	1.530e-006	-2.150
GRB150502A	241.4600	42.0600	1.0000	109.310	2015-05-02	10:25:55.163	2.550e-005	-2.150
GRB150506A	176.2500	7.5600	1.4600	6.780	2015-05-06	09:33:47.785	3.560e-006	-2.150
GRB150510A	15.1380	4.9850	0.3600	62.000	2015-05-10	03:19:48.505	1.900e-004	-2.150
GRB150512A	200.5000	59.1100	3.6400	123.140	2015-05-12	10:22:25.873	2.170e-005	-2.150

APPENDIX
B

Variables used in the BDT

In this appendix, the distributions of the variables used in the BDT are presented. The explanation of these variables as well as their importance in the BDT are given in Table 4.4.

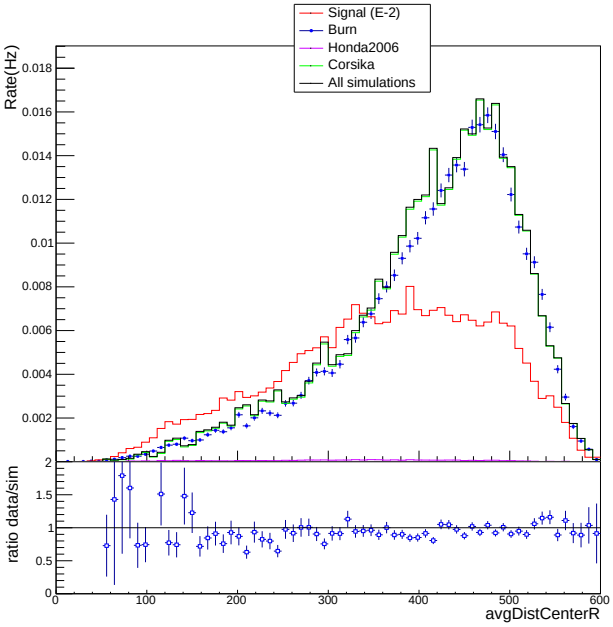

Figure B.1: avgDistCenterR

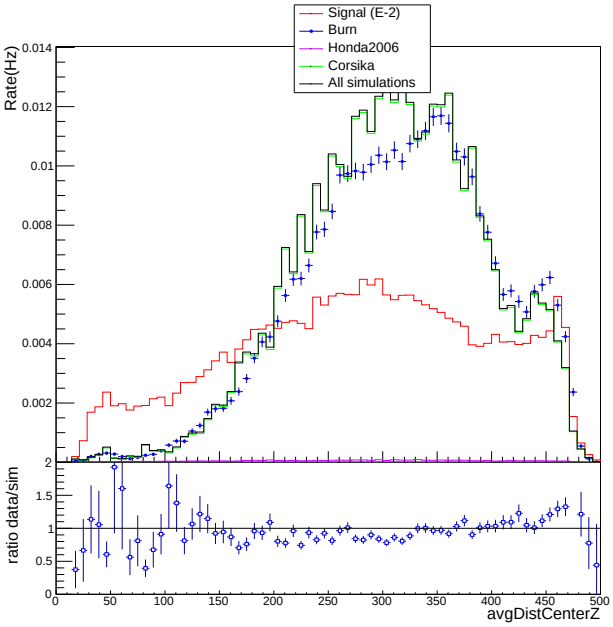

Figure B.2: avgDistCenterZ

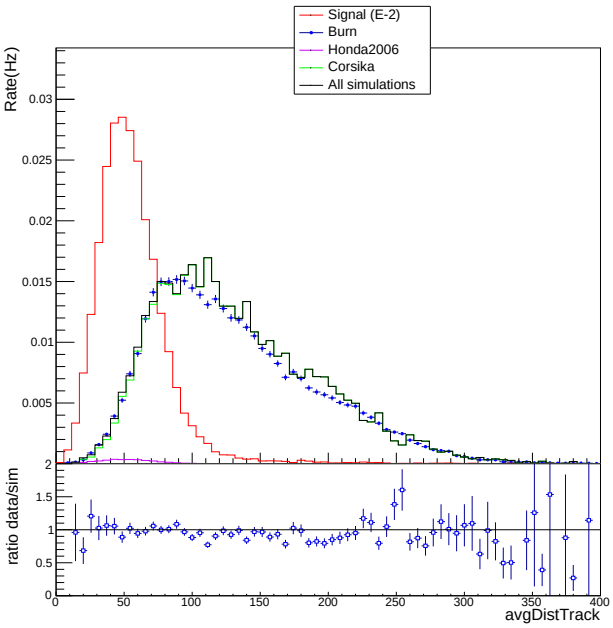

Figure B.3: `avgDistTrack`

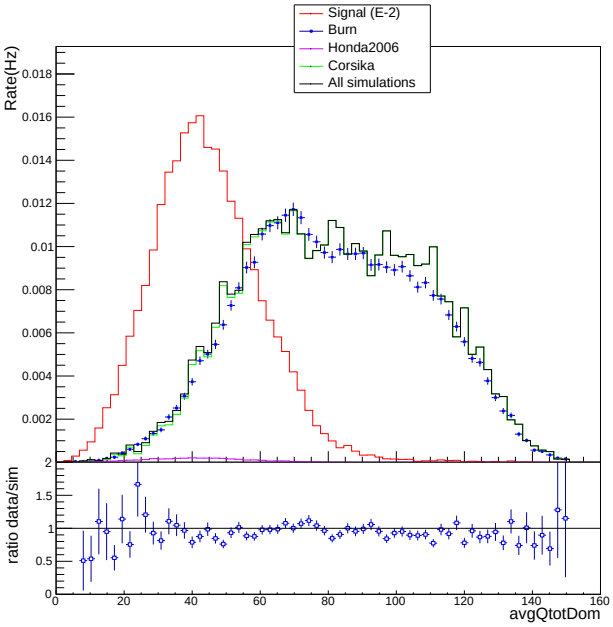

Figure B.4: `avgQtotDom`

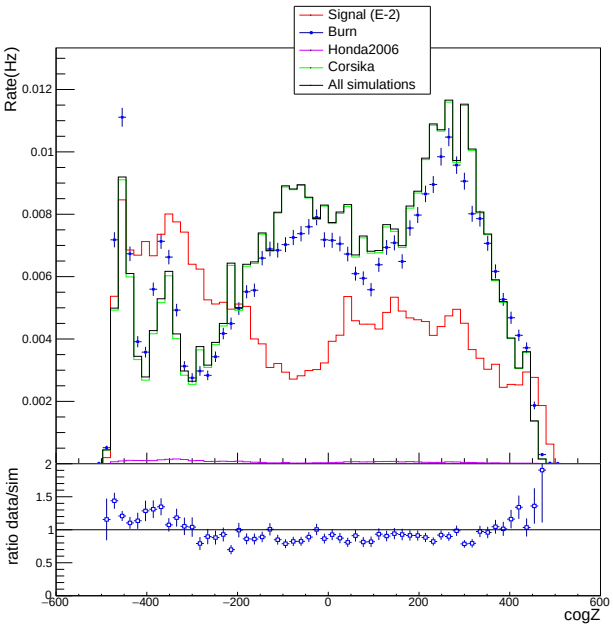

Figure B.5: cogZ

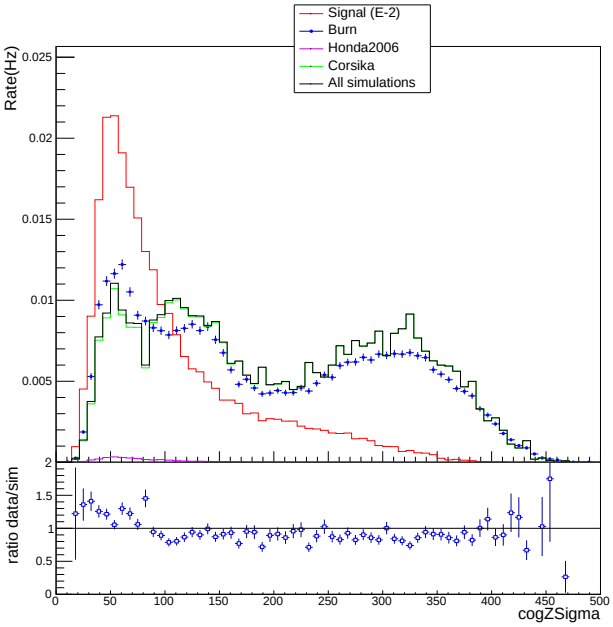

Figure B.6: cogZSigma

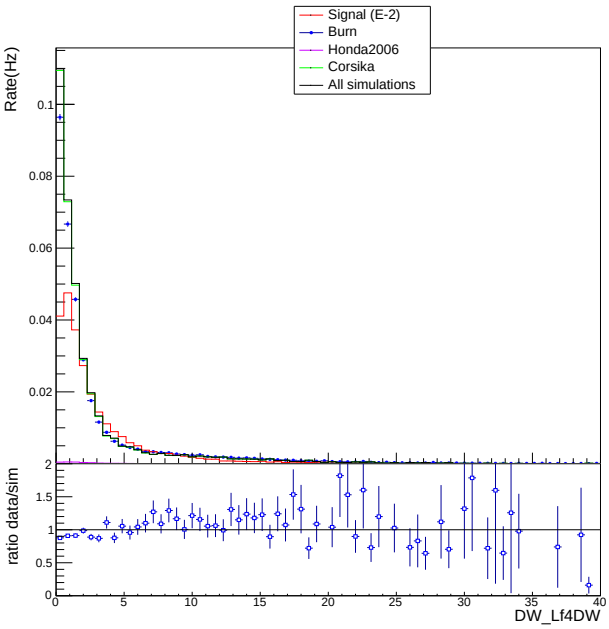

Figure B.7: `DW_Lf4DW`

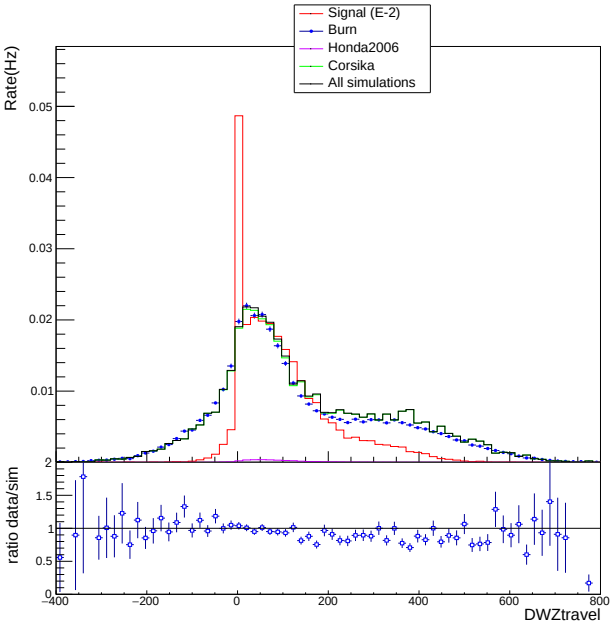

Figure B.8: `DWZtravel`

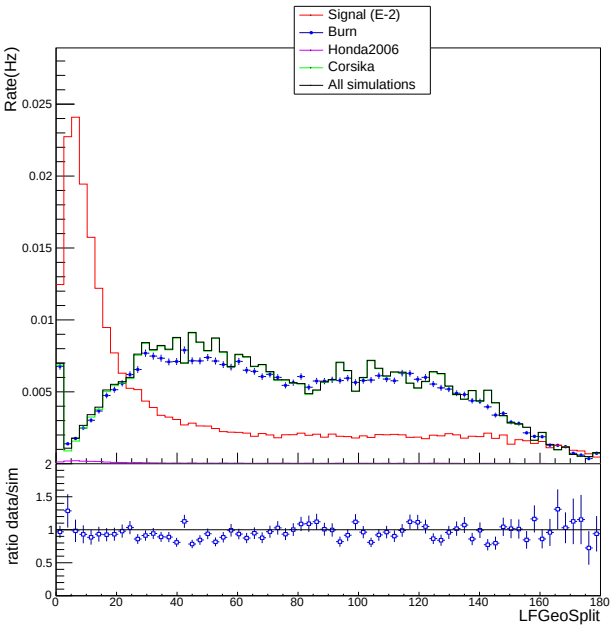

Figure B.9: `LineFit_GeoSplit`

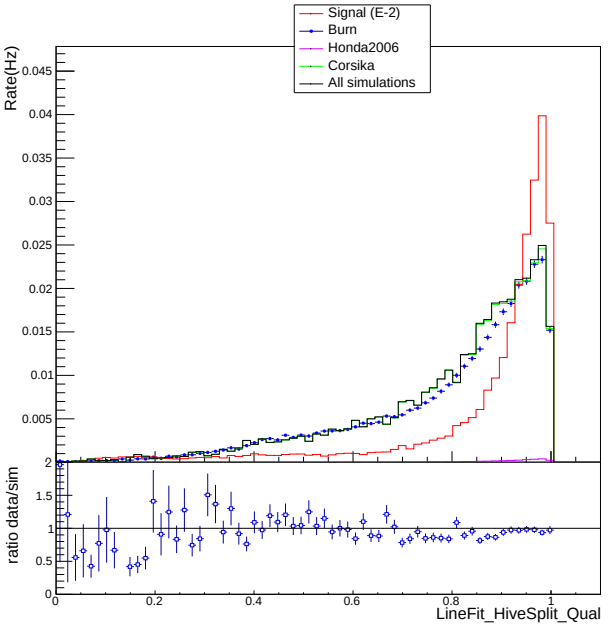

Figure B.10: `LineFit_HiveSplit_Qual`

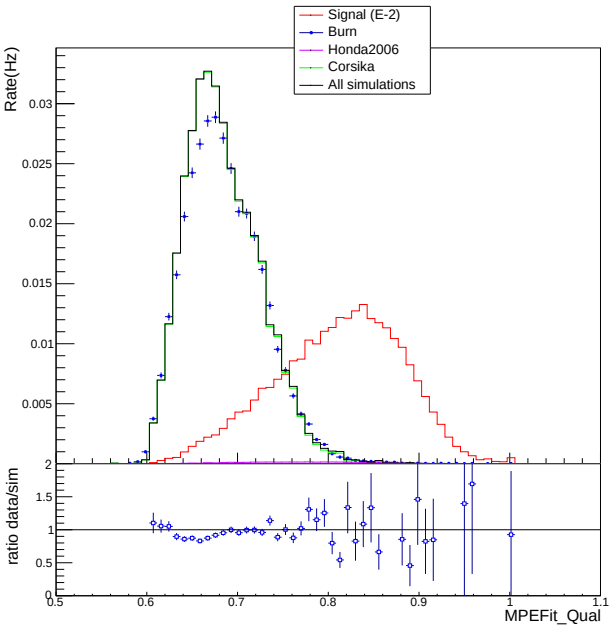

Figure B.11: `MPEFit_Qual`

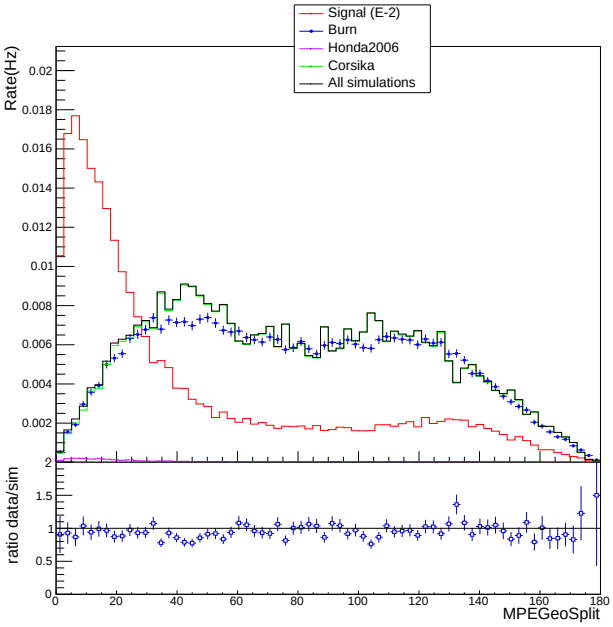

Figure B.12: `MPEFit_GeoSplit`

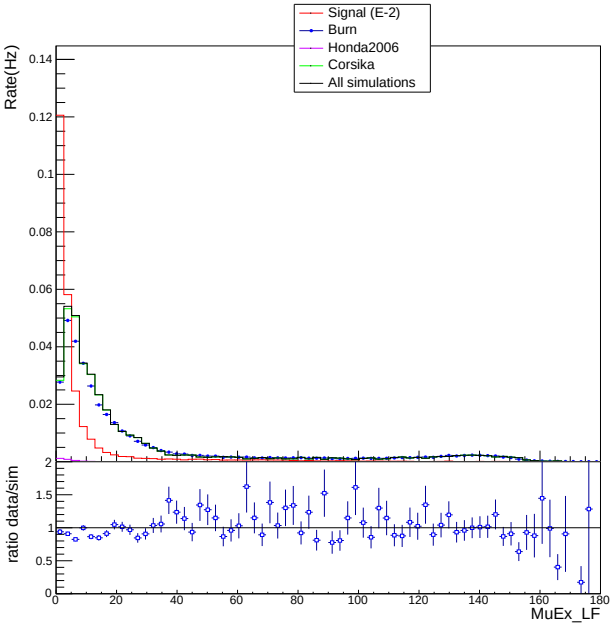

Figure B.13: `MuEx_LF`

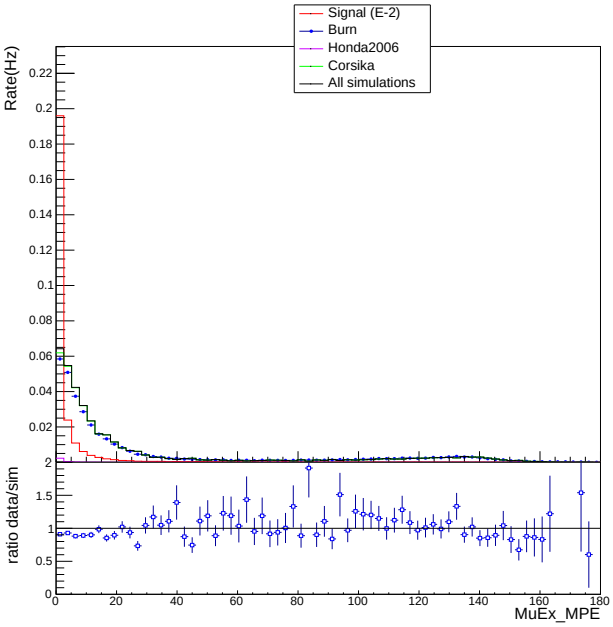

Figure B.14: `MuEx_MPE`

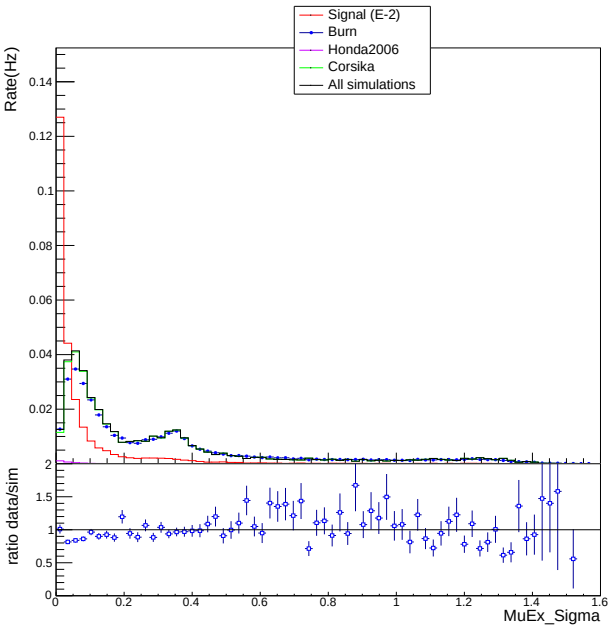

Figure B.15: `MuEx_Sigma`

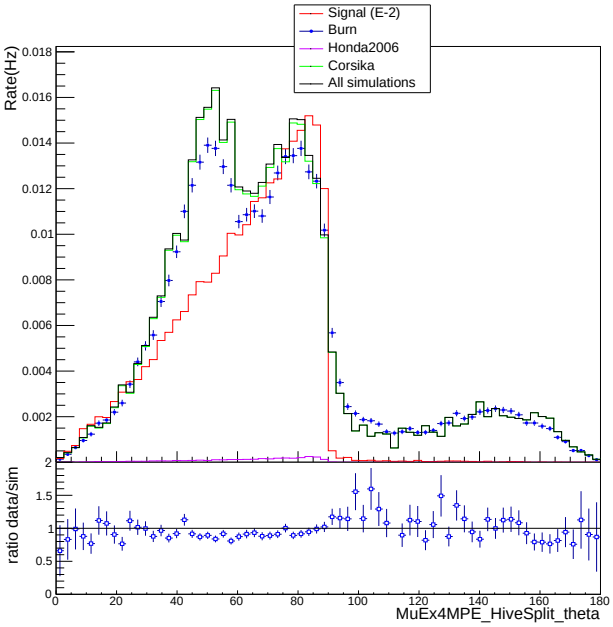

Figure B.16: `MuEx4MPE_HiveSplit_zen`

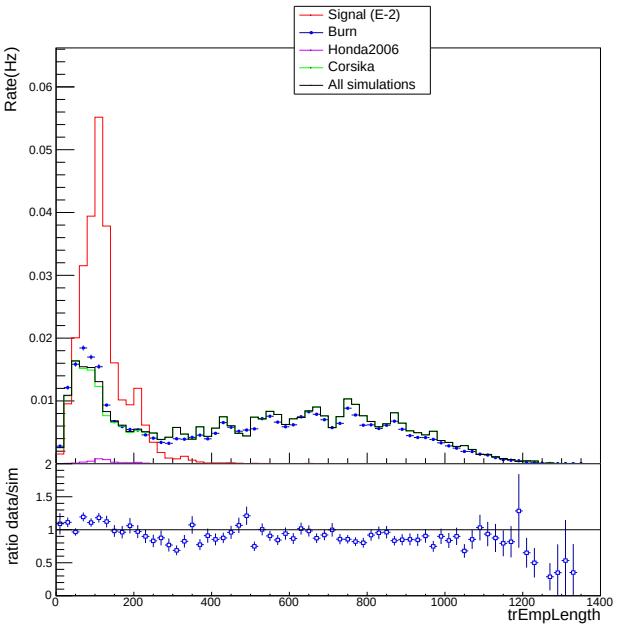

Figure B.17: `trEmpLength`

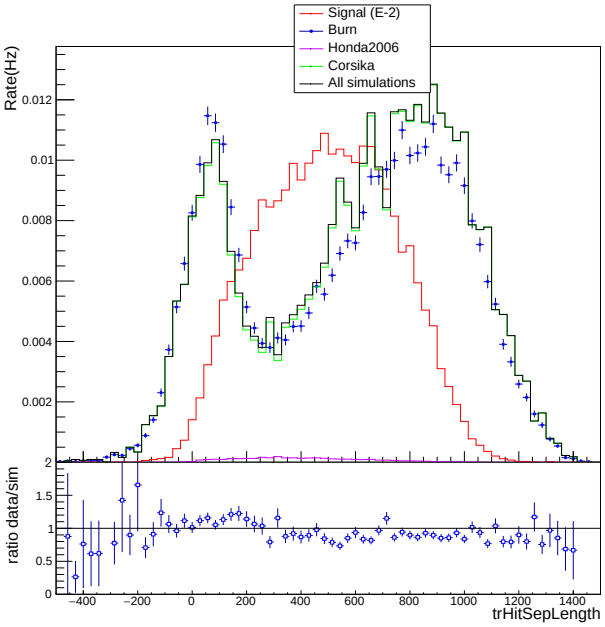

Figure B.18: `trHitSepLength`

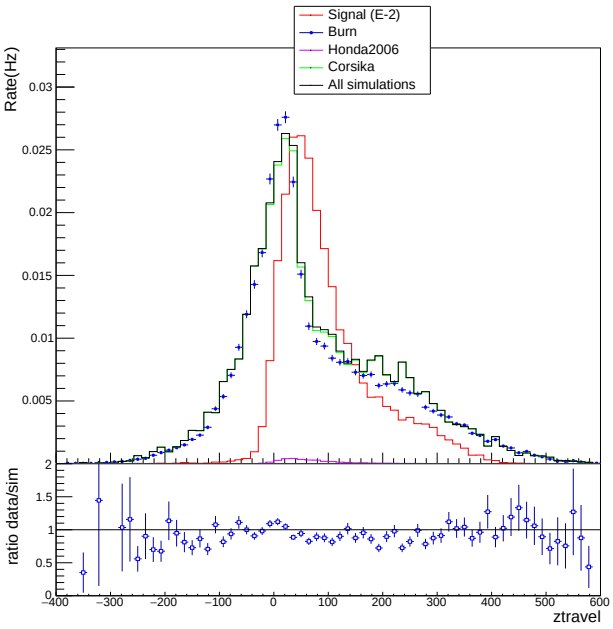

Figure B.19: ZTravel

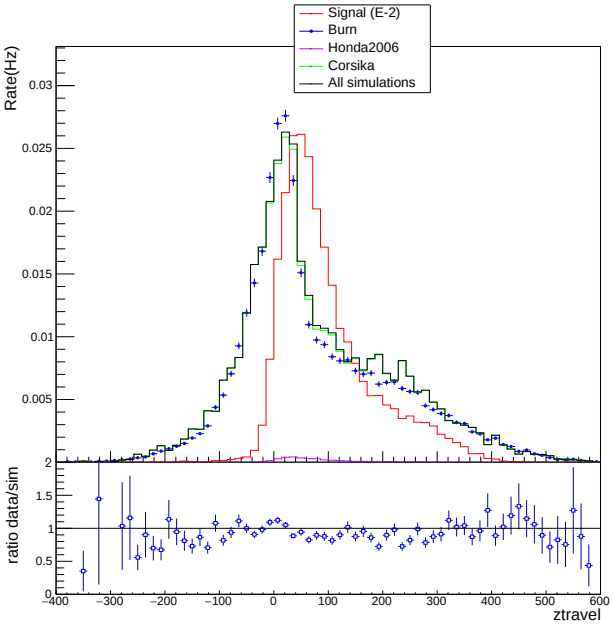

Figure B.20: ZTravel

List of Figures

List of Tables

Bibliography

[1] M. Walter and A.W. Wolfendale. Early history of cosmic particle physics. *The European Physical Journal H*, 37(3):323–358, 2012.

[2] T. Wulf. Beobachtungen über die Strahlung hoher Durchdringungsfähigkeit auf dem Eiffelturm. *Phys. Zeit.*, 11:811–813, 1910.

[3] V. Hess. Observations in low level radiation during seven free balloon flights. *Phys. Zeit*, 13:1084–1091, 1912.

[4] K.D. de Vries. *Macroscopic modelling of radio emission from ultra-high-energy-cosmic-ray-induced air showers*. PhD thesis, Rijksuniversiteit Groningen, 2013.

[5] J. Blümer, R. Engel, and J. R. Hörandel. Cosmic rays from the knee to the highest energies. *Progress in Particle and Nuclear Physics*, 63(2):293 – 338, 2009.

[6] F. L. Wilson. Fermi's Theory of Beta Decay. *American Journal of Physics*, 36(12), 1968.

[7] C. L. Cowan, F. Reines, F. B. Harrison, H. W. Kruse, and A. D. McGuire. Detection of the Free Neutrino: a Confirmation. *Science*, 124(3212):103–104, 1956, http://www.sciencemag.org/content/124/3212/103.full.pdf.

[8] G. Danby et al. Observation of High-Energy Neutrino Reactions and the Existence of Two Kinds of Neutrinos. *Phys. Rev. Lett.*, 9:36–44, Jul 1962.

[9] M. L. Perl et al. Evidence for Anomalous Lepton Production in $e^+ - e^-$ Annihilation. *Phys. Rev. Lett.*, 35:1489–1492, Dec 1975.

[10] K. Kodama et al. Observation of tau neutrino interactions. *Physics Letters B*, 504(3):218 – 224, 2001.

[11] Q. R. Ahmad et al. Measurement of the Rate of $\nu_e + d \rightarrow p + p + e^-$ Interactions Produced by ^8B Solar Neutrinos at the Sudbury Neutrino Observatory. *Phys. Rev. Lett.*, 87:071301, Jul 2001.

[12] Y. Fukuda et al. Evidence for Oscillation of Atmospheric Neutrinos. *Phys. Rev. Lett.*, 81:1562–1567, Aug 1998.

[13] F. Halzen and D. Hooper. High-energy neutrino astronomy: The Cosmic ray connection. *Rept.Prog.Phys.*, 65:1025–1078, 2002, astro-ph/0204527.

[14] T. Piran. The physics of gamma-ray bursts. *Rev. Mod. Phys.*, 76:1143–1210, Jan 2005.

[15] D. A. Kniffen. Gamma-Ray observatory overview. In W. Neil Johnson, editor, *Proceedings of the Gamma Ray Observatory science workshop*, pages 1–10, 1989.

[16] G. J. Fishman. BATSE: The burst and transient source experiment on the gamma ray observatory. In W. Neil Johnson, editor, *Proceedings of the Gamma Ray Observatory science workshop*, pages 39–50, 1989.

[17] C. A. Meegan et al. Spatial distribution of gamma-ray bursts observed by BATSE. *Nature*, 355(6356):143–145, 1992.

[18] M. S. Briggs et al. The Error Distribution of BATSE Gamma-Ray Burst Locations. *The Astrophysical Journal Supplement Series*, 122(2):503, 1999.

[19] E. Costa et al. Discovery of an X-ray afterglow associated with the Gamma-ray burst of 28 February 1997. *Nature*, 387(6635):783–785, 1997.

[20] R.L. Aptekar et al. Konus-W gamma-ray burst experiment for the GGS wind spacecraft. *Space Science Reviews*, 71(1-4):265–272, 1995.

[21] G. Ricker et al. GRB 010921: Localization and Observations by the High Energy Transient Explorer Satellite. *The Astrophysical Journal Letters*, 571(2):L127, 2002.

[22] C. Winkler et al. The INTEGRAL mission. *A&A*, 411(1):L1–L6, 2003.

[23] N. Gehrels et al. The Swift Gamma-Ray Burst Mission. *The Astrophysical Journal*, 611(2):1005, 2004.

[24] A. Bouvier. Gamma-Ray Burst Observations at High Energy with the Fermi Large Area Telescope. *ArXiv e-prints*, Nov 2010, 1012.0558.

[25] D. Band et al. BATSE observations of gamma-ray burst spectra. 1. Spectral diversity. *Astrophys.J.*, 413:281–292, 1993.

[26] E. Ramirez-Ruiz and E. E. Fenimore. Pulse Width Evolution in Gamma-Ray Bursts: Evidence for Internal Shocks. *The Astrophysical Journal*, 539(2):712, 2000.

[27] J.P. Norris, G.F. Marani, and J.T. Bonnell. Connection between Energy-dependent Lags and Peak Luminosity in Gamma-Ray Bursts. *Astrophys.J.*, 534:248–257, 2000, astro-ph/9903233.

[28] E. E. Fenimore and E. Ramirez-Ruiz. Redshifts for 220 BATSE gamma-ray bursts determined by variability and the cosmological consequences. *Astrophys.J.*, 2000, astro-ph/0004176.

[29] C. Kouveliotou et al. Identification of two classes of gamma-ray bursts. *Astrophys.J.*, 413:L101–104, 1993.

[30] Y. Qin et al. A Comprehensive Analysis of Fermi Gamma-Ray Burst Data. III. Energy-dependent T_{90} Distributions of GBM GRBs and Instrumental Selection Effect on Duration Classification. *The Astrophysical Journal*, 763(1):15, 2013.

[31] G. Ghirlanda, G. Ghisellini, and A. Celotti. The spectra of short gamma-ray bursts. *A&A*, 422(3):L55–L58, 2004.

[32] J. Hjorth et al. The optical afterglow of the short γ-ray burst GRB 050709. *Nature*, 437(7060):859–861, 2005.

[33] A. Volnova et al. A case study of dark GRB 051008. *European Astronomical Society Publications Series*, 61:275–278, 2013.

[34] A. V. Filippenko. Optical spectra of supernovae. *Ann.Rev.Astron.Astrophys.*, 35:309–355, 1997.

[35] D. A. Frail, S. R. Kulkarni, L. Nicastro, M. Feroci, and G. B. Taylor. The radio afterglow from the γ-ray burst of 8 May 1997. *Nature*, 389(6648):261–263, 09 1997.

[36] E. Fermi. On the Origin of the Cosmic Radiation. *Phys. Rev.*, 75:1169–1174, Apr 1949.

[37] F. C. Jones and D. C. Ellison. The plasma physics of shock acceleration. *Space Science Reviews*, 58(1):259–346, 1991.

[38] R. J. Protheroe and R.W. Clay. Ultrahigh energy cosmic rays. *Publ.Astron.Soc.Pac.*, 21:1–22, 2004, astro-ph/0311466.

[39] L O'C Drury. An introduction to the theory of diffusive shock acceleration of energetic particles in tenuous plasmas. *Reports on Progress in Physics*, 46(8):973, 1983.

[40] J.G. Learned and K. Mannheim. High-energy neutrino astrophysics. *Ann.Rev.Nucl.Part.Sci.*, 50:679–749, 2000.

[41] P. Mészáros and M.J. Rees. Gamma-Ray Bursts. *ArXiv e-prints*, 2014, 1401.3012.

[42] E. E. Fenimore, C. D. Madras, and S. Nayakshin. Expanding Relativistic Shells and Gamma-Ray Burst Temporal Structure. *The Astrophysical Journal*, 473(2):998, 1996.

[43] T. Laskar et al. A Reverse Shock in GRB 130427A. *The Astrophysical Journal*, 776(2):119, 2013.

[44] P. Mészáros and M. J. Rees. GRB 990123: reverse and internal shock flashes and late afterglow behaviour. *Monthly Notices of the Royal Astronomical Society*, 306(3):L39–L43, 1999, http://mnras.oxfordjournals.org/content/306/3/L39.full.pdf+html.

[45] P. Mészáros and M. J. Rees. Optical and Long-Wavelength Afterglow from Gamma-Ray Bursts. *The Astrophysical Journal*, 476(1):232, 1997.

[46] B. Paczynski and G.H. Xu. Neutrino bursts from gamma-ray bursts. *Astrophys.J.*, 427:708–713, 1994.

[47] J. K. Becker. High-energy neutrinos in the context of multimessenger physics. *Phys.Rept.*, 458:173–246, 2008, 0710.1557.

[48] E. Waxman and J. N. Bahcall. High-energy neutrinos from cosmological gamma-ray burst fireballs. *Phys.Rev.Lett.*, 78:2292–2295, 1997, astro-ph/9701231.

[49] M. G. Aartsen et al. Search for Galactic PeV gamma rays with the IceCube Neutrino Observatory. *Phys. Rev. D*, 87:062002, Mar 2013.

[50] R. Abbasi et al. An absence of neutrinos associated with cosmic-ray acceleration in γ-ray bursts. *Nature*, 484:351–353, 2012, 1204.4219.

[51] P. Baerwald, M. Bustamante, and W. Winter. Are gamma-ray bursts the sources of ultra-high energy cosmic rays? *ArXiv e-prints*, 2014, 1401.1820.

[52] M. Ahlers, M.C. Gonzalez-Garcia, and F. Halzen. {GRBs} on probation: Testing the {UHE} {CR} paradigm with icecube. *Astroparticle Physics*, 35(2):87 – 94, 2011.

[53] K. Mannheim, R. J. Protheroe, and J. P. Rachen. Cosmic ray bound for models of extragalactic neutrino production. *Phys. Rev. D*, 63:023003, Dec 2000.

[54] D. Guetta, D. Hooper, J. Alvarez-Muñiz, F. Halzen, and E. Reuveni. Neutrinos from individual gamma-ray bursts in the BATSE catalog. *Astroparticle Physics*, 20(4):429 – 455, 2004.

[55] A. Mücke, J.P. Rachen, R. Engel, R.J. Protheroe, and T. Stanev. Photomeson production in astrophysical sources. *arXiv preprint astro-ph/9905153*, 1999.

[56] I. Vurm and J. Poutanen. Time-Dependent Modeling of Radiative Processes in Hot Magnetized Plasmas. *The Astrophysical Journal*, 698(1):293, 2009.

[57] F. Halzen and S. R. Klein. Invited Review Article: IceCube: An instrument for neutrino astronomy. *Review of Scientific Instruments*, 81(8):–, 2010.

[58] E. Andres et al. Observation of high-energy neutrinos using cerenkov detectors embedded deep in antarctic ice. *Nature*, 410(6827):441–443, 03 2001.

[59] R. Abbasi et al. IceCube - Astrophysics and Astroparticle Physics at the South Pole. *ArXiv e-prints*, 2011, 1111.5188.

[60] T. Gaisser and F. Halzen. Icecube. *Annual Review of Nuclear and Particle Science*, 64(1):101–123, 2014, http://dx.doi.org/10.1146/annurev-nucl-102313-025321.

[61] R. Abbasi et al. The IceCube data acquisition system: Signal capture, digitization, and timestamping. *Nuclear Instruments and Methods in Physics Research Section A: Accelerators, Spectrometers, Detectors and Associated Equipment*, 601(3):294 – 316, 2009.

[62] J. Ahrens et al. Sensitivity of the IceCube detector to astrophysical sources of high energy muon neutrinos. *Astroparticle Physics*, 20(5):507 – 532, 2004.

[63] R. Gandhi, C. Quigg, M. H. Reno, and I. Sarcevic. Ultrahigh-energy neutrino interactions. *Astroparticle Physics*, 5(2):81 – 110, 1996.

[64] T. K. Gaisser and T. Stanev. Neutrino-induced muon flux deep underground and search for neutrino oscillations. *Phys. Rev. D*, 30:985–990, Sep 1984.

[65] S. Iyer Dutta, M. H. Reno, I. Sarcevic, and D. Seckel. Propagation of muons and taus at high energies. *Phys. Rev. D*, 63:094020, Apr 2001.

[66] P. C. Redl. *A search for muon neutrinos coincident with gamma-ray bursts with the IceCube 59-string detector*. PhD thesis, University of Maryland, 2011.

[67] E. V. Bugaev and Yu. V. Shlepin. Photonuclear interaction of high energy muons and tau leptons. *Phys. Rev. D*, 67:034027, Feb 2003.

[68] J. D. Jackson. *Classical Electrodynamics*. John Wiley & Sons, New Jersey, USA, third edition, 1998.

[69] S. Bechet. *Recherche d'un flux diffus de neutrinos tauiques d'origine cosmique dans le détecteur IceCube*. PhD thesis, Université Libre de Bruxelles, 2012.

[70] J.L. Kelley. *"Event Triggering in the IceCube Data Acquisition System"*. IceCube Collaboration, 2014.

[71] J.L. Kelley. *"DOMs and the DAQ Demystified"*. IceCube Collaboration, 2013. Bootcamp.

[72] M. et al. Ackermann. Optical properties of deep glacial ice at the south pole. *Journal of Geophysical Research: Atmospheres*, 111(D13):n/a–n/a, 2006.

[73] P. B. Price, K. Woschnagg, and D. Chirkin. Age vs depth of glacial ice at south pole. *Geophysical Research Letters*, 27(14):2129–2132, 2000.

[74] M.G. Aartsen et al. Measurement of South Pole ice transparency with the IceCube LED calibration system. *Nuclear Instruments and Methods in Physics Research Section A: Accelerators, Spectrometers, Detectors and Associated Equipment*, 711(0):73 – 89, 2013.

[75] R. C. Bay, R. A. Rohde, P. B. Price, and N. E. Bramall. South Pole paleowind from automated synthesis of ice core records. *Journal of Geophysical Research: Atmospheres*, 115(D14):n/a–n/a, 2010.

[76] M. Zoll. Preparations for the next solar WIMP analysis with IceCube. Technical report, IceCube Collaboration internal report, 2014.

[77] J. Ahrens et al. Muon track reconstruction and data selection techniques in AMANDA. *Nuclear Instruments and Methods in Physics Research Section A: Accelerators, Spectrometers, Detectors and Associated Equipment*, 524(1–3):169 – 194, 2004.

[78] M.G. Aartsen et al. Improvement in fast particle track reconstruction with robust statistics. *Nuclear Instruments and Methods in Physics Research Section A: Accelerators, Spectrometers, Detectors and Associated Equipment*, 736(0):143 – 149, 2014.

[79] D. Chirkin. Photon propagation approximations and energy reconstruction. Technical report, IceCube Collaboration internal report, 2007.

[80] D. Heck, G Schatz, J Knapp, T Thouw, and JN Capdevielle. CORSIKA: A Monte Carlo code to simulate extensive air showers. Technical Report FZKA-6019, Forschungszentrum Karlsruhe, 1998.

[81] A. Gazizov and M. Kowalski. ANIS: High energy neutrino generator for neutrino telescopes. *Computer Physics Communications*, 172(3):203 – 213, 2005.

[82] M. Richman. *A search for muon neutrinos coincident with northern gamma-ray bursts using IceCube*. PhD thesis, University of Maryland, 2015.

[83] A. Hoecker et al. TMVA - Toolkit for Multivariate Data Analysis. *ArXiv Physics e-prints*, Mar 2007, physics/0703039.

[84] M. G. Aartsen et al. Search for Prompt Neutrino Emission from Gamma-Ray Bursts with IceCube. *The Astrophysical Journal Letters*, 805(1):L5, 2015.

[85] S. Razzaque, P. Mészáros, and E. Waxman. Neutrino tomography of gamma ray bursts and massive stellar collapses. *Phys. Rev. D*, 68:083001, Oct 2003.

[86] P. Mészáros, S. Kobayashi, S. Razzaque, and B. Zhang. High energy photons, neutrinos and gravitational waves from gamma-ray bursts. *eConf*, C0208122:30–43, 2002, astro-ph/0305066.

[87] M. Kulldorff. Spatial Scan Statistics: Models, Calculations, and Applications. In Joseph Glaz and N. Balakrishnan, editors, *Scan Statistics and Applications*, Statistics for Industry and Technology, pages 303–322. Birkhäuser Boston, 1999.

[88] N. van Eijndhoven. On the observability of high-energy neutrinos from gamma ray bursts. *Astroparticle Physics*, 28(6):540 – 546, 2008.

[89] D. Bose, L. Brayeur, M. Casier, K.D. de Vries, G. Golup, and N. van Eijndhoven. Bayesian approach for counting experiment statistics applied to a neutrino point source analysis. *Astroparticle Physics*, 50–52:57 – 64, 2013.

[90] R. S. Pilla, C. Loader, and C. C. Taylor. New Technique for Finding Needles in Haystacks: Geometric Approach to Distinguishing between a New Source and Random Fluctuations. *Phys. Rev. Lett.*, 95:230202, Dec 2005.

[91] H. Cramér. Mathematical methods of statistics. *University Press: Princeton*, 1946.

[92] CR. Rao. Minimum variance and the estimation of several parameters. *Proc. Cambridge Phil. Soc.*, 43:280–283, 1946.

[93] R. Abbasi et al. Calibration and characterization of the icecube photomultiplier tube. *Nuclear Instruments and Methods in Physics Research Section A: Accelerators, Spectrometers, Detectors and Associated Equipment*, 618(1–3):139 – 152, 2010.

[94] R. Abbasi et al. Search for muon neutrinos from gamma-ray bursts with the icecube neutrino telescope. *The Astrophysical Journal*, 710(1):346, 2010.

[95] Gary J. Feldman and Robert D. Cousins. Unified approach to the classical statistical analysis of small signals. *Phys. Rev. D*, 57:3873–3889, Apr 1998.

[96] Martin Casier. *Search for High-Energy Neutrino Production in Short Gamma Ray Bursts with the IceCube Neutrino Observatory* . PhD thesis, Vrije Universiteit Brussel, 2015.

[97] M. G. Aartsen et al. IceCube-Gen2: A Vision for the Future of Neutrino Astronomy in Antarctica. 2014, 1412.5106.

Index